RADIATION TRANSPORT IN LOW PRESSURE PLASMAS: LIGHTING AND SEMICONDUCTOR ETCHING PLASMAS

BY

KAPIL RAJARAMAN

B.Tech., Indian Institute of Technology, Bombay, 1999
M.S., University of Illinois at Urbana-Champaign, 2000

DISSERTATION

Submitted in partial fulfillment of the requirements
for the degree of Doctor of Philosophy in Physics
in the Graduate College of the
University of Illinois at Urbana-Champaign, 2005

Urbana, Illinois

RADIATION TRANSPORT IN LOW-PRESSURE PLASMAS: LIGHTING AND SEMICONDUCTOR ETCHING PLASMAS

Kapil Rajaraman, Ph.D.
Department of Physics
University of Illinois at Urbana-Champaign, 2005
Mark J. Kushner, Advisor

Ultra-violet (UV) radiation is emitted by many molecular and atomic species in technological plasmas. In some products like lamps, the transport of radiation is an important design consideration. In other instances, such as semiconductor materials processing, the role of UV photons in surface processes is a side product and is poorly understood. Since the basic surface reaction mechanisms in semiconductor processing are now being developed, it is an opportune time to investigate the role of UV photons.

As lamp geometries become increasingly complex, analytical methods to treat radiation transport become more difficult to implement. Design of lamps must therefore rely on numerical methods. To investigate radiative processes in lighting plasmas, a Monte Carlo Radiation Transport Model was developed and interfaced with a two-dimensional plasma equipment model (HPEM). Investigations were performed on low pressure Ar/Hg electrodeless discharges. We found that analytically computed radiation trapping factors are less accurate when there is a non-uniform density of absorbers and emitters, as may occur in low pressure lamps. In our case these non-uniformities are due primarily to cataphoresis. We found that the shape of the plasma cavity influences trapping factors, primarily due to the consequences of transport of Hg ions on the distribution of radiators.

To address the role of radiation transport in semiconductor etching plasmas, we investigated the plasma etching of SiO_2 in fluorocarbon plasmas, a process dependent on polymer deposition. We first developed a surface reaction mechanism to understand the role played by the polymer film that overlays the SiO_2 substrate, and is essential to facilitating an etch. This mechanism was implemented in a Surface Kinetics Model of the HPEM. We found that the dominant etch channel in C_4F_8 plasmas was due to the fluorine released in the polymer layer by energetic ion bombardment. For plasmas that do not lead to strongly bound films (like C_2F_6 plasmas), defluorination is no longer the dominant SiO_2 etch process.

Finally, we combined the models above to address radiation transport in fluorocarbon/Ar etching plasmas. We found that resonance radiation from Ar produced only small increases in etch rate due to photon-induced defluorination, and this increase was well offset by the decrease in etch rate due to a lower amount of etchant fluorine in the polymer layer. At the process regimes of interest to us, the ion-induced defluorination was much more dominant than UV-induced defluorination.

ACKNOWLEDGMENTS

First and foremost, I would like to express my deepest gratitude to my advisor, Prof. Mark Kushner for all his help and guidance. I am especially thankful to him for being patient with me, and supporting and motivating me through difficult times. I have acquired an immense amount of knowledge from him, both science-related and otherwise. This learning has helped me vastly through my graduate career, and I am sure that it will continue to do so in the future.

I would also like to thank the members of my dissertation committee, Prof. Munir Nayfeh, Prof. Douglas Beck, Prof. J. Gary Eden, and Prof. Robert Clegg, for their comments. I would like to acknowledge the support of the Semiconductor Research Corporation (SRC), Osram Sylvania Inc., and the National Science Foundation (NSF).

I have received a lot of valuable knowledge and feedback from my peers in the Computational Optical and Discharge Physics Group: Pramod Subramonium, Arvind Sankaran, Ramesh Arakoni, Ankur Agarwal, Ananth Bhoj, Vivek Vyas, Rajesh Dorai, Alex Vasenkov, and Shane Stafford. I would like to thank my friends at the University of Illinois for very beneficial conversations: Sanghyun Park, Aki Palanisami, Tommy Angelini, Ziggy Majumdar, Dyutiman Das, Jordan Vincent, Matt Gordon, Hector Garcia and Dom Ricci. I would specially like to thank Joscelyn Fisher for her support.

I would like to thank my parents for nurturing the love of knowledge in me, my elder brother, Arvind, for showing me how well and elegantly that knowledge can be used, and the faculty at the physics department at the Indian Institute of Technology and the University of Illinois for educating me and helping me realize my potential.

TABLE OF CONTENTS

Page

1. TECHNOLOGICAL PLASMAS 1
    1.1 Plasma Physics 1
    1.2 Overview of the Dissertation 2
    1.3 Tables 5
    1.4 Figures 6
    1.5 References 7

2. INTRODUCTION TO RADIATION TRANSPORT 8
    2.1 Discharge Lamps 8
    2.2 Electrodeless Lamps 10
    2.3 Radiation Transport 11
        2.3.1. Broadening Mechanisms 11
        2.3.2. Theory of Radiation Transport 14
    2.4 Numerical Methods for Radiation Transport 17
    2.5 Figures 19
    2.6 References 22

3. HYBRID PLASMA EQUIPMENT MODEL 23
    3.1 Introduction 23
    3.2 The Electromagnetics Module 24
    3.3 The Electron Energy Transport Module 25
        3.3.1. Electron Energy Equation Method 26
        3.3.2. Electron Monte Carlo simulation 27
    3.4 The Fluid-Chemical Kinetics Module 29
    3.5 External Modules 32
    3.6 Figures 33
    3.7 References 34

4. MONTE CARLO RADIATION TRANSPORT MODEL 35
    4.1 Description of Model 35
    4.2 Lineshape 37
    4.3 Frequency Redistribution 41
    4.4 Hyperfine Splitting and Isotopes 42
    4.5 Tables 44
    4.6 Figures 45
    4.7 References 46

5. RADIATION TRANSPORT IN ELECTRODELESS LAMPS 47
    5.1 Introduction 47
    5.2 Base Case Geometry and Plasma Parameters 47
    5.3 Effects of Plasma Conditions on Radiation Transport 49
    5.4 Lamp Geometry and Radiation Transport 52
    5.5 Isotopic Effects of Mercury 55

5.6 Radiation Trapping and Electron Energy Distributions 56
5.6.1. Electron Energy Distributions for the Base Case 57
5.6.2. Effects of Radiation Trapping 58
5.7 Conclusions 61
5.8 Tables 62
5.9 Figures 66
5.10 References 78

6. FLUOROCARBON PLASMAS…………… 79
6.1 Etching Plasmas 79
6.2 Plasma Processing of Low-k Dielectrics 80
6.3 Plasmas for Deposition 82
6.4 Role of Modeling 83
6.5 Summary 84
6.6 Figures 86
6.7 References 91

7. SURFACE KINETICS MODEL…………… 95
7.1 Introduction 95
7.2 Description of Surface Kinetics Model 96
7.3 Surface Reaction Mechanisms in Fluorocarbon Plasma Etching of SiO_2 100
7.4 Summary 104
7.5 Tables 105
7.6 Figures 112
7.7 References 114

8. POLYMER FILMS IN FLUOROCARBON ETCHING PLASMAS 116
8.1 Introduction 116
8.2 C_4F_8 Plasmas 116
8.2.1. Base Case Plasma Parameters 116
8.2.2. SiO_2 Etch Rates and Polymer Film Properties 117
8.2.3. Ion-induced Defluorination 119
8.2.4. Parameterizations 120
8.3 Polymer Film Properties in C_2F_6 Plasmas 121
8.4 Summary 122
8.5 Figures 124
8.6 References 134

9. ETCHING IN C_4F_8 / ARGON PLASMAS : EFFECT OF UV RADIATION 136
9.1 Introduction 136
9.2 UV Photon Surface Reactions 137
9.3 Radiation Trapping in C_4F_8/Ar Plasmas 139
9.4 Etch Rates in C_4F_8/Ar Plasmas 141
9.5 Summary 144
9.6 Figures 145
9.7 References 156

10. CONCLUSIONS AND FUTURE EXTENSIONS 157
10.1 Conclusions 157
10.2 Future Extensions 159

APPENDIX A: LIST OF REACTIONS FOR Ar/Hg 160
A.1 References 164

APPENDIX B: LIST OF REACTIONS FOR C_4F_8 / Ar 165
B.1 Electron Impact Excitation, Ionization, and Dissociation Reactions 165
B.2 Neutral Heavy Particle Reactions 170
B.3 Ion-molecule Reactions 172
B.4 Ion-ion and Ion-electron Reactions 176
B.5 References 180

APPENDIX C: LIST OF REACTIONS FOR C_2F_6 / Ar 184
C.1 References 188

AUTHOR'S BIOGRAPHY 189

1. TECHNOLOGICAL PLASMAS

1.1 Plasma Physics

Plasma physics refers to the study of collections of gaseous charged particles and neutrals, that show collective behavior, and are on a large enough spatial scale quasi-neutral. Plasmas are the most common form of matter, comprising more than 99% of the visible universe. The defining characteristics of a plasma is its degree of ionization and its electron temperature. As seen in Fig 1.1, the range of plasmas includes high-pressure gases with a small fraction of the atoms ionized and relatively low charged-particle temperatures - for example, plasmas used in computer-chip processing and light sources - to those in very low density gases with a large fraction of the gas atoms ionized and very high temperature charged particles - for example, fusion plasmas.[1,2]

In this dissertation, the focus of work will be on "technological" plasmas. These are "cold" plasmas, with electron temperatures between 0.1-10 eV, and electron densities on the order of 10^{10} - 10^{12} cm^{-3}, which represents a low degree of fractional ionization. Applications of these plasmas are shown in Table 1.1. In general, these plasmas serve as power transfer media (Fig 1.2), where power from a wall socket is deposited in the plasma via dc, inductive or capacitive coupling. The fields so generated accelerate the electrons that strike the neutral gas in the chamber, ionizing and exciting the constituents. This leads to the formation of reactive species like ions and radicals, which are then used in the plasma processing technology of choice. For example, for etching of semiconductors, the ions are the primary activators of the etching process.[3,4] In lamps,

the light is generated from excited state species.[5,6] For atmospheric pressure gas remediation, neutral radicals are the primary reactive species.[7,8]

In this dissertation, technological plasmas are studied in the context of lighting plasmas, as well as fluorocarbon plasmas for surface modification. The regimes of underlying physics in both cases are different. Lamps work at higher pressures (0.1 – 10s of Torr) in sealed cavities, while semiconductor modification is performed at low pressures (few mTorr) in systems with flow and (in this case) with electronegative gases. The common feature that ties these two applications is the plasma production of UV photons, either intentional or unintentional, and the transport of those photons to surfaces. Many processes which are important to design of technological devices are still not understood at the level of detail and sophistication required to perform such designs from first principles. This work addresses two such issues: the transport of radiation in a low pressure lamp, and the mechanisms for surface modification in fluorocarbon plasma, as well as the assessment of the importance of radiation-surface interaction in semiconductor processing.

1.2 Overview of the dissertation

The resonance radiation emitted by an atom may be absorbed and re-emitted by other atoms of the same species many times in the plasma during its transit from the initial sites of emission to leaving the plasma or striking a surface. This process, commonly called radiation trapping or imprisonment, lengthens the effective lifetime of the excited radiative state as viewed from outside the lamp.[9] Radiation transport is an important consideration for designing new generation of highly efficient electrodeless lamps.[10] As such, there is a need to couple radiation transport to the plasma processes

in the lamp to properly account for an accurate evolution of parameters as a function of, for example, operating pressure, power and geometry. To this end, a Monte Carlo Radiation Transport Module (MCRTM) was developed and interfaced with a 2-dimensional plasma equipment model, the Hybrid Plasma Equipment Model (HPEM).[11] The combined model was applied to analyses of Hg/Ar lamps having geometries similar to those commercially available (Philips QL and Matsushita Everlight).[10,12] We found that coupling of the plasma kinetics to the MCRTM led to significant spatial variations in densities and temperatures of photon radiating and absorbing species. In select cases, these spatial inhomogeneities had measurable effects on radiation trapping. Second-order effects of radiation transport on the electron energy distributions were also quantified. A detailed overview of electrodeless lamps and radiation transport is given in Chapter 2. The description of the HPEM is in Chapter 3, and the description of the MCRTM is in Chapter 4. The results of our investigation are discussed and summarized in Chapter 5.

Chapters 6 through 8 deal with the modeling of the polymer films formed in fluorocarbon plasmas at various process regimes. Chapter 6 is an introduction to the applications of fluorocarbon plasmas, in the context of both etching as well as deposition processes. Chapter 7 contains a description of the Surface Kinetics Model (SKM) used to model the evolution of the surface. The results obtained from interfacing the SKM with the HPEM, for a two-dimensional description of the etching process, are detailed in Chapter 8. We found that ion-induced defluorination is an important process leading to fluorine that participates in etching.

Just as lighting plasmas produce UV photons, so do semiconductor plasmas. The consequences of UV illumination of, for example, polymers in etching plasmas has not previously been addressed. In Chapter 9, we discuss results of investigations where we combined the MCRTM and the SKM to investigate C_4F_8/Ar etching plasmas. This study is of significance because of the importance of the UV radiation-induced damage during semiconductor processing.[13] The UV radiation affects the state of fluorination of the carbon atoms in the polymer film via bond-breaking, and also take parts in crosslinking processes.[14] As a proof-of-principle study, we assumed that the UV radiation participates in photon-induced defluorination. We found that the change in etch rates was not appreciable, and this was due to the low fluorine content of the polymer film.

In Chapter 10, conclusions are made about the overall significance of the work and recommendations for future work are suggested.

1.3 Tables

Processing:
- Surface Processing
- Nonequilibrium (low pressure)
- Thermal (high pressure)

Volume Processing:
- Flue gas treatment
- Metal recovery
- Waste treatment

Chemical Synthesis:
- Plasma spraying
- Diamond film deposition
- Ceramic powders

Light Sources:
- High intensity discharge lamps
- Low pressure lamps
- Specialty sources

Surface Treatment:
- Ion implantation
- Hardening
- Welding
- Cutting
- Drilling

Propulsion

Flat-Panel Displays:
- Field-emitter arrays
- Plasma displays

Radiation Processing:
- Water purification
- Plant growth

Switches:
- Electric power
- Pulsed power

Energy Converters:
- MHD converters
- Thermionic energy converters

Medicine:
- Surface treatment
- Instrument sterilization

Isotope Separation

Beam Sources

Lasers

Material Analysis

Table 1.1. Some applications of technological plasmas

1.4 Figures

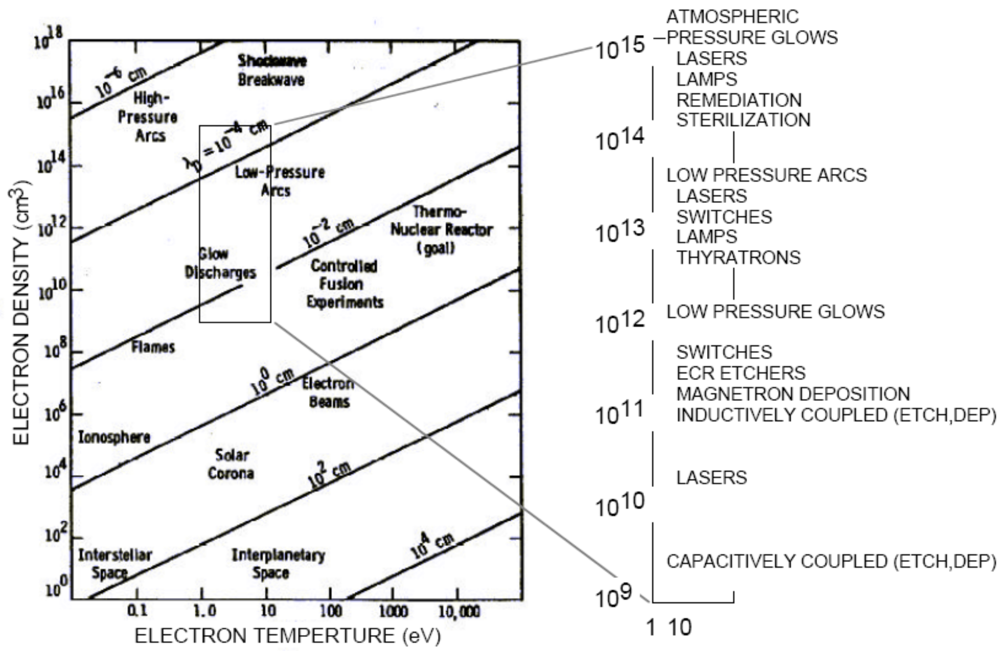

Figure 1.1. Range and overview of plasmas. The box shows the range of technological plasmas.

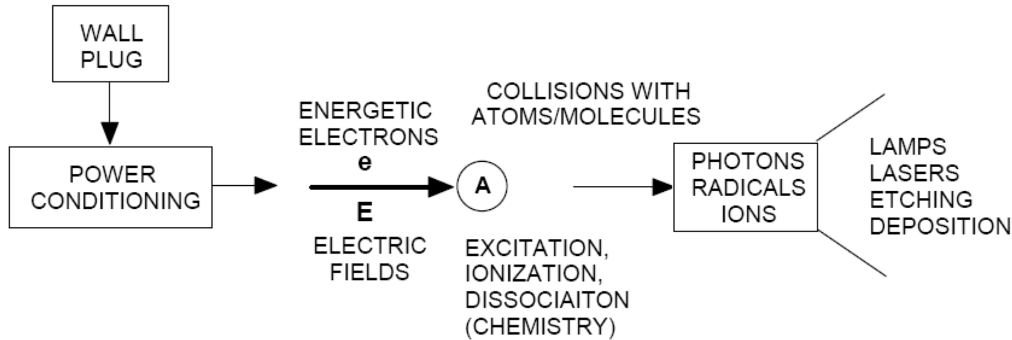

Figure 1.2. Technological plasmas as power transfer media. Power from the wall plug gets converted, via inductive/capacitive coupling, to electric fields, which then accelarate electrons, which take part in inelastic processes, creating radicals and ions for the plasma processing technology of choice.

1.5 References

1. National Research Council, Plasma Science: From Fundamental Research to Technological Applications (National Academy Press, Washington D.C., 1995).
2. Perspectives on Plasmas, www.plasmas.org.
3. G. S. Oehrlein and J. F. Rembetski, IBM J. Res. Develop. **36**, 140 (1992).
4. Plasma Etching: An Introduction. Edited by D. M. Manos and D. L. Flamm, Academic Press, 1989.
5. A. F. Molisch and B. P. Oehry, Radiation Trapping in Atomic Vapours (Clarendon Press, Oxford, 1998).
6. J. Waymouth, Electric Discharge Lamps, (MIT Press, Cambridge, 1971).
7. D. Evans, L. A. Rosocha, G. K. Anderson, J. J. Coogan, and M. J. Kushner, J. Appl. Phys. **74**, 5378 (1993).
8. K. Urashima and J.-S. Chang, IEEE T. Dielec El. In. **7**, 602 (2000).
9. T. Holstein, Phys. Rev. **72**, 1212 (1947).
10. A. Netten and C.M. Verheij, QL lighting product presentation storybook (Philips Lighting, Eindhoven, Product Literature, 1991; Updated 1994).
11. K. Rajaraman and M. J. Kushner, J. Phys. D. **37**, 780 (2004).
12. M. Shinomaya, K. Kobayashi, M. Higashikawa, S. Ukegawa, J. Matsuura, and K. Tanigawa, J. Ill. Engg. Soc. **44** (1991).
13. J. L. Lauer, J. L. Shohet, and R. W. Hansen, J. Vac. Sci. Technol. A **21**, 1253 (2003).
14. C. Decker, Polym. Int. **51**, 1141 (2002).

2. INTRODUCTION TO RADIATION TRANSPORT

2.1 Discharge Lamps

Electric discharge lamps are undoubtedly one of the most economically important plasma devices in use today. Due to this widespread use, even small improvements in lamp efficiency have tremendous impact on world-wide energy consumption. Rough estimates show that if the efficiency of electric discharge lamps could be increased by about 1%, this would lead to savings of 10^9 kWh per year worldwide.

Fluorescent lamps are low pressure discharges, operating at gas temperatures of 300-700 K, with electron temperatures 1-2 eV. Conventional fluorescent lamps are filled with a rare gas, typically argon at around 3 Torr pressure, with a minority of mercury (typically a few millitorr). Between 60-70% of electrical power in these discharges is converted to UV radiation (185 nm, 254 nm) by mercury atoms. A phosphor is then used to convert the UV to visible light, resulting in a total electrical conversion efficiency of about 25%. These are non-LTE (local thermal equilibrium) discharges, meaning that the electrons, ions and neutral species have different temperatures at each point in the plasma.

HID (High Intensity Discharge) lamps are LTE (local thermodynamic equilibrium) discharges that operate at a few atmospheres of pressure, where the majority species is usually mercury or another vaporized metal such as sodium. Both gas and electron temperatures are $\approx$ 1000 K near the wall and $\approx$ 6000 K near the center the discharge. HID lamps directly produce light in the visible spectrum. Metal halide salts

are often added to improve color rendering. Typical uses of HID lamps are for roadway, projector and high quality indoor lighting.

Electric discharge lamps have been studied extensively, and empirically optimized by the industrial sector. In spite of these efforts, the fundamental physical processes that determine the lamp efficiency are not well known. The physical processes that occur in low- and high-pressure lamps are extremely complex, combining charged and neutral particle transport, non-Maxwellian electron energy distribution functions, and chemical reactions between filling and cathode material. In this regard, determination of the relevant transport cross-sections is very difficult, as data in the literature still show considerable discrepancies. Of most fundamental importance to us, the process of radiation transport and trapping has historically been treated using only approximate methods.

To address both the physics and technology of improving the efficiency of electric discharge lamps, my research has involved developing new algorithms for the modeling of low pressure lamps. In work to date, models for radiation transport in electrodeless discharges have been developed. The outcome of this work will be useful to lamp designers in providing them with knowledge of the plasma parameter profiles in lamps, as well as giving them the opportunity to understand novel emitting materials. The potential impact to society is in the form of increased savings and more environmentally friendly technologies due to an improved ratio of light output to electrical power.

2.2 Electrodeless Lamps

Electron impact excitation of the ground state Hg $^1S_0$ atoms in fluorescent lamps results in Hg excited states ($^3P_1$, $^3P_0$, $^1P_1$, $^3P_2$), shown in Fig. 2.1. These atoms then either decay back to the ground state emitting a resonance photon, or are ionized by collisions with other excited atoms or by electrons. The "useful" output of the lamp is the resonance radiation at 185 nm and 254 nm that reaches the walls of the lamp.

In conventional fluorescent lamps, the plasma is sustained by direct or low-frequency alternating currents, which require electrodes within the lamp to maintain the discharge. The presence of electrodes places severe restrictions on lamp design and is a major cause of failure, therefore limiting lamp life. These lamps operate with thermionic cathodes to reduce the voltage drop in the cathode fall, thereby improving efficiency and reducing sputtering of the cathode. An electron emitting material (such as barium oxide) is typically impregnated onto the electrode. The evaporation of the emitter material during lamp operation increases the voltage drop at the electrode beyond that available from the power supply in addition to darkening of the tube. Both eventually result in lamp failure.

Recent developments in lamp technology have led to the introduction of electrodeless products, in which the power is introduced in the discharge by inductive coupling of radio frequency power from an antenna. An example is the Philips QL lamp, shown in Fig 2.2. Apart from increasing the life of the lamp due to the absence of electrodes, the possibilities exist for using new, possibly corrosive chemistries, which would otherwise damage the electrode in the conventional lamps.

2.3 Radiation Transport

The resonance radiation emitted by an atom may be absorbed and re-emitted by other atoms of the same species many times in the plasma during its transit from the initial sites of emission to striking the phosphor. This process, commonly called radiation trapping or imprisonment, lengthens the effective lifetime of the excited state as viewed from outside the lamp.[3] The time required for any given quanta of energy to escape the plasma is longer due to this series of absorption and re-emission steps.

Radiation trapping by itself is not necessarily detrimental to operation of the lamp or to its efficiency. In the absence of other processes, the photons do eventually escape, as in the steady state the rate of photon escape equals the rate of initial generation of quanta. The longer effective lifetime of the excited states, however, increases the likelihood that collisional processes will quench the excitation prior to escape, thereby reducing the net number of photons escaping the plasma. Second order effects resulting from the lengthened lifetime of the resonance level include changes in the ionization balance (due to multistep ionization from the excited state) and electron temperature. Quantifying and perhaps controlling radiation trapping is therefore an important design consideration for improving the efficiency of lamps.

2.3.1 Broadening Mechanisms

Spectral lines emitted by atoms are broadened and shifted by at least three different processes:

Natural broadening is caused by the finite lifetime of the atomic levels. The natural linewidth of the spectral line is

$$\Delta\nu_n = \frac{1}{2\pi}\left(\frac{1}{\tau_1} + \frac{1}{\tau_2}\right) \qquad (2.1)$$

where τ_1 and τ_2 are the lifetimes of the lower nd upper levels. The probability that a photon of frequency ν is emitted/absorbed is given by

$$k(\nu) = k_0\left[1+\left(\frac{2(\nu-\nu_0)}{\Delta\nu_n}\right)^2\right]^{-1} \qquad (2.2)$$

where $k(\nu)$ is the emission/absorption coefficient at frequency ν, and k_0 is the absorption coefficient at line center ν_0.

Pressure (or collisional) broadening results from the perturbation of energy levels due to the collision with other atoms or electrons. There are two theories to account for these processes:

- Lorentz theory - In this theory, the lineshape due to collisions is of the same form as in natural broadening, with $\Delta\nu_n$ replaced by $\Delta\nu_c$, the collision width. $\Delta\nu_c$ is the collision frequency of each atom with the other species in the plasma. It is dependent on the density of the collision partners, as well as its transport properties in the plasma. In this case, the lineshape does not depend on the type of interactions between atoms.
- Statistical theory - This is only valid in the far wings of the lineshape. Here the lineshape depends on the type of interaction force with the "disturbing" atoms.

Doppler broadening is due to the random thermal motion of the gas atoms in the vapor cell. Both the emission and absorption frequencies are Doppler shifted. In thermal equilibrium, the Maxwellian velocity distribution of the atoms results in an emission/absorption coefficient with a Gaussian profile

$$k(\nu) = k_0 . \exp\left[-\left(\frac{2(\nu - \nu_0)}{\Delta\nu_D} \sqrt{\ln 2} \right)^2 \right], \qquad \Delta\nu_D = \frac{2}{c} \sqrt{\frac{2\ln(2) k_B T}{M}} \nu_0 \tag{2.3}$$

where ν_0 is the center frequency for the line (254 or 185 nm for the case of Hg), $\Delta\nu_D$ is the Doppler width, T is the gas temperature, k_B is the Boltzmann constant, and M is the atomic mass.

The most important broadening process in sub-Torr fluorescent lamps is Doppler broadening. For intermediate pressures, however, it is more realistic to use a combination of all the three types of broadening, resulting in what is called a Voigt profile. The probability that a photon will be absorbed/emitted at any frequency is given by

$$g(\nu) = \frac{a}{\pi^{3/2}} \int_{-\infty}^{\infty} \frac{\exp(-y^2)}{a^2 + (\nu - y)^2} dy \tag{2.4}$$

where a is the ratio of the sum natural and pressure broadened widths to the Doppler width, and ν is the frequency departure from line center in units of the Doppler width. A comparison of Voigt and Doppler profiles is shown in Fig. 2.3.

2.3.2 Theory of Radiation Transport

The physical process of radiation trapping bears a strong resemblance to particle diffusion. Milne, therefore, combined the equation for radiative transfer and the equation of radiative equilibrium to arrive at a modified diffusion equation.[4] Here, the lineshape is replaced by an equivalent box-shaped line, and the photon mean free path is $1/\bar{k}$. The equation for radiative transfer, found by computing the gains and losses of a pencil of radiation during a path length ds, is given by

$$\frac{1}{N\bar{k}}\frac{dI_\nu}{ds} = -\left(n_1 - n_2\frac{q_1}{q_2}\right)I_\nu + n_2\frac{q_1}{q_2}\sigma, \quad \sigma = \frac{2h\nu^3}{c^2} \tag{2.5}$$

where I_ν is the intensity of radiation, n_1 and n_2 are the number densities of atoms in the ground and excited states respectively, N is the total number density, and q_1 and q_2 are the statistical weights of the ground and excited states, respectively. The equation of radiative equilibrium states that, in the absence of any other source of excitation, the difference in number of emission and absorptions is equal to the rate of increase in the number of excited atoms. This gives us

$$\nabla^2\left[n_2(\mathbf{r},t) + \tau\frac{\partial n_2(\mathbf{r},t)}{\partial t}\right] = 4\bar{k}^2\tau\frac{\partial n_2(\mathbf{r},t)}{\partial t} \tag{2.6}$$

where n_2 is the excited state density, and **r** is the position in the cell, and τ is the natural radiative lifetime of the excited state. The additional term to the diffusion equation (the second term) describes the natural decay of the excited states. However, this concept of a frequency averaged mean free path leads to an infinite mean free path which is not

physical. This method however, works for low opacities, where the error of replacing the lineshape with a box-shape is quite small. At higher opacities, the absorption coefficent k varies with frequency, and the diffusion formalism must be replaced by a more accurate treatment.

Holstein and Biberman realised that radiation transport is non-local in real space and thus is best described by an integral transport equation rather than the differential equation of diffusive transport.[5,6] Holstein proceeded to derive what he called the transmission factor T(x), defined as the probability that a photon will traverse a distance x without being absorbed. This is given by

$$T(x) = \int_0^\infty \phi(\nu) \exp(-k(\nu)x) d\nu \tag{2.7}$$

where ϕ is the lineshape function. This transmission factor is then used to derive a Green's function for photon transport

$$G(\mathbf{r},\mathbf{r'}) = -\frac{1}{4\pi l^2} \frac{\partial}{\partial x} T(x), \qquad x = |\mathbf{r} - \mathbf{r'}| \tag{2.8}$$

A rate equation for the excited-state atoms can then be written, assuming no excitation after t=0 (so the excited atoms decay only radiatively)

$$\frac{\partial n(\mathbf{r},t)}{\partial t} = -\frac{1}{\tau} n(\mathbf{r},t) + \frac{1}{\tau} \int_V n(\mathbf{r'},t) G(\mathbf{r},\mathbf{r'}) d\mathbf{r'} \tag{2.9}$$

where τ is the natural radiative lifetime of the excited state. The excited state can then be written as a superposition of states,

$$n(\mathbf{r}, t) = \sum_{j=1}^{\infty} c_j n_j(\mathbf{r}) e^{-g_j t/\tau} \tag{2.10}$$

where c_j are determined by the initial distribution, and the trapping factors g_j are geometry dependent. At later times the distribution is determined by the lowest g value, called the fundamental mode decay factor. Holstein derived asymptotic approximations for the fundamental mode decay rate for Doppler and Lorentz lines for a cylinder having radius R

$$g_D = \frac{1.60}{k_0 R[\ln(k_0 R)]^{1/2}}, \qquad g_L = \frac{1.125}{[\pi k_0 R]^{1/2}} \tag{2.11}$$

The decay rates for the fundamental modes of this equation have been computed exactly for simplistic geometries in Doppler or pressure-broadened regimes.[7,8] This calculation is direct because of the simplicity of the kernel function. The spatial distribution of emitters must be fairly simple to enable the integration of the resulting Green's function for transport of photons. Inherent to this method is the full spectral redistribution of radiation upon re-emission. That is, the frequency of the emitted photon within the lineshape function is independent of the absorption frequency. To date, most lamps have had simple geometries, and have operated at high enough opacities for the

Holstein analysis to provide acceptable solutions. In cases where there are complex geometries or distributions of radiators and absorbers, one must resort to numerical methods to solve for the decay rates and trapping factors.

2.4 Numerical Methods for Radiation Transport

Monte Carlo methods, first popularized by Anderson et al,[9] are well suited to addressing radiation transport where the spatial distributions of absorbers and radiators are complex or change in time, or Partial Frequency Redistribution (PFR) may be important.[10-12] In simple geometries, the distributions for the ground and excited state densities can be estimated or parameterized. In this regard, Lawler and coworkers have developed semi-empirical expressions for radiation trapping factors in cylindrical geometries using Monte Carlo and propagator function techniques for fundamental mode distributions and radially symmetric inhomogeneities.[13] They found that the trapped lifetimes of resonance radiation of Hg in Ar/Hg plasmas, as measured externally of the plasmas, are not significantly affected by moderate inhomogeneities in absorber densities, though the excited atom distributions are.[12] These trends are shown in Fig. 2.4. They also investigated the transport of photons produced by the 185 nm transition [14] and the consequences of foreign gas broadening.[15]

In more dynamic systems, a self-consistent plasma model that accounts for the evolution of gas densities, temperatures and other plasma parameters may be necessary. The need for such coupled models has been recently addressed by Lee and Verboncoeur, who developed a radiation transport model coupled to a particle-in-cell simulation, and have applied it to a 1-dimensional planar Ar discharge.[16,17] Their results agree well

with Holstein eigenmode analyses for radiation trapping factors.(See Fig 2.5) They have performed a power loss balance analysis and showed that in Ar discharges, the radiation loss can be a very significant fraction of the total power loss, which emphasizes the importance of understanding radiation transport well.

2.5 Figures

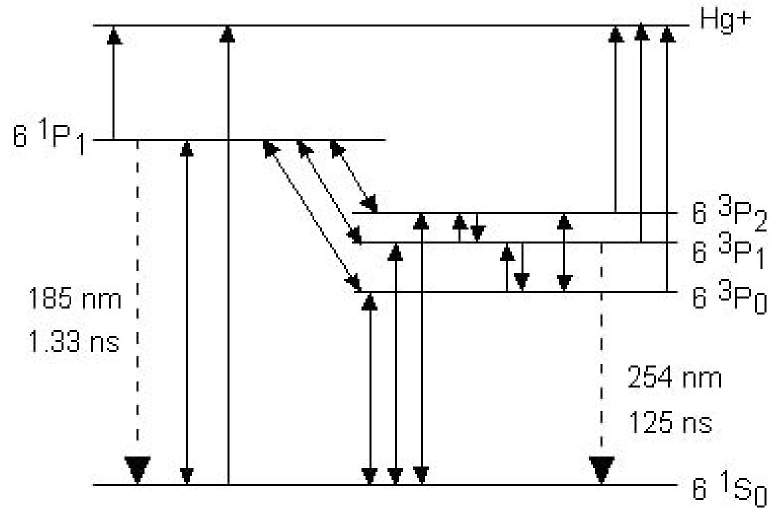

Figure 2.1. Energy diagram for Hg. Solid lines indicate electron impact reactions.

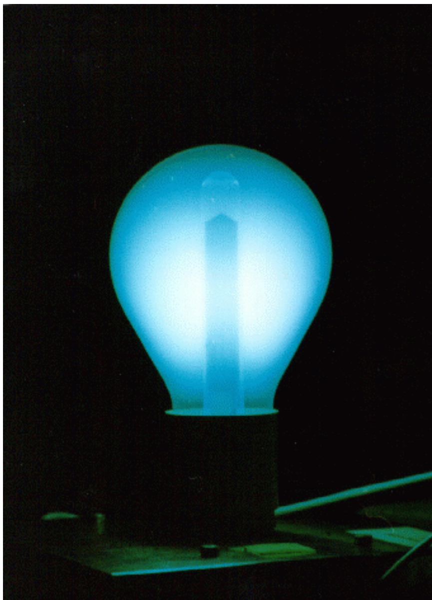

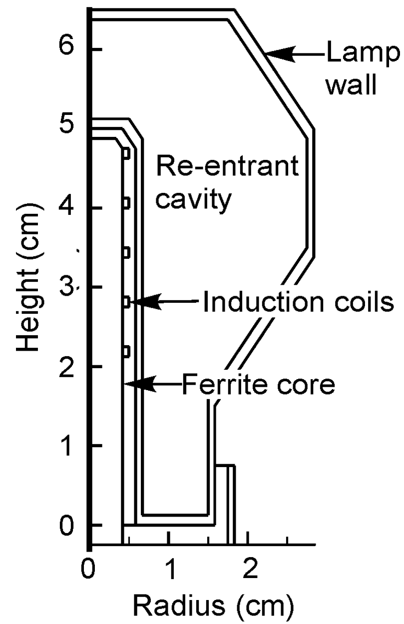

Figure 2.2. Philips QL Lamp in operation (left) and a schematic used for the modeling study (right)

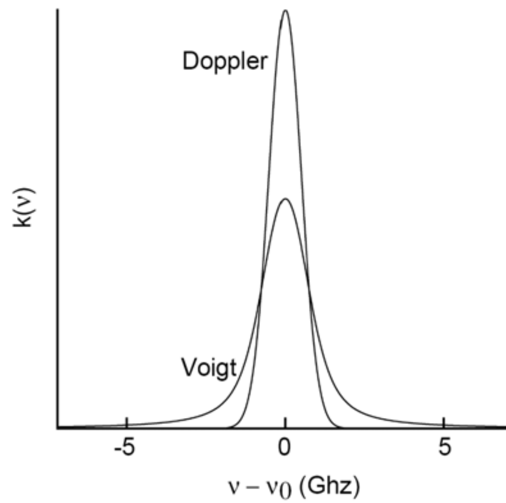

Figure 2.3. A Voigt profile is compared with the Doppler profile at the same pressure and temperature. It is seen that the Voigt profile extends over a larger range of frequencies because of the natural and collisional broadening.

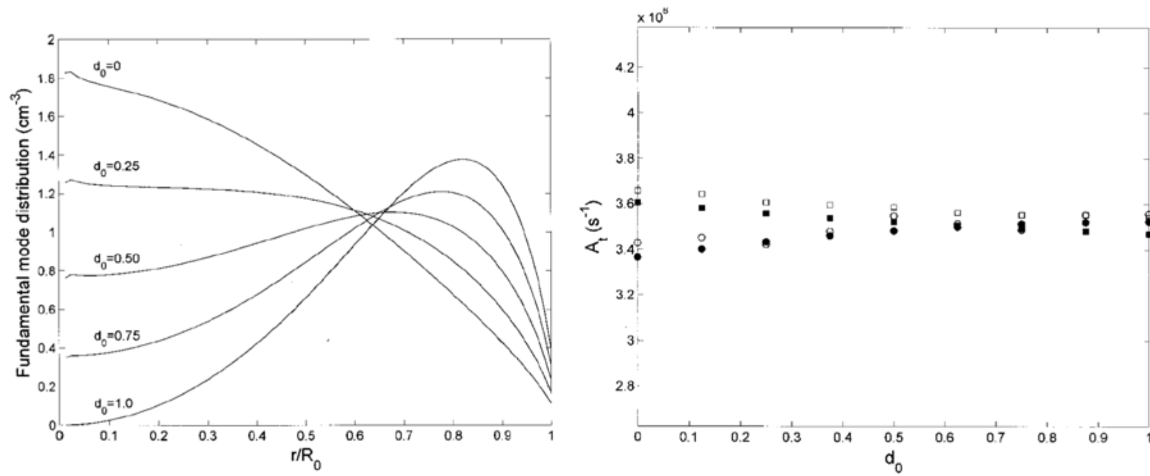

Figure 2.4. Results from J. E. Lawler's study on inhomogeneities.[15] d_0 is a factor that shows the extent of inhomogeneity (as shown in the left figure). A is the inverse effective lifetime of the 185 nm line, and is moderately affected by inhomogeneities.

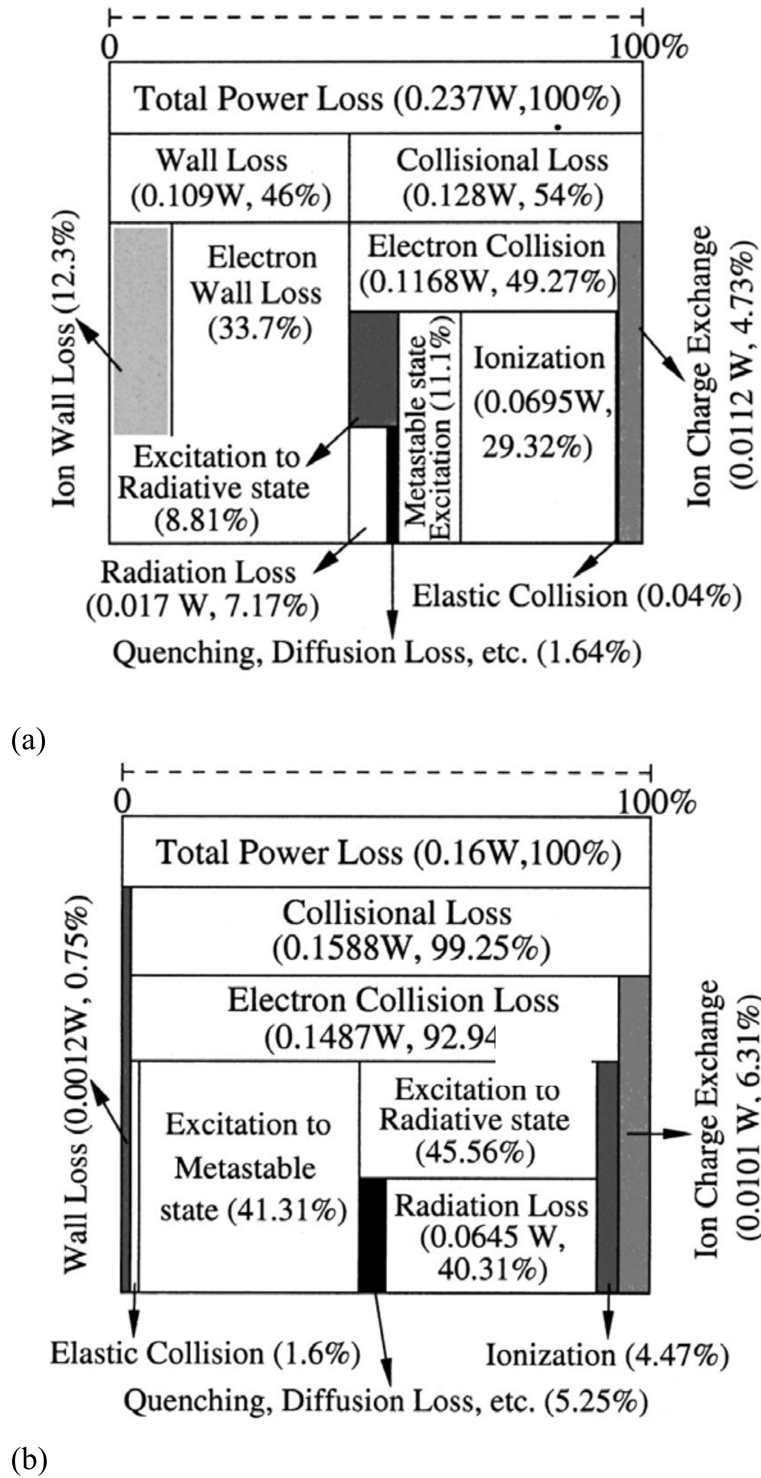

Figure 2.5. Results from Lee and Verbonceour's work on 1D model of an Ar discharge. Figure (a) is at P=6 mTorr, R=1 cm, and I=5.4 mA. Figure (b) is at P=0.5 Torr, R=0.2 cm, I=0.154 mA. Radiation loss is seen to be a significant fraction of total power loss.[17]

2.6 References

1. M. Shinomaya, K. Kobayashi, M. Higashikawa, S. Ukegawa, J. Matsuura, and K. Tanigawa, J. Ill. Engg. Soc. **44** (1991).
2. J. M. Anderson, US Patent 3,500,118, March 1970.
3. A. F. Molisch and B. P. Oehry, Radiation Trapping in Atomic Vapours (Clarendon Press, Oxford, 1998).
4. E. A. Milne, J. London Math Soc. **1**, 40 (1926).
5. T. Holstein, Phys. Rev. **72**, 1212 (1947).
6. L. M. Biberman, Zh. Eksp. Theor. Fiz. **17**, 416 (1947).
7. C. van Trigt, Phys. Rev. A **4**, 1303 (1971).
8. C. van Trigt, Phys. Rev. A **13**, 726 (1976).
9. J. B. Anderson, J. Maya, M. W. Grossman, R. Lagushenko, and J. F. Waymouth, Phys. Rev. A **31**, 2968 (1985).
10. T. J. Sommerer, J. Appl. Phys. **74**, 1579 (1993).
11. J. E. Lawler, G. J. Parker, and W. N. G. Hitchon, J. Quant. Spect. Rad. Transf. **49**, 627 (1993).
12. J. J. Curry, J. E. Lawler, and G. G. Lister, J. Appl. Phys. **86**, 731 (1999).
13. J. E. Lawler and J. J. Curry, J. Phys. D: Appl. Phys. **31**, 3235 (1998).
14. K. L. Menningen and J. E. Lawler, J. Appl. Phys. **88**, 3190 (2000).
15. J. E. Lawler, J. J. Curry, and G. G. Lister, J. Phys. D **33**, 252 (2000).
16. H. J. Lee and J. P. Verboncoeur, Phys. Plasmas **8**, 3077 (2001).
17. H. J. Lee and J. P. Verboncoeur, Phys. Plasmas **8**, 3089 (2001).

3. HYBRID PLASMA EQUIPMENT MODEL

3.1 Introduction

The Hybrid Plasma Equipment model (HPEM) has been developed at the University of Illinois for simulating low-temperature, low-pressure plasma processes [1-6]. The HPEM is capable of modeling a wide variety of plasma processing conditions and reactor geometries. The HPEM addresses plasma physics and chemistry in three main modules: The Electromagnetics Module (EMM), the Electron Energy Transport Module (EETM), and the Fluid-chemical Kinetics Module (FKM). The roles of the modules are:

1. The EMM computes the inductively coupled electric fields determined by inductive coils, and the magnetostatic fields induced by permanent magnets or dc current loops. This requires an initial guess of plasma properties for the first iteration.
2. These fields are then passed to the EETM, which calculates electron kinetic properties such as electron energy distribution function, electron temperature, and electron impact rate coefficients. The electron impact reaction cross-sections are looked up from a database describing electron collision cross sections.
3. Results of the EETM are transferred to the FKM to determine plasma source and sink terms. The FKM solves the fluid continuity equations for species densities and plasma conductivity. Electrostatic fields are also derived in the FKM by either solving Poisson's equation or assuming quasi-neutrality. The outputs of the FKM are then fed back to the EMM and EETM modules. The whole process iterates until the results reach a preset convergence criterion.

3.2 The Electromagnetics Module

The electromagnetics module (EMM) computes time varying electric and magnetic fields for the HPEM. For an inductively coupled plasma, rf currents passing through the inductive coil generate azimuthal electric fields. The EMM module calculates the spatially dependent azimuthal electric fields by solving Maxwell's equation under time harmonic conditions. With azimuthal symmetry, Maxwell's equation for electric field is

$$-\nabla \cdot \frac{1}{\mu} \nabla E_{\phi} = \omega^2 \varepsilon E_{\phi} - j\omega J_{\phi} \tag{3.1}$$

where μ is the permeability, ε is the permittivity, ω is the driving frequency, and the current J_{ϕ} is the sum of the driving current J_o and the conduction current in the plasma. The conduction current is assumed to be of the form $J_{\phi}=\sigma E_{\phi}$. For collisional plasmas, the conductivity of the plasma is

$$\sigma = \frac{q_e^2 n_e}{m_e} \frac{1}{\nu_{me} + i\omega} \tag{3.2}$$

where q is the charge, n_e is the electron density, m is the mass, and ν_m is the momentum transfer collision frequency.

The static magnetic fields in the axial and radial directions are also determined in the EMM. The magnetic field, under consitions of azimuthal symmetry, can be represented by a vector potential **A** with only an azimuthal component. **A** satisfies the following equations:

$$\nabla \times \frac{1}{\mu} \nabla \times \mathbf{A} = j, \qquad B = \nabla \times \mathbf{A} \tag{3.3}$$

where j is the source terms due to closed current loops at mesh points representing permanent magnets or dc coils. This equation, as well as the electric field equation, are solved using successive over relaxation (SOR).

3.3 The Electron Energy Transport Module

The electric and magnetic fields computed in the FKM and EMM affect the electron transport properties and impact sources. The electron impact reaction rates strongly depend on the electron temperature T_e, which is related to the electron energy distribution (EED) as

$$T_e = \frac{3}{2} \int f(\varepsilon).\varepsilon.d\varepsilon, \tag{3.4}$$

where ε represents electron energy and $f(\varepsilon)$ is the electron energy distribution. Inelastic collisions influence the EED by extracting energy from the electrons, resulting in a reduction of the high-energy tail of the EED. The Electron Energy Transport Module

(EETM) was designed to simulate these effects. There are two methods for determining these parameters. The first method determines the electron temperature by solving the electron energy equation. The second method uses a Monte Carlo Simulation to launch electron particles and collect statistics to generate the EEDF.

3.3.1 Electron Energy Equation Method

The zero-order Boltzmann equation is solved to obtain an electron energy distribution for a range of E/N values. This directly leads to the computation of an electron temperature as $Te = 2\langle \varepsilon \rangle / 3$, where $\langle \varepsilon \rangle$ is the average energy.

In the case of a weakly collisional plasma, the kinetics of electrons are described by the Boltzmann equation:

$$\frac{\partial f_e}{\partial t} + v.\nabla_r f_e - \frac{e(E + v \times B)}{m_e}.\nabla_v f_e = \left(\frac{\delta f_e}{\delta t} \right)_{collision}, \tag{3.5}$$

where $f_e = f_e(t, r, v)$ is the electron distribution function, ∇_r is the spatial gradient, ∇_v is the velocity gradient, m_e is the electron mass, and $\left(\frac{\delta f_e}{\delta t} \right)_{collision}$ represents the effect of collisions. The information from the zero-dimensional Boltzmann equation is used in the solution of the electron energy equation

$$\nabla k \nabla T_e + \nabla \cdot (\Gamma T_e) = P_{heating} - P_{loss} \tag{3.6}$$

where k is the thermal conductivity, Γ is the electron flux determined by the FKM, T_e is the electron temperature. $P_{heating}$ is the power added due to conductive heating equal

to $\mathbf{j} \cdot \mathrm{E}$. The current density and electric field are determined in the FKM. The electric field is the sum of the azimuthal field from the EMM and the radial and axial field found in the FKM. P_{loss} is the power loss due to collisions by the electrons.

3.3.2 Electron Monte Carlo Simulation

The electron Monte Carlo simulation (EMCS) integrates trajectories of electron pseudo particles in the electromagnetic fields obtained from the EMM module and the electrostatic fields obtained from the FKM. Initially the electrons are given a Maxwellian distribution and distributed in the reactor weighted by the current electron density (from the FKM). Particle trajectories are computed using the Lorentz equation,

$$\frac{d\overline{v}}{dt} = \frac{q_e}{m_e}\left(\overline{E} + \overline{v} \times \overline{B}\right) \tag{3.7}$$

where $\overline{v}$, $\overline{E}$, and $\overline{B}$ are the electron velocity, local electric field, and magnetic field respectively. Equation 3.7 is updated using a second order implicit integration method. The electron energy range is divided into discrete energy bins. Within an energy bin, the collision frequency, ν_i, is computed by summing all the possible collisions within the energy range

$$\nu_i = \left(\frac{2\varepsilon_i}{m_e}\right)^{\frac{1}{2}} \sum_{j,k} \sigma_{ijk} N_j \ , \tag{3.8}$$

where ε_i is the average energy within the bin, σ_{ijk} is the cross section at energy *i* for the species *j* and collision process *k*, and N_j is the number density of species *j*. Null collision

cross sections are employed to provide a constant collision frequency. The integration time step is given by the minimum of the time required to traverse a specified part of the computational cell, a specified fraction of the rf period, and $\tau = -\frac{1}{\nu_i}\ln(r)$, where r is a random number distributed on (0,1). After the free flight, the type of collision is determined by the energy of the pseudoparticle. The corresponding energy bin in referenced and a collision is randomly selected from that energy bin, with a null reaction making up the difference between the maximum and actual collision frequency.

Statistics are collected for every particle on every time step. The particles are binned by energy and location with a weighting factor accounting for the number of electrons each pseudoparticle represents. The particle trajectories are integrated for ~ 100 rf cycles. At the end of each iteration, the EED at each spatial location is obtained by normalizing the statistics

$$\sum_i F_i(\bar{r}) = \sum_i f_i(\bar{r})\varepsilon_i^{\frac{1}{2}}\Delta\varepsilon_i = 1, \tag{3.9}$$

where $F_i(\bar{r})$ is the sum of the pseudoparticles' weightings at $\bar{r}$ for energy bin i having energy ε_i, $f_i(\bar{r})$ (eV$^{-3/2}$) is the EED at $\bar{r}$, and $\Delta\varepsilon_i$ is the bin width. Electron impact rate coefficients for process j at $\bar{r}$ are determined by

$$k_j(\bar{r}) = \sum_j f_j(\bar{r})\varepsilon_j^{\frac{1}{2}}\left(\frac{2\varepsilon_j}{m_e}\right)^{\frac{1}{2}}\sigma_j\Delta\varepsilon_i, \tag{3.10}$$

where σ_j is the energy dependent cross section for process j. This can be used to generate source functions for these impact processes

$$S_j^l(\bar{r}) = kj(\bar{r})n_e^{l-1}(\bar{r}), \tag{3.11}$$

where $n_e^{l-1}(\bar{r})$ is the electron density obtained on the previous iteration. These source functions may be back averaged to accelerate convergence.

3.4 The Fluid-Chemical Kinetics Model

The EETM calculates electron kinetic properties such as electron energy distribution function, electron temperature, and electron impact rate coefficients. Results of the EETM are transferred to the FKM to integrate the fluid continuity, momentum and energy equations. These provide the species densities, fluxes and temperatures, as well as the Poisson;s equation solution for the electrostatic potential.

The continuity equation that describes the density evolution rate for any species is

$$\frac{\partial N_i}{\partial t} = -\nabla \cdot \Gamma_i + S_i \tag{3.12}$$

where N_i, Γ_i, and S_i are the species density, flux, and source for species *i*. Electron (and heavy paricle) densities are determined using the drift diffusion formulation,

$$\Gamma_i = \mu_i q_i N_i \overline{E}_s - D_i \nabla N_i \tag{3.13}$$

where μ_i is the mobility of species *i*, D_i is the diffusion coefficient, q_i is the species charge in units of elementary charge, and E_s is the electrostatic field. Heavy ion and neutral fluxes can be determined by using the previous drift diffusion method or by using the heavy body momentum equation,

$$\frac{\partial \Gamma_i}{\partial t} = -\frac{1}{m_i}\nabla\left(N_i k T_i\right) - \nabla\cdot\left(N_i\ \bar{v}_i \bar{v}_i\right) + \frac{q_i}{m_i} N_i \bar{E} - \sum_j \frac{m_j}{m_i + m_j} N_i N_j \left(\bar{v}_i - \bar{v}_j\right) \nu_{ij} \tag{3.14}$$

where T_i is the species temperature, $\bar{v}_i$ is the species velocity given by Γ_i / N_i, and ν_{ij} is the collision frequency between species *i* and species *j*.

The gas and ion temperatures are determined from the energy equation for each species,

$$\frac{\partial N_i c_v T_i}{\partial t} = \nabla\cdot\kappa_i \nabla T_i - P_i \nabla\cdot\vec{v}_i - \nabla\cdot(\vec{\varphi}_i \varepsilon_i) + \frac{N_i q_i^2}{m_i \nu_i} E_s^2 + \frac{N_i q_i^2 \nu_i}{m_i(\nu_i^2 + \omega^2)} E^2 + \sum_j 3\frac{m_{ij}}{m_i + m_j} N_i N_j R_{ij} k (T_j - T_i) \tag{3.15}$$

where N_i is the density of species i, c_v is specific heat, T_i is the species temperature, κ_i is the thermal conductivity of species i, P_i is the partial pressure of species i, $\vec{v}_i$ is the species velocity, $\vec{\varphi}_i$ is the flux of species i, ε_i is the internal energy of species i, E_s is the electrostatic field, E is the rf field, m_i is the mass of species i, m_{ij} is the reduced mass, ν_i is the momentum transfer collision frequency for species i, and R_{ij} is the collision frequency for the collision process between species i and j.

These fields determine the drift flux terms used in the continuity equation. There are two alternative ways for the FKM to calculate the electrostatic fields. The first option is to directly solve Poisson's equation in a semi-implicit manner. The time evolving electrostatic potential is related to the net charge density as

$$\nabla.\varepsilon\nabla\Phi = -\rho \tag{3.16}$$

where ε is the permittivity, Φ is the electrostatic potential, and ρ is the net charge density. The charge density is numerically estimated using a first-order Taylor series expansion:

$$\rho^{t+\Delta t} = \rho^{t} + \Delta t.\left.\frac{\partial\rho}{\partial t}\right|^{t+\Delta t}, \tag{3.17}$$

where ρ^t is the charge density at time t and $\rho^{t+\Delta t}$ is the charge density at time t. The evolution rate of the charge density $\frac{\partial\rho}{\partial t}$ is determined by the gradient of the total current density j :

$$\frac{\partial\rho}{\partial t} = -\nabla.j + S, \tag{3.18}$$

where S is the source function of charges (including collisions, photoionization, secondary electron emission, etc.). In the plasma region, $j = \sum_i q_i(-D_i\nabla n_i + q_i n_i \mu_i(-\nabla\Phi))$; In materials, $j = \sigma(-\nabla\Phi)$ where σ is the material conductivity.

The second option is to compute electrostatic fields using an ambipolar approximation over the entire plasma region. Under such an assumption, the electron density is equal to the total ion charge density at all locations. At steady state, the flux conservation requires that

$$-\nabla.\Gamma_e + S_e = \sum_i q_i(-\nabla.\Gamma_i + S_i) \tag{3.19}$$

or

$$\nabla.(\mu_e n_e \nabla\Phi + D_e \nabla n_e) + S_e = \sum_i q_i(\nabla.(-\mu_i n_i \nabla\Phi + D_i \nabla n_i) + S_i) \tag{3.20}$$

when using drift-diffusion equations for both electrons and ions. S_e and S_i represent electron and ion source functions, respectively. By solving for the potential in the above form, the time step is limited only by the Courant limit.

3.5 External Modules

The plasma parameters obtained from the HPEM can be used in modules external to the three described above. In this dissertation, two such modules shall be discussed: The Monte Carlo Radiation Transport Module (MCRTM), and the Surface Kinetics Module (SKM). The MCRTM inputs the gas densities, temperatures, pressures, collision frequencies, and rate coefficients for all the gas phase reactions (including radiative reactions), and modifies the rate coefficient for the radiative reactions. The SKM reads in fluxes to the surfaces of interest, and returns sticking coefficients and modified gas fluxes from the surface, afer the surface reactions are computed. Both these modules shall be described in detail in the upcoming chapters.

3.6 Figures

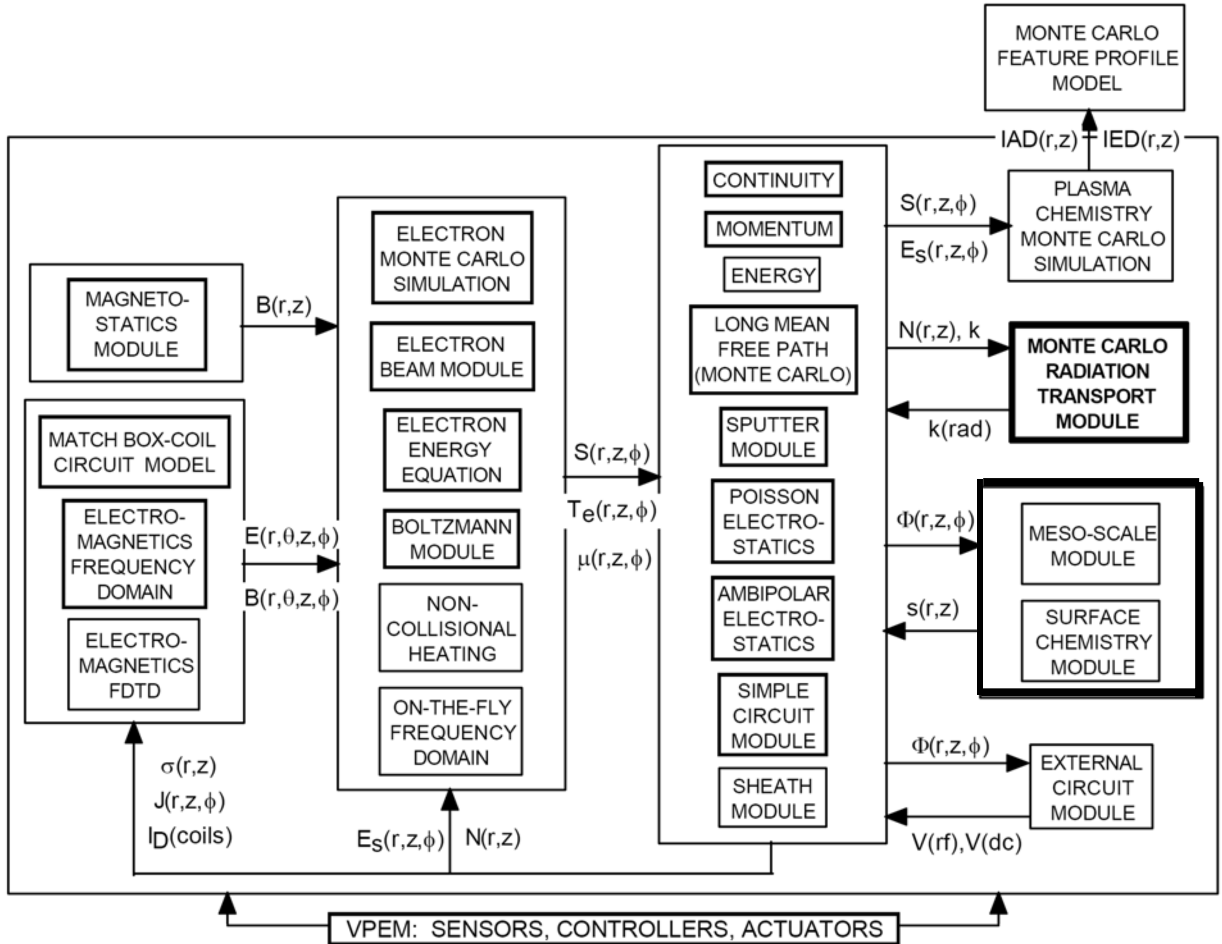

Figure 3.1. Schematic of the modular Hybrid Plasma Equipment Model (HPEM). The highlighted boxes refer to the modules that are of primary importance in this dissertation.

3.7 References

1. P. L. G. Ventzek, R. J. Hoekstra, and M. J. Kushner, J. Vac. Sci. Technol. B **12**, 416 (1993).

2. P. L. G. Ventzek, M. Grapperhaus, and M. J. Kushner, J. Vac. Sci. Technol. B **16**, 3118 (1994).

3. W. Z. Collison and M. J. Kushner, Appl. Phys. Lett. **68**, 903 (1996).

4. M. J. Kushner, W. Z. Collison, M. J. Grapperhaus, J. P. Holland, and M. S. Barnes, J. Appl. Phys. **80**, 1337 (1996).

5. M. J. Grapperhaus and M. J. Kushner, J. Appl. Phys. **81**, 569 (1997).

6. S. Rauf and M. J. Kushner, J. Appl. Phys. **81**, 5966 (1997).

4. MONTE CARLO RADIATION TRANSPORT MODEL

4.1 Description of Model

The Monte Carlo Radiation Transport Model (MCRTM) tracks quanta of energy emitted by plasma excited species as the photon is absorbed and reemitted while traversing the plasma. As the probability for absorption and re-emission depends on local densities of the absorbing and emitting species, the densities of quenching and lineshape perturbing species, and the gas temperature, the MCRTM was interfaced to the HPEM, which provides these quantities. In turn, the MCRTM provides the effective lifetime of emitting excited states for use in the plasma kinetics routines of the HPEM.

The MCRTM directly interfaces with the FKM on each iteration through the HPEM. The parameters provided by the FKM to the MCRTM are species densities, gas temperatures, and rate constants, from which the frequencies for perturbing and quenching collisions affecting the species participating in radiative transfer reactions are calculated. The MCRTM produces radiation trapping factors which are used to modify the lifetime of radiating species during the next execution of the FKM. The algorithms used in the MCRTM are similar to those used by Sommerer.[1] (Fig. 4.1) Pseudoparticles representing photons are tracked from their site of emission through multiple absorptions and re-emissions until their escape from the plasma or until the quanta of energy is quenched. Although reflection from surfaces can be accounted for, we assumed that all surfaces are absorbing or transmitting and so any photon which strikes a surface is lost from the plasma.

Pseudoparticles are emitted from sites randomly distributed within a numerical

mesh cell in proportion to the density of radiators in that cell (obtained from the FKM). As the densities of radiators may vary by orders of magnitude over the plasma region, the number of pseudoparticles released from each cell i is rescaled to ensure that a statistically relevant number of pseudoparticles is emitted from every cell.

$$n_i = n_{min} + (n_{max} - n_{min}) \frac{\log N_i^* - \log N_{min}^*}{\log N_{max}^* - \log N_{min}^*} \tag{4.1}$$

where n_i is the number of pseudoparticles emitted from cell i, and n_{min} and n_{max} are preselected minimum and maximum number of pseudoparticles permitted to be emitted and N_i^* is the density of the radiating species in cell i. N_{min}^* and N_{max}^* are the minimum and maximum densities of N* in the plasma. These values are dynamically determined during execution of the model. A weighting w_i is assigned to each pseudoparticle for the purposes of collecting statistics. For a pseudoparticle emitted from cell i,

$$w_i = \prod_m w_{m,i} \tag{4.2}$$

where w_m is a series of subweightings. The first such subweighting is

$$w_{1,i} = \frac{N_i \Delta V_i}{n_i} \tag{4.3}$$

where ΔV_i is the volume of cell i.

The frequency of the photon is then selected from the lineshape function $g(\nu)$, the probability of a photon being emitted at a frequency.[2] The likelihood of the photon being emitted near line center can be hundreds to thousands of times higher than being emitted in the far wings of the lineshape. The majority of photons escaping the plasma usually originate from the wings of the lineshape, where absorption probabilities are smaller. Selecting pseudoparticles with probabilities directly proportional to $g(\nu)$ would, in the absence of using a very large number of pseudoparticles, undersample the wings of the lineshape. Although the assignment of frequency directly proportional to $g(\nu)$ is the least ambiguous method, the need to avoid sampling problems in 2-dimensions and the desire to obtain frequency resolution throughout the mesh motivates one to try another method. To avoid the statistical undersampling in the wings of the lineshape profile, we instead uniformly distribute the pseudoparticles over a preselected range of frequencies about the line center ν_0, and use an additional weighting factor $w_2 = g(\nu)$ to account for the likelihood of emission.

4.2 Lineshape

The lineshape is a Voigt profile, which combines the features of Doppler and Lorentzian broadening and is applicable at the temperatures and pressures of interest to us. This lineshape is given by

$$g(\nu') = \frac{\gamma}{\pi^{3/2}} \int_{-\infty}^{\infty} \frac{e^{-y^2}}{\gamma^2 + (\nu' - y)^2} dy , \quad \gamma = \frac{\nu_H}{4\pi \Delta \nu_D} , \quad \nu' = \frac{\nu - \nu_0}{\Delta \nu_D} \tag{4.4}$$

where ν_H is the homogeneous Lorentzian damping frequency, $\Delta\nu_D$ is the Doppler width, and ν' is the frequency departure from ν_0 in units of Doppler width. For our conditions,

$$\nu_H = A + \sum_j 2\nu_j \tag{4.5}$$

where A is the Einstein coefficient for spontaneous emission and ν_j is the frequency for broadening collisions by the jth species. As ν_j depends on the local densities and temperatures of collision partners and ν' depends on the local gas temperature through $\Delta\nu_D$, $g(\nu')$ is then also a function of position. Rather than recompute $g(\nu')$ at every mesh point, $g(\nu')$ was pre-computed at the beginning of each iteration of the MCRTM and stored as a two-dimensional array with γ and ν' as interpolation parameters. We estimate the range of ν' to construct the lookup tables based on estimates of densities and temperatures from previous cases. Typical ranges are $-5 \leq \nu' \leq 5$. Given the array $g(\gamma, \nu')$, the actual value of the Voigt profile at any spatial point is found by simple interpolation using the local values of γ and ν'. For investigations of systems with multiple isotopes or radiating species, $g(\gamma, \nu')$ is pre-computed as a three-dimensional array with the third index corresponding to a given species.

Given the randomly chosen initial frequency, the polar and azimuthal angles for emission are randomly chosen assuming an isotropic distribution. A running tally of the residence time of the pseudoparticle in the plasma is initialized as $\tau_T = -\frac{w_i}{A}\ln(r)$, where r is a random number distributed on (0,1). The photon transport was then tracked until its

next absorption by stepping through the mesh. As the geometry of the lamp is, in principle, arbitrary, the stepping method is required to account for striking physical objects (e.g., protruding electrodes). Although view factors and a Green's function could, in principle, substitute for the spatial integration, the tradeoffs between computer storage requirements and computing time to derive the Green's function were not favorable.

The null collision method was employed for photon transport. The photon path at frequency ν is advanced a distance $\lambda = \lambda_{min}(\nu)\, ln(r)$, where $\lambda_{min}(\nu)$ is the minimum mean free path for absorption at frequency ν based on densities, temperatures and cross sections throughout the mesh

$$\lambda_{min}(\nu) = \frac{1}{max\left(\sum_j N_j \sigma_j(\nu)\right)}, \qquad \sigma_j(\nu) = \frac{A_j c^2 g(\nu)}{8\pi\nu^2} \tag{4.6}$$

where the max function samples all locations in the mesh and the sum is over absorbing species having density N_j, absorption cross section $\sigma_j(\nu)$, and Einstein coefficient A_j. After advancing the trajectory a distance λ to location $\vec{r}$, the probability of a real absorption is determined by comparing

$$r < \frac{\sum_j N_j(\vec{r})\, \sigma_j(\vec{r},\nu)}{max\left(\sum_j N_j \sigma_j(\nu)\right)} \tag{4.7}$$

where r is a random number distributed (0,1). If the inequality is satisfied, the absorption occurs. If not, another test absorption length is chosen and the photon is advanced without change in direction. The identity of the absorbing species k is determined from

$$\delta_{k-1} < r < \delta_k, \qquad \delta_k = \frac{\sum_{j=1}^{k} N_j(\vec{r})\,\sigma_j(\vec{r},\nu)}{\sum_{j=1}^{n} N_j(\vec{r})\,\sigma_j(\vec{r},\nu)} \tag{4.8}$$

where n is the total number of absorbing species. If the absorbing species is non-emitting, the pseudoparticle is removed from the simulation. Otherwise the photon is re-emitted if not quenched.

At sufficiently large pressures or plasma densities, or statistically long lifetimes, quanta of energy may be quenched by collisions prior to re-emission. The likelihood of this occurring is determined by

$$r > \frac{A'}{A' + \sum_j \nu_j(\vec{r})}, \qquad A' = A\, ln(r) \tag{4.9}$$

where ν_j is the frequency of the jth quenching collision. If the inequality holds, the excited state was deemed to have been quenched prior to emission, and the quanta of

energy is removed from the simulation. For non-quenched quanta, τ_T is incremented as

$\tau_T \rightarrow \tau_T - \frac{w_{ij}}{A} ln(r)$, and the photon is re-emitted at a frequency determined by PFR.

The trapping factor as viewed from outside the lamp is defined as

$$K = \frac{\sum_m \tau_{T_m}}{\sum_m w_m} A, \tag{4.10}$$

where the sum is over all escaping photons. For purposes of extension of the lifetime of the excited state, the sum is over all emitted photons. The effective radiative lifetime of the radiating state is then A / K for the next iteration for the HPEM.

4.3 Frequency Redistribution

The Holstein-Biberman model [3] assumes complete frequency redistribution, that is the frequency and velocity of the emitted photon is uncorrelated to that of the absorbed photon. As such, the frequency for pressure broadening collisions should be commensurate or larger than the rate of radiative relaxation. PFR assumes that there is a correlation between the absorbed and emitted wavelengths. In the limit of there being no momentum changing collisions, the absorption and emission frequencies should be the same, or at best differ by the natural linewidth. We addressed PFR by two methods. In the first method, photons absorbed at frequency ν, are randomly reemitted in the frequency range $\nu \pm \Delta\nu$. The value of $\Delta \nu$ was found by determining the trapping factor of the 254 nm transition of Hg in a cylinder of radius R_0 with a uniform density of Hg

and Ar , and comparing to a more exhaustive formalism for PFR.[4] The calibration in this manner yielded $\Delta\nu = \alpha\Delta\nu_D$, $1.75 < \alpha < 2.0$. A comparison of the trapping factors so derived and those obtained by Lister [4] are shown in Table 4.1. In general, the agreement is good.

We also used a more exact formalism for PFR, which is similar to the Jefferies-White approximation.[5, 6] The core of the lineshape is determined by Doppler broadening, while the wings are determined by Lorentzian broadening. Pure Doppler broadening corresponds to a complete coherence in the rest frame of the atom, but due to the direction of re-emission being random, the absorbed and re-emitted frequencies are uncorrelated in the laboratory rest frame. Thus, pure Doppler broadening corresponds to CFR. We modeled the Doppler core using CFR, and the wings using PFR. To model PFR in the wings for absorption at ν, we redistribute the emission frequency randomly within one Doppler width of ν. The approximate core cut-off frequency is precalculated based on the solution of the equation

$$exp\left(-x_\nu^{\,2}\right) = \frac{\gamma}{x_\nu^{\,2}\sqrt{\pi}} \tag{4.11}$$

where x_ν is the departure from line center in units of $\Delta\nu_D$.

4.4 Hyperfine Splitting and Isotopes

A lamp may have many radiating species, each having its own spectral distributions for absorption and emission, such as the 254 and 185 nm resonance

transitions. In the event these distributions overlap, they may interfere or contribute to radiation transport from another species. This is particularly the case for isotopes whose line center frequencies are closely spaced. In our model we treated isotopes as separate species to account for, for example, energy exchanging collisions. For example, when a photon is deemed to have been absorbed, we checked to determine which of the isotopes the particle is absorbed by using Eq. 4.8.

Hyperfine splitting (hfs) of an isotope results in subclasses of the species having a different ν_0, collision frequency and concentration which leads to different lineshapes for each hfs component. In the same manner as isotopes, we consider each hyperfine component as a separate radiating species. Foreign gas collisions are known to redistribute the excitation on hfs components of odd isotopes.[7] As such, if the quanta was absorbed by an even isotope, it was re-emitted by the same isotope. If the quanta was absorbed by an odd isotope, the likelihood of a collision redistributing the excitation among hfs components was computed using crosssections from Sommerer.[1] Based on choice of a random number, if the collision is deemed to have occurred, the excitation is redistributed.

The reaction mechanism for Ar/Hg plasmas is summarized in Appendix A. The electron impact cross-sections for Hg were taken from Rockwood, Kenty and Vriens.[8-10] The heavy-body cross-sections (excitation transfer, quenching) were taken from Sommerer.[1] The values for the cross-section for resonance broadening between Hg species is 3×10^{-14} cm^2 and that for Ar-Hg broadening is 7×10^{-15} cm^2.

4.5 Tables

Table 4.1. Comparison of trapping factors obtained by MCRTM and Lister[a)]

R_0 (cm)	[Hg] (cm^{-3})	[Ar] (cm^{-3})	T_{ave} (K)	k_{Lister}	k_{MCRTM}
0.80	1.4×10^{14}	1.6×10^{17}	373	14.2	14.3
1.27	1.4×10^{14}	1.3×10^{17}	373	22.3	23.1
1.91	1.9×10^{14}	8.0×10^{16}	313	47.8	48.8
2.50	1.9×10^{14}	9.6×10^{15}	313	100.4	104.3

a) G.G. Lister, Private Communication

4.6 Figures

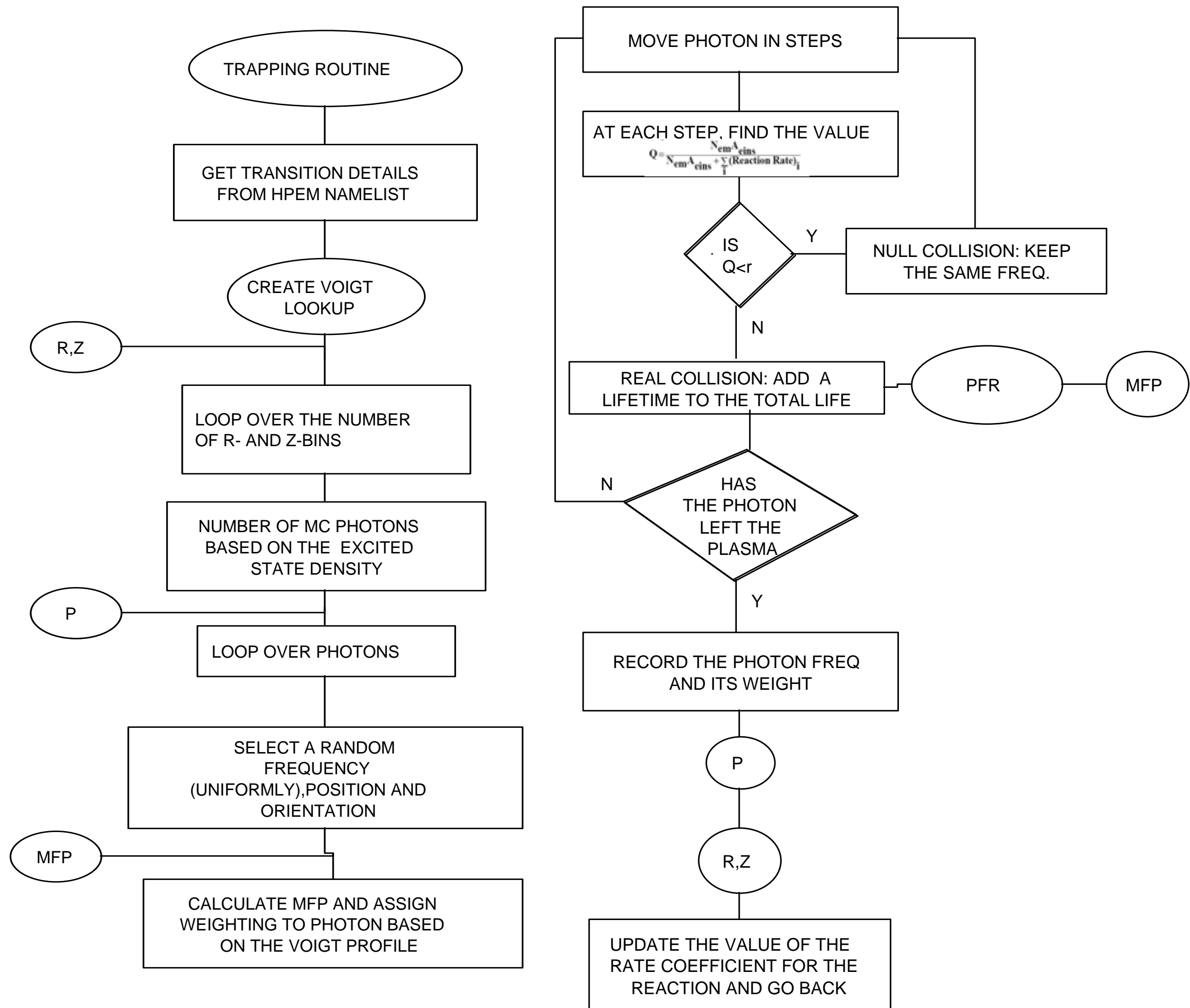

Figure 4.1. Flowchart of the Monte Carlo Radiation Transport Model

4.7 References

1. T. J. Sommerer, J. Appl. Phys. **74**, 1579 (1993).
2. L. W. Avery, L. L. House, and A. Skumanich, **9**, 519 (1969).
3. T. Holstein, Phys. Rev. **72**, 1212 (1947).
4. G. G. Lister, Private Communication.
5. A. F. Molisch and B. P. Oehry, Radiation Trapping in Atomic Vapours (Clarendon Press, Oxford, 1998).
6. J. T. Jefferies and O. White, Ap. J. **132**, 767 (1960).
7. K. L. Menningen and J. E. Lawler, J. Appl. Phys. **88**, 3190 (2000).
8. S. D. Rockwood, Phys. Rev. A **8**, 2348 (1973).
9. C. Kenty, J. Appl. Phys. **21**, 1309 (1950).
10. L. Vriens and A. H. M. Smeets, Phys. Rev. A **22**, 940 (1980).

5. RADIATION TRANSPORT IN ELECTRODELESS LAMPS

5.1 Introduction

An overview of radiation transport, and the reasons for using numerical methods to address this phenomena, have been introduced in Chapter 2. Descriptions of the computational models used for our study have been presented in Chapters 3 and 4. In this chapter, we shall apply these models to realistically simulate commercially available lamps, and investigate the effects of varying plasma conditions on radiation transport. The motivation for this study is to provide lamp designers with a more complete understanding of physical processes, that may not have been accounted for in a self-consistent manner to date. The chapter shall discuss both first-order as well as second-order effects of radiation transport in Hg/Ar lamps. The first-order effects arise directly from the absorption/emission processes, causing an extended lifetime of the radiative states. The second-order effects arise because these extended lifetimes cause the radiative states to participate in more gas-phase reactions, like multi-step ionization and superelastic relaxation.

5.2 Base Case Geometry and Plasma Parameters

The geometry for the base case is shown in Fig. 5.1. This lamp is similar in shape to the Philips QL lamp.[1] rf coils are wrapped around a central ferrite core. The plasma volume has a reentrant cavity surrounding the coil. The base case operating conditions are an Ar fill pressure of 500 mTorr, cold spot temperature of 310 K (corresponding to a Hg vapor pressure of ≈5 mTorr), an rf frequency of 5 MHz, and a power deposition of 55

W. The skin depth for these conditions is ≈30 cm. The electric field is a maximum near the coils, primarily for geometrical reasons as opposed to a short absorption length. As a result, the largest specific power deposition is near the reentrant coil.

The electron temperature T_e and density n_e are also shown in Fig. 5.1. T_e has a maximum value of ≈2 eV near the coil. For these conditions, the electron mean free path is $\approx 10^{-2}$ cm, much less than the skin depth, and the electron collision frequency is $\approx 1 \times 10^9$ s^{-1}, much larger than the rf frequency. Power deposition is therefore dominantly collisional. The electron density peaks at $\approx 2 \times 10^{12}$ cm^{-3} in an annulus around the antenna. The gas mixture is not attaching, and recombination in the bulk plasma is negligible. As a result, the dominant charged particle loss is by diffusion. The lower ionization threshold of Hg and multistep ionization from Hg(6P) produces far more rapid ionization than Ar. Any excited states or ions of Ar are rapidly quenched by Penning ionization ($\tau \approx 25$ μs) and charge exchange ($\tau \approx 400$ μs).

Ground and excited state densities of Hg are shown in Fig. 5.2. The Hg ground state density [$Hg(6^1S_0)$] is significantly depleted in the central region of the plasma due to cataphoresis. The ambipolar radial ion flux (see Fig. 5.2d) to the walls at the midheight of the antenna is $\approx 10^{17}$ cm^2s^{-1} and the momentum transfer cross section to Hg (6^1S_0) is $\approx 10^{-15}$ cm^2, producing a rate of momentum transfer of $\approx 10^2$ s^{-1}, which is rapid compared to the rate of thermal diffusion. The $Hg(6^1S_0)$ is therefore depleted in the central part of the lamp, an effect that is exacerbated by a gas temperature rise with respect to the walls of ≈40 K. Ions recombining on the surfaces provide a source of ground state neutrals at the wall. The end result is that the $Hg(6^1S_0)$ density is maximum near the walls.

The production of $Hg(6^3P_1)$, upper state of the 254 nm transition, is dominated by electron impact from the ground state. The quenching of Hg (6^3P_1) is dominated by superelastic electron collisions ($\tau \approx 1$ ms), and radiative relaxation, both of which have rates which are large compared to transport. The density of $Hg(6^3P_1)$ therefore peaks where the excitation rates are largest which in this case is near the walls at the height of the antenna where the electron temperature and $Hg(6^1S_0)$ are largest. The $Hg(6^1P_1)$ density (upper state of the 185 nm transition) also peaks near the antenna. The untrapped (1.3 ns) radiative lifetime of $Hg(6^1P_1)$, state is small compared to the untrapped lifetime of the $Hg(6^3P_1)$ (125 ns). As a result, spreading by diffusion of the $Hg(6^1P_1)$ density from its peak has a smaller extent than does the $Hg(6^3P_1)$ density, but otherwise the spatial distributions of the two emitting states have the same functional dependencies. As a result, we shall only be showing the Hg (6^3P_1) profile as an indication of emitter densities.

5.3 Effects of Plasma Conditions on Radiation Transport

Radiation trapping factors were investigated for the 185 nm and the 254 nm transitions while varying the cold spot temperature T_c, which controls the vapor pressure of Hg. As the lamps are sealed, an increase in T_c increases the Hg density while the Ar density remains the same. As such, with increasing T_c the rate of collisional broadening remains nearly constant with a small increase due to the increase in thermal speed. When keeping the power constant, the density of emitters (excited states) is approximately constant. The end result is that the trapping factors increase with T_c, as shown in Fig. 5.3. The trapping factors for both the 185 nm and 254 nm transitions change by nearly

the same percentage, and this is to be expected because the spatial profiles of the radiators and absorbers for both the transitions are nearly the same. At the largest Hg densities, the total trapped lifetimes (Kτ) of the 185 and 254 nm transitions are approximately the same (2.9 μs).

The trapping factor for the 185 nm line is about 100 times larger than the trapping factor for the 254 nm line, which suggests an inverse scaling of the trapping factor with vacuum radiative lifetime. The Holstein theory for a cylindrical discharge states that the trapping factor for a Doppler broadened line scales as

$$K = \frac{\alpha(\pi \ln \alpha)^{1/2}}{1.6}, \qquad \alpha = \frac{R\lambda_0^3 N g_2 A}{8\pi^{3/2} g_1 V_t}, \tag{5.1}$$

where $V_t = \left(\frac{2kT}{M}\right)^{1/2}$, λ_0 is the wavelength at line center, g_1 and g_2 are the statistical degeneracies for the upper and lower energy levels, and R is the radius of the cylindrical discharge.[2] So for similar absorber densities, trapping factors should scale almost inversely with vacuum radiative lifetime, which we observe here. The nonlinearities in the scaling of K/[Hg] likely result from the complex non-cylindrical geometry of the lamp and the fact that the densities of absorbers and emitters are not uniform.

The spectra for the 254 and 185 nm transitions, averaged over all photons escaping the lamp, are shown for cold spot temperatures of 293 K and 323 K (Hg densities of ≈3.5 × 10^{13} and ≈3.5 × 10^{14} cm^{-3} respectively) in Fig. 5.4. The dip in the center of the lineshape is due to the more frequent absorption of photons which, with

PFR, may be re-emitted in the wings of the lineshape where the mean free path for absorption is longer and so the likelihood for escape from plasma is greater.

The choice of rf frequency for exciting the plasma is an important design consideration with respect to the efficiency of power transfer. Radiation transport ultimately depends on the spatial distribution of radiators and absorbers, which is determined by the spatial distribution of power deposition. To investigate whether the rf frequency should be a consideration with respect to radiation transport, the frequency was varied while keeping the other parameters constant. The resulting trapping factors for the 254 nm and 185 nm lines are shown in Fig. 5.5. The trapping factors have only small variations with the rf frequency, mostly within the limits of statistical error of the method. At our operating conditions of 100s of mTorr, the plasma is collisional, and the electron-neutral momentum transfer frequency ν_m is greater than the plasma frequency ω_{pe} near the boundary. In this case, the skin depth is given by [3]

$$\delta_c = \left(\frac{2}{\omega \mu_0 \sigma_{dc}} \right)^{1/2}, \qquad \sigma_{dc} = \frac{e^2 n_e}{m \nu_m} \tag{5.2}$$

For our lamp, the maximum electron density for the base case operating conditions is 2×10^{12} cm^{-3}. The minimum collision frequency is 1.5×10^{7} s^{-1}, which gives a minimum possible skin depth of approximately 30 cm, which is much larger than the size of the lamp. Frequencies in the GHz regime would be required to perturb the spatial distribution of radiators. As a result, radiation transport is little affected by the rf frequency.

5.4 Lamp Geometry and Radiation Transport

Although there are many constraints and tradeoffs on lamp design, radiation transport is one important consideration. In this regard, we contrasted a geometry similar to the Everlight lamp geometry [4] and with that of the QL lamp. The Everlight lamp has its coils in an external solenoidal configuration. For purposes of this study, we chose the radius and height of the lamps to be the same. Without a re-entrant void for the central post, the volume of the Everlight lamp is larger. Plasma parameters (power, electron density, [Hg (6^1S_0)] and [Hg (6^3P_1)]) for the Everlight lamp are shown in Fig. 5.6 for the base case conditions. Power deposition peaks at (2.6 W/cm^3, smaller compared to the QL lamp because the same power (55 W) is deposited into a larger overall volume. Since the peak electric fields are at the outer radii for the Everlight lamp and inner radii for the QL lamp, the incremental volumes for peak power deposition are also larger. The electron density has a similar peak value as the QL lamp though the maximum is displaced to a larger radius. As such, the ion flux producing cataphoresis which transports Hg (6^1S_0) has inward and outward components. The spatial distribution of Hg (6^3P_1), though still highly peaked towards the coils, is more uniformly distributed through the volume of the lamp.

Trapping factors for the 254 and 185 nm transitions for the QL and Everlight geometries while varying the Ar fill pressure and the cold spot temperature are shown in Table 5.1. All other parameters were kept at their base case values. The general trends are that trapping factors decrease with increasing Ar fill pressure and increase with increasing Hg partial pressure. The decrease in trapping with fill pressure results from the increasing Ar collision frequency, which redistributes quanta to the wings of the

lineshape, thereby increasing the likelihood for escape. An increase in trapping factor with increasing [Hg] is due to the larger absorber density. The increase in trapping factor did not directly scale with the increase in Hg vapor density. The trapping factors for the QL geometry are systematically smaller than for the Everlight geometry by 5-15%. We attribute these scalings to the non-uniform distributions of radiators and absorbers.

For example, the Hg ground and excited state densities for the two lamps with an Ar fill pressure of 100 mTorr, and Hg partial pressure of 5 mTorr (T_c=310 K) are shown in Fig. 5.7; and for a Hg pressure of 20 mTorr (T_c=330 K) in Fig 5.8. The spatial distributions of the Hg ground state are significantly different between the 5 and 20 mTorr cases. These differences are due in part to the more collisional conditions for electrons with the higher Hg pressure, producing shorter mean free paths for energy dissipation. As a result, excitation is confined closer to the high electric field regions near the coils. The difference in ground state density is also in part due to momentum transfer from ions. Owing to the increase in the Hg ground state density, there is more efficient momentum transfer of Hg^+ with the more numerous and same mass ground state Hg compared to the lighter Ar. The rate of symmetric charge exchange also increases, resulting in charge exchange becoming the dominant momentum transfer process which shifts the peak of the Hg ion density towards the walls, as shown in Fig. 5.8. This relative shift in ionization peak is more apparent in the Everlight lamp due to the longer distance between the center of the column and the walls. Due to the shift in peak in ionization, the cataphoresis now occurs at a different location in the lamp.

The peak densities of Hg (6^3P_1) are shifted towards the walls at higher Hg densities in both lamps. The end result is that in the Everlight lamp geometry, regardless

of where the photons are emitted in the bulk, they experience a Hg absorber density of around 6 (10^{14} cm^{-3} between the sites of emission and the walls. In contrast, most of the photons emitted in the interior of the QL lamp traverse a depleted region of Hg in the center of the lamp, and only traverse high densities of absorbers near the walls of the lamp. As a result, trapping factors for the Everlight lamp are moderately higher than those for the QL lamp.

Trapping factors as a function of power for the QL lamp are shown in Fig. 5.9 for an Ar fill pressure of 500 mTorr and Hg pressure of 5 mTorr. We found that the trapping factors generally decrease with increasing power deposition. With increasing power the depletion of Hg (6^1S_0) in the center of the lamp by both thermal and cataphoretic processes increases, producing larger ground state densities near the walls. As a result the excited state densities are produced successively closer to the walls with increasing power. Had this been a plane parallel geometry, the proximity of the radiators to the walls would likely have been offset by the larger column density of Hg (6^1S_0) near the walls resulting in little, if any change in trapping factor. In these more complex geometries, the closer proximity of radiators to the walls dominates the increased column density, producing a smaller trapping factor. Increased power also produces more electron collisional quenching. Quanta which were originally emitted deep in the interior of the lamp are less likely to escape the plasma. It is these photons which most heavily contribute to the trapping factor, and so their loss reduces the average residence time and decreases the trapping factor.

To decouple cataphoresis and electron collisional quenching from other parametric variations, investigations were performed at a low ICP powers. For example,

trapping factors as a function of Ar fill pressure are shown in Fig. 5.10 for a power of 10 W for which cataphoresis is not terribly important. As such the densities of excited states of Hg peak in the center of the lamp, and most quanta are emitted from that volume. The trapping factors are found to be approximately constant over the pressure range studied (50-1500 mTorr) and within the statistical error of the method, a consequence of natural and Doppler broadening dominating. From these and other studies, we concluded that variations of trapping factors with power and pressure over the design space can be largely attributed to redistribution of radiators resulting from cataphoresis and secondarily due to electron quenching in the bulk of the plasma.

5.5 Isotopic Effects of Mercury

Previous studies have proposed that trapping factors can be manipulated by changing the isotopic abundance of the Hg atoms.[5] The ability to manipulate trapping factors with addition of, for example, Hg 196 results from its center frequency being sufficiently far away from the other isotopes that a photon that is emitted by that isotope has a high likelihood of escaping from the lamp. Ideally, quanta of energy which are collisionally mixed between the isotopes and which are preferentially channeled to the Hg 196 isotope are rapidly radiated away. Some success in manipulating radiation trapping factors with isotopic abundances has been achieved for conventional high pressure linear lamps.

In this regard, exit spectra for the complete isotopic structure of Hg with hfs are shown in Fig. 5.11 for an Ar fill pressure of 500 mTorr, T_c=310 K (Hg = 5 mTorr) and Ar fill pressure 1.5 Torr, T_c=340 K (Hg=40 mTorr). Other operating parameters were kept

at their base case values. The spectrum at the lower fill pressure and cold spot shows 10 peaks due to self-trapping. The Hg-196 isotope is not visible in the spectrum for these conditions due to its low abundance. The isotopes of the Hg-199a, Hg-201a and Hg-204 have small line center separations compared to their separations from other isotopes. As a result, their combined lineshape appears as the lineshape for a single isotope. The Hg-198 and Hg-201b isotopes, and the Hg-199b and Hg-201c isotopes also behave similarly. The end result is the appearance of five "isotopes". At low Ar and Hg pressures typical of electrodeless lamps, there is insufficient broadening and collisional mixing for there to be significant exchange of quanta between isotopes and so we obtain non-overlapping spectra with line self-reversal. As such, special isotopic mixtures to manipulate trapping factors are not likely to be important at the lower pressures of electrodeless lamps. At the higher Ar and Hg densities typical of conventional linear lamps which have greater collisional broadening and mixing, the lineshapes overlap and there is exchange of quanta between isotopes, as shown in Fig. 11b. We performed studies on the effect of artificially increasing the Hg-196 concentration on trapping factors. We found that for Hg-196 concentrations from 0.15% (naturally occurring) to 3.5%, there was no significant variation in trapping factors of any of the Hg isotopes. This is again due to our low pressure operating conditions for which there are not enough collisional processes to randomize the exit channels of photons.

5.6 Radiation Trapping and Electron Energy Distributions

Due to nonequilibrium electron transport, the electron energy distributions (EED) in the lamps discussed above are non-Maxwellian. Electron-electron collisions

redistribute the electron energy, and strongly influence the high energy tail of the EED. The effect of de-Maxwellization on a fluorescent lamp plasma has been studied computationally by Hartgers et al.[6] They found that the de-Maxwellization reduced the number of Ar ions by as much as an order of magnitude, and affected other processes like Penning ionization production of Hg ions. Wani [7,8] has shown that the superelastic collisions with Hg excited atoms increase more than the other inelastic collisions with increase in Hg density.

The effect of radiation trapping on the EEDs has not been addressed directly in these studies. Due to radiation trapping, the longer effective lifetime of the radiative states leads to second order effects, which may include changes in the ionization balance (due to multistep ionization from the excited state) and electron temperature. In this letter, we study these secondary effects on radiation trapping. To address this, we ran the Electron Monte Carlo Simulation Routine (EMCS) in conjunction with the MCRTM, to obtain spatial information about the statistics of the electron distributions at various points in the lamp.

5.6.1 Electron Energy Distributions for the Base Case

The electron energy distribution statistics are collected using the method outlined by Vasenkov et al.[9] In Fig. 5.12, we show the three locations where the distributions shall be compared. The three points are chosen in the region of maximum emitter density (A), in the center of the cylindrical column, where the ground state absorbers are lowest in number (B), and at the opposite wall, where the electron density is lowest. (C)

The untrapped electron energy distributions are shown as dotted lines in Fig. 5.13. These refer to the simulations performed with the Hg 6^3P_1 and 6^1P_1 states emitting at the vacuum radiative lifetimes (125 ns and 1.33 ns respectively). The EEDs near the antenna have the longest tail because of high power deposition in the region. The electrons then accelerate into the bulk plasma, where they degrade in energy due to collisions, and few electrons can overcome the barrier of the bulk plasma potential. These electrons exchange kinetic for potential energy, leading to very short-tailed distributions on the walls opposite the antenna (point C). The other mechanism for electrons at the opposite wall is for high energy electrons to directly reach the opposite wall without falling into the potential well. However, due to the high [Hg] density, these high energy electrons are generally consumed in direct impact ionization of the ground state of Hg. As a result, we see no high energy electrons at the opposite wall. The base case shows one inflection at 5 eV, and the tail is determined by power balance and the direct impact ionization of Hg (10.4 eV).

5.6.2 Effects of Radiation Trapping

The effect of radiation trapping is to extend the lifetime of the radiative states. At the base case properties, this extension is a factor of ~7 (for the Hg 6^3P_1 transition) and ~ 500 (for the Hg 6^1P_1 transition). This extended lifetime manifests itself as an increase in density of these states. Due to this extended lifetime, excited states can participate in more reactions, the main ones being multi-step ionization and superelastic relaxation to the ground state.

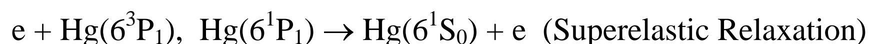

$e + Hg(6^3P_1),\ Hg(6^1P_1) \rightarrow Hg(6^1S_0) + e$ (Superelastic Relaxation)

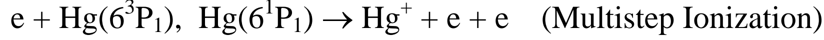
$e + Hg(6^3P_1),\ Hg(6^1P_1) \rightarrow Hg^+ + e + e$ (Multistep Ionization)

Hg*-Hg ionization occurs at a threshold of ~5 eV. The primary electron loses this energy (depleting the tail of the EED), and a new electron is created with an energy $E_s \propto E_b / (1 + E_p / E_b)^2$, where E_p is the primary electron energy and E_b is a parameter, approximately 15 eV in this case. Due to the secondary electron being created with low energy, there is increase in the bulk of the EED. On the other hand, an increase in excited state lifetime also causes an increase in superelastic collisions. Low energy electrons mainly participate in this process, gaining the energy differential as the Hg excited state relaxes to the ground state. Thus, this leads to an increase in the tail, and lowering of the bulk of the EED. These two processes work to opposite effects on the tail of the EED.

The simulations performed including the effect of trapping are shown by solid lines in Fig. 5.13. The shortening of the EED with an extension in excited state lifetime would lead us to believe that the ionization is the dominant mechanism in the plasma studied here. This is confirmed by Table 5.2, where the $[Hg^+]$ and n_e increase by an order of magnitude with the introduction of radiation trapping. If superelastic relaxation had been the dominant process, then the electron density would not increase, and the tail of the EED would move to higher energies, both of which are not occurring in this case. This ionization is predominantly multistep, because the ground state densities do not change appreciably by the extension of the lifetime.

For the case of a lower partial pressure of Hg (Ar fill 500 mTorr, cold spot 300 K), the EEDs are shown in Fig. 5.14(a). In this case, the untrapped distributions have a much longer tail, because the Hg ionization is reduced. The tail of the distribution at

point A goes to 20 eV from less than 15 eV for the 40 mtorr Hg vapor pressure case. Also, these high energy electrons can escape the plasma potential well without falling into it, and directly reach the opposite wall. Thus, at point C, the high energy tail of the distribution is populated, while the bulk of the distribution is Maxwellian because these electrons are emerging from the column of bulk plasma in the center of the lamp. Due to the pooling of electrons in the bulk of the plasma well, there are numerous collisions and the electrons are thermalized before emerging to the opposite wall. In this case, with trapping included, the effects are negligible. From Table 5.3, we see that the excited state lifetimes are lengthened as in the first case. However, the relative change in [Hg 6^3P_1] with and without trapping is not as high as in the case of a higher vapor pressure. This is because of two factors: firstly, the absolute Hg excited state densities are not high enough to participate in multi-step ionizations. The second factor is that for a higher vapor pressure of Hg, the direct impact ionization of the Hg 6^1S_0 leads to secondary electrons formed in the bulk of the distribution. This electron density increase leads to thermalization, and increased availability of electrons for multistep ionization.

The extremal case of an extremely high partial pressure of Hg (400 mTorr Hg, 1600 mTorr Ar) is shown in Fig 5.14(b). This is unphysical (corresponding to a cold spot of ~385 K), but has been shown here to illustrate the effects of superelastic relaxations. The trapped EEDs in this case have an extended tail compared to the vacuum EEDs, suggesting the possibility of superelastic collisions. From Table 5.4, the electron density does not increase as much as in the cases of lower Hg density. [Hg 6^1S_0] should increase more than in the prior cases too, but since the change [Hg 6^1S_0] due to superelastic

collisions is only a fraction of the base density, it is not a statistically significant indicator of the presence of superelastic collision processes.

5.7 Conclusions

A Monte Carlo resonance radiation transport model has been described which interfaces with a plasma equipment model to evaluate radiation trapping in gas discharges having complex geometries. Electrodeless inductively coupled discharges were investigated under a variety of operating conditions with different isotopic considerations. The scaling laws which provide Holstein factors in simpler geometries are not necessarily applicable in the case where radial cataphoresis generates a nonuniform density profile of absorbers and emitters. At typical operating conditions, the electromagnetic skin depth is much larger than the size of the lamp and so the frequency of rf excitation does not affect radiation transport. Trapping factors decrease with an increase in applied power due in large part to a redistribution of radiators and absorbers. The shape of the plasma vessels affects the radiation transport through cataphoresis. This effect increases at higher temperatures where momentum transfer between Hg ions and Hg neutrals is more efficient.

Also, radiation trapping in Ar/Hg discharges leads to an extension in the lifetime of radiative excited Hg states. Increased multistep ionization leads to a reduction of tail electrons in the EED, while increasing the bulk, while superelastic collisions create the opposite effect. Coupling of the plasma kinetics to the MCRTM led to significant spatial variations in densities and temperatures of photon radiating and absorbing species, and these inhomogeneities manifest themselves in the spatial variation of EEDs. At the low

Hg vapor pressures used in electrodeless lamps, however, this effect is negligible in these lamps. At increase of cold spot, multi-step ionization is the dominant process, until superelastic processes become the dominant mechanism defining the EEDs, and the effect of radiation trapping is to extend the tail of the EED to higher energies.

5.8 Tables

Table 5.1. Trapping factors for QL and Everlight geometries (55 W, 5 MHz)

Lamp Geometry	Hg vapor pressure (mTorr)	Ar fill pressure (mTorr)	Trapping factor	
			254 nm	185 nm
Everlight	5	100	2.52	220
Everlight	5	500	2.10	203
Everlight	20	100	10.87	1038
Everlight	20	500	10.02	946
QL	5	100	2.46	212
QL	5	500	2.03	194
QL	20	100	9.84	886
QL	20	500	9.03	848

Table 5.2. Densities of species for Ar fill 0.5 Torr, and Hg partial pressure 20 mTorr. No trapping refers to simulations with the vacuum radiative lifetime. The excited state densities increase due to the higher effective lifetime with radiation trapping included in the simulation. The increase in electron densities,and the shortening of the tail of the EED in Fig. 2, suggests that the dominant excited state process is multi-step ionization.

Species	A (w/o trapping)	A (with trapping)	B (w/o trapping)	B (with trapping)	C (w/o trapping)	C (with trapping)
[Hg 6^1S_0] ($\times 10^{14}$)	6.1	6.1	5.7	5.7	5.8	5.8
[Hg 6^3P_1] ($\times 10^{11}$)	0.3	2.4	0.1	1.0	.005	.1
[Hg 6^1P_1] ($\times 10^{10}$)	6.7	20.0	4.6	7.0	.005	.005
[Hg^+], n_e ($\times 10^{12}$)	1.2	2.5	0.6	1.5	0.2	0.3

Table 5.3. Densities of species for Ar fill 0.5 Torr, and Hg partial pressure 5 mTorr. No trapping refers to simulations with the vacuum radiative lifetime. The densities, as well as the EED are not appreciably affected by the radiation trapping (Fig 3 (a)), due to the low concentration of Hg.

Species	A (w/o trapping)	A (with trapping)	B (w/o trapping)	B (with trapping)	C (w/o trapping)	C (with trapping)
[Hg 6^1S_0] ($\times 10^{14}$)	2.3	2.3	1.7	1.7	1.9	1.9
[Hg 6^3P_1] ($\times 10^{11}$)	6.6	7.3	3.0	3.3	.008	.02
[Hg 6^1P_1] ($\times 10^{10}$)	10	13	3.7	5	.002	.002
[Hg^+], n_e ($\times 10^{12}$)	1.5	1.9	0.7	1.1	0.2	0.3

Table 5.4. Densities of species for Ar fill 1.6 Torr, and Hg partial pressure 0.4 Torr. No trapping refers to simulations with the vacuum radiative lifetime. The electron density does not increase significantly with trapping, while the EED tail extends to higher energies (Fig. 3(b)), showing the dominance of superelastic collisions.

Species	A (w/o trapping)	A (with trapping)	B (w/o trapping)	B (with trapping)	C (w/o trapping)	C (with trapping)
[Hg 6^1S_0] ($\times 10^{15}$)	5.6	5.6	5.6	5.6	1.9	1.9
[Hg 6^3P_1] ($\times 10^{11}$)	4.3	5.5	1.9	2.0	.004	.006
[Hg 6^1P_1] ($\times 10^{10}$)	2.1	2.0	0.1	0.2	.002	.002
[Hg^+], n_e ($\times 10^{12}$)	0.5	0.7	1.3	1.4	0.2	0.3

5.9 Figures

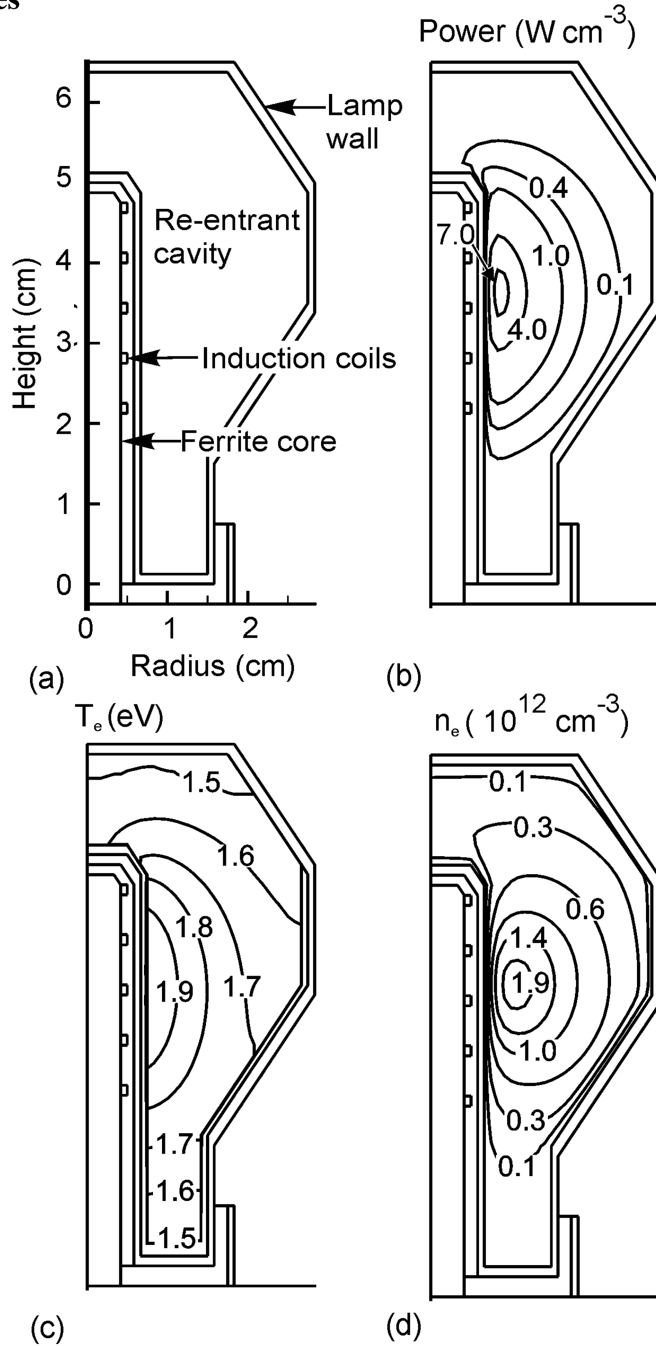

Figure 5.1. Lamp geometry and plasma properties for the base case conditions (Ar 500 mTorr, Hg 5 mTorr, 55 W). (a) Schematic of the lamp, (b) power deposition, (c) electron temperature and (d) electron density. Even thought the skin depth exceeds the dimensions of the lamp, power deposition peaks at inner radii due to geometrical considerations. Contour labels are in units shown at the top of each figure.

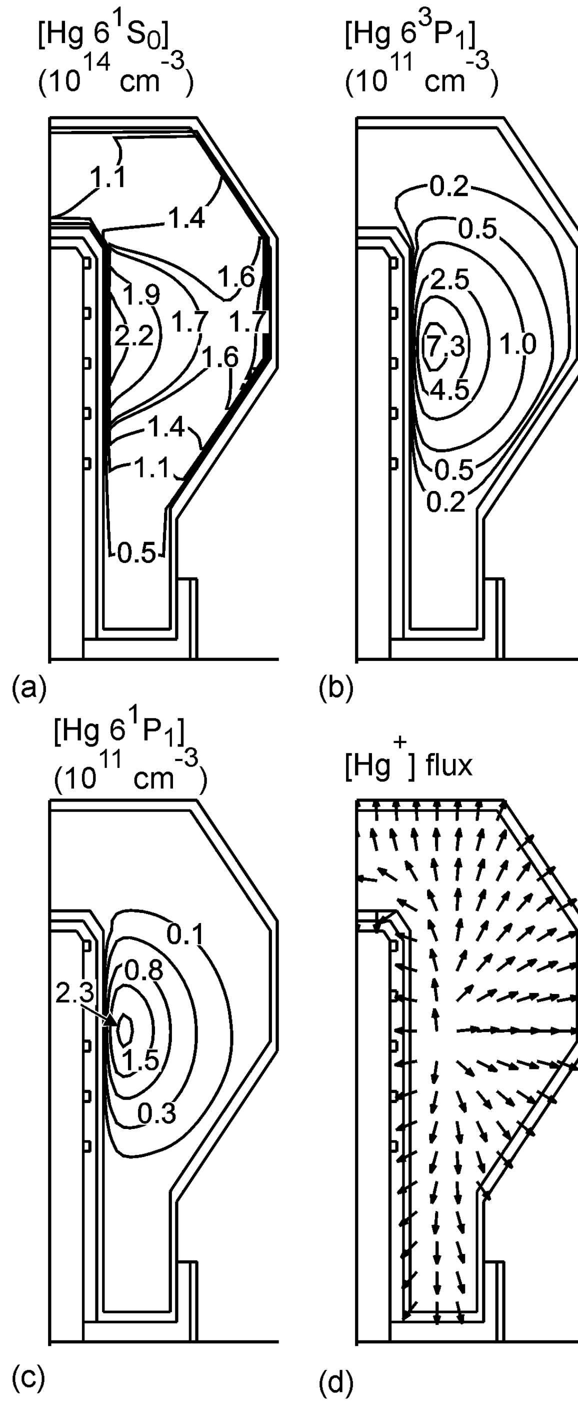

Figure 5.2. Plasma properties for the base case conditions. (a) [Hg (6^1S_0)], (b) [Hg (6^3P_1)], (c) [Hg (6^1P_1)] and (d) flux vectors for Hg^+. The flux vectors show direction only and not magnitude. Cataphoresis and temperature rise decrease the density of ground state Hg.

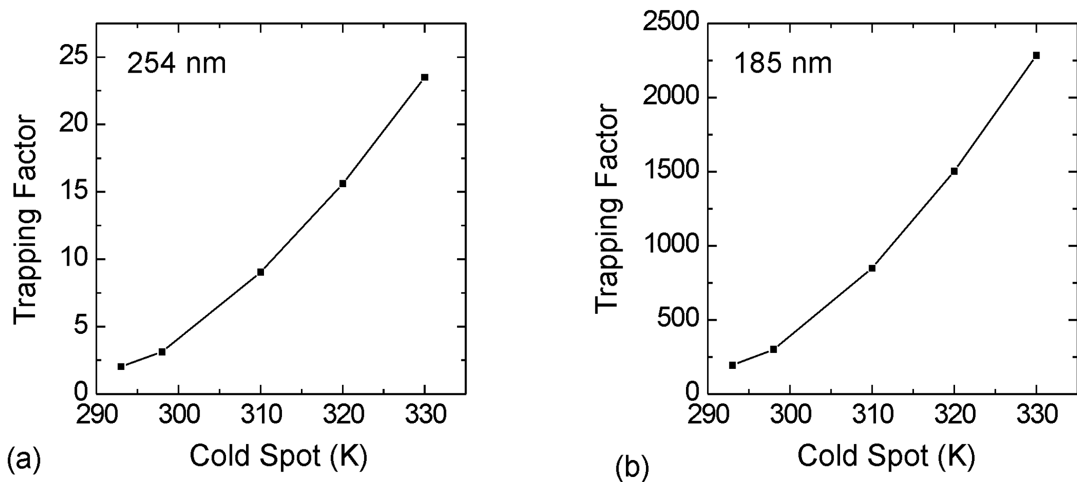

Figure 5.3. Trapping factors as a function of cold spot temperature for the (a) 254 and (b) 185 nm transition. Increasing absorber density increases radiation trapping factors.

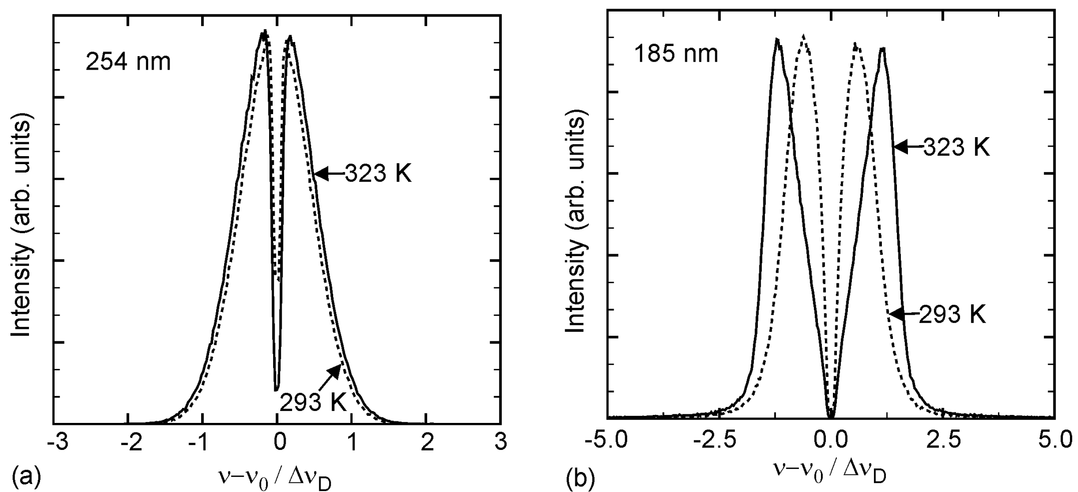

Figure 5.4 . Spectra averaged over photons escaping form the lamp for cold spot temperatures of 310 K and 330 K for the (a) 254 nm and (b) 185 nm transitions. The 185 nm line reversal is more sensitive to the increase in absorber density.

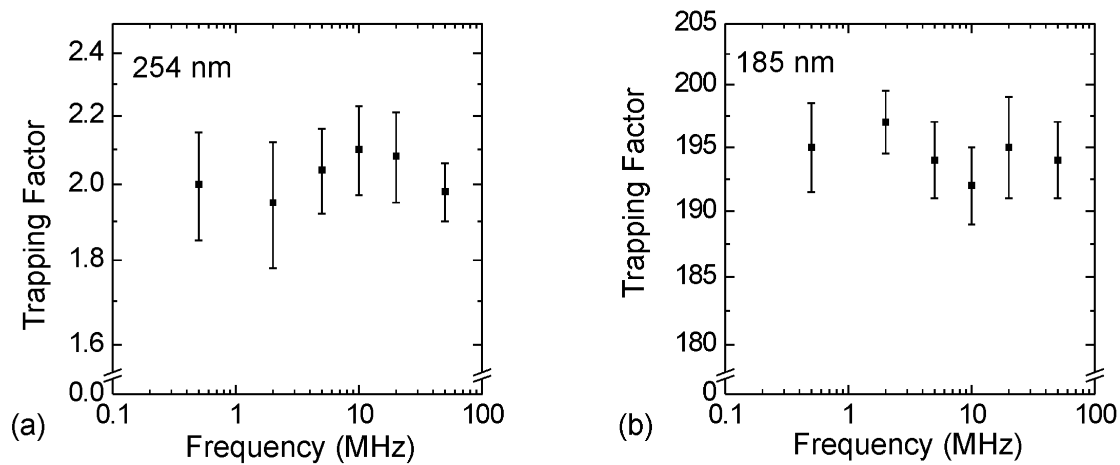

Figure 5.5. Trapping factors as a function of rf source frequency for the (a) 254 nm and (b) 185 nm transitions for the base case conditions. No systematic variations in trapping factor with rf frequency were observed.

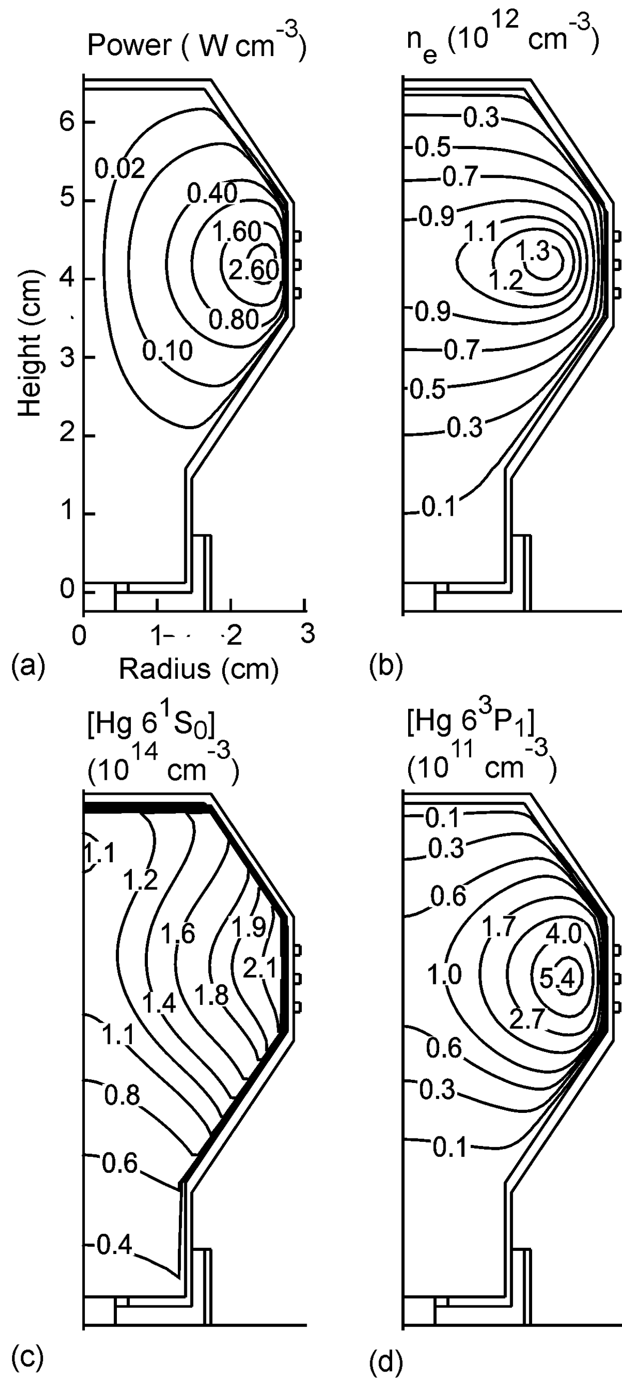

Figure 5.6. Plasma parameters for the Everlight geometry for the base case conditions. (Ar 500 mTorr, Hg 5 mTorr, 55 W) (a) Power deposition, (b) electron density, (c) [Hg (6^1S_0)] and (d) [Hg (6^3P_1)]. The change in coil location changes the distribution of radiators and absorbers.

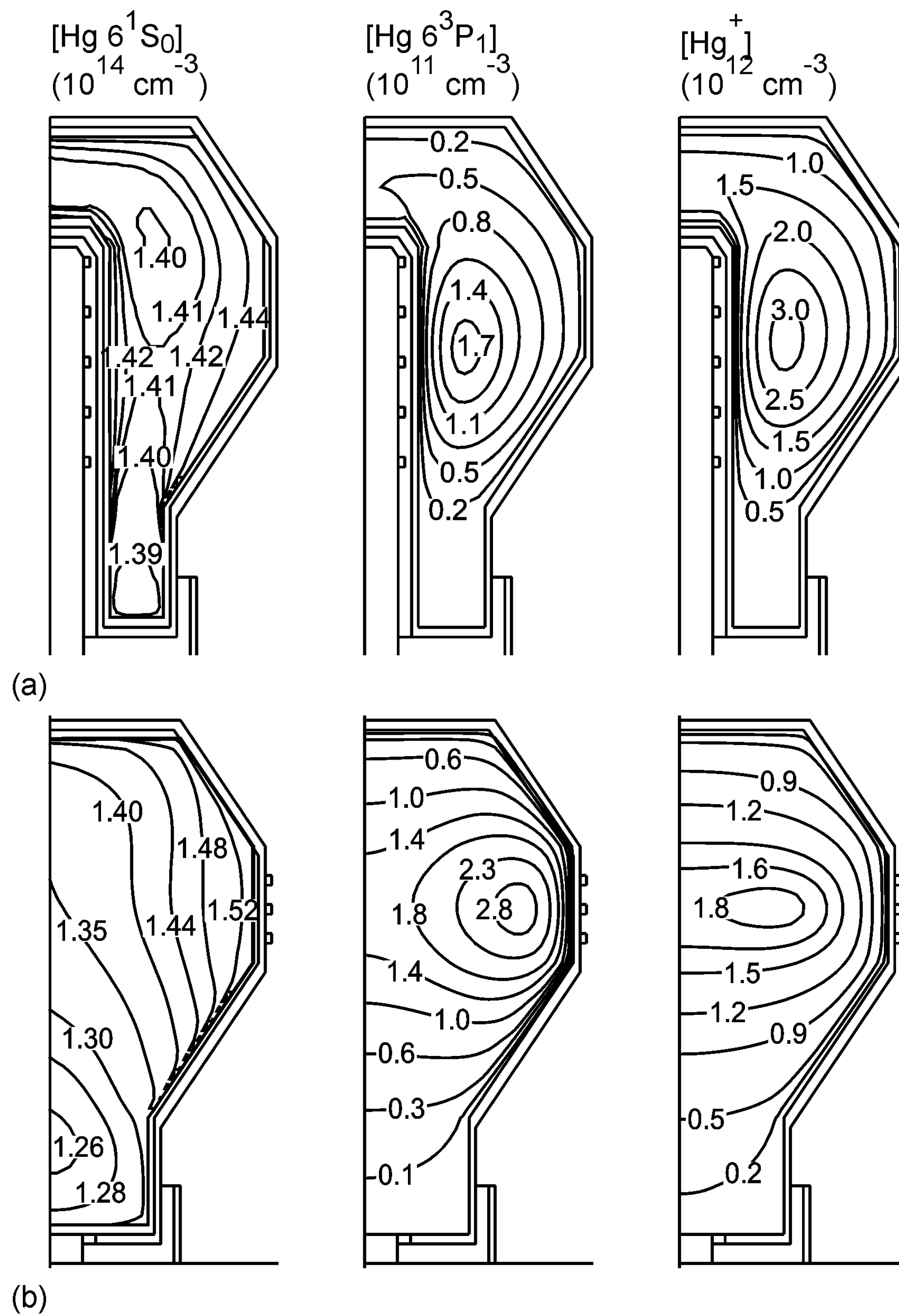

Figure 5.7. Densities of Hg (6^1S_0), Hg (6^3P_1) and Hg^+ for the (a) QL and (b) Everlight geometries for 100 mTorr Ar fill pressure, and 5 mTorr Hg (310 K cold spot).

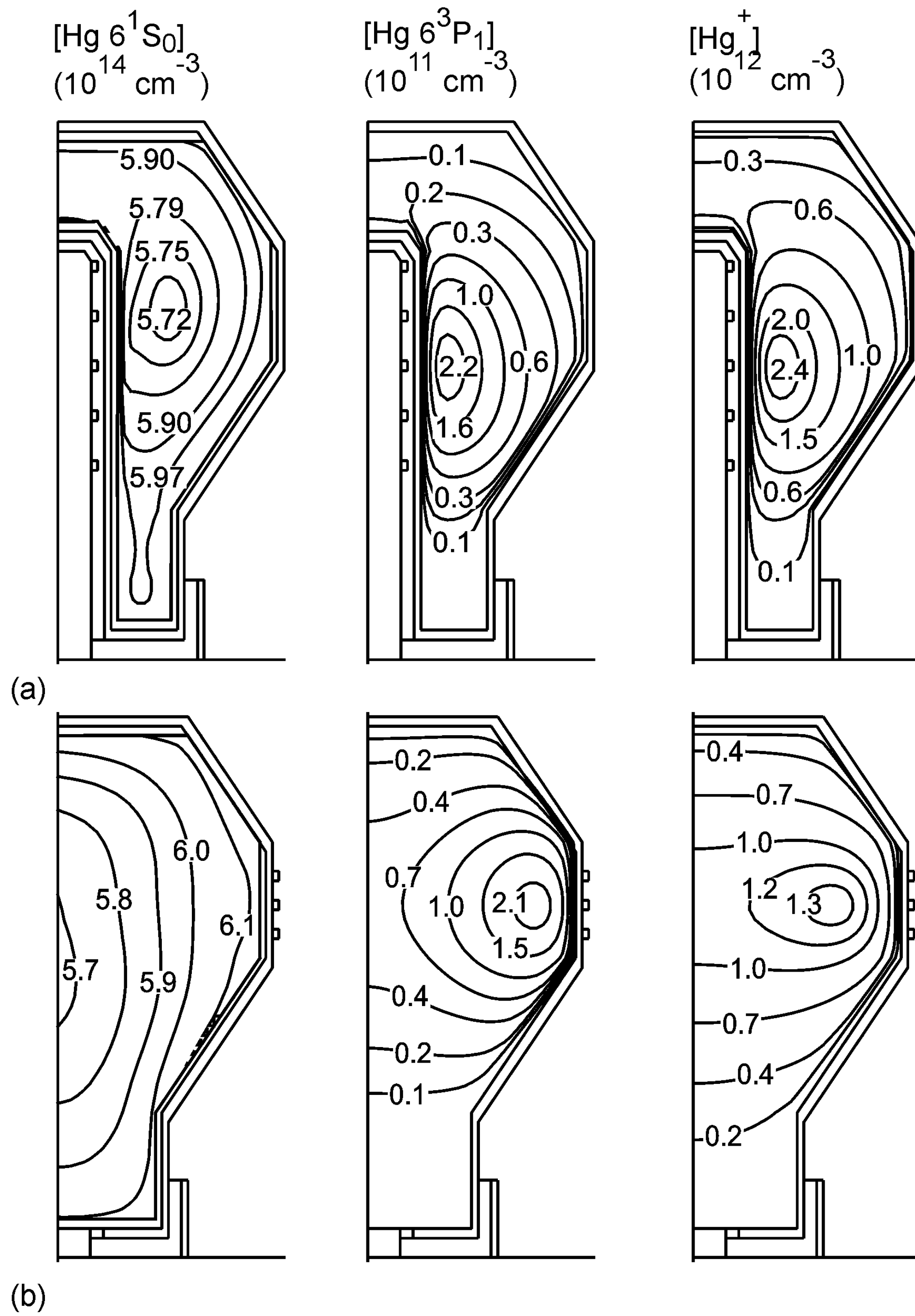

Figure 5.8. Densities of Hg (6^1S_0), Hg (6^3P_1) and Hg^+ for the (a) QL and (b) Everlight geometries for 100 mTorr Ar fill pressure, and 20 mTorr Hg (330 K cold spot).

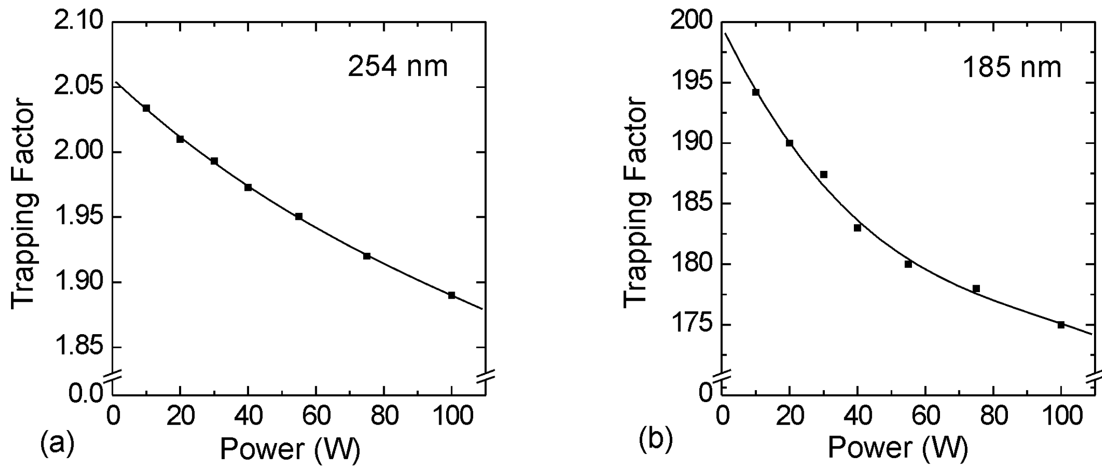

Figure 5.9. Trapping factor as a function of power for the (a) 254 nm and (b) 185 nm transitions, keeping the other parameters at the base values. Increasing power increases the importance of electron collision quenching and cataphoresis in redistributing absorbers.

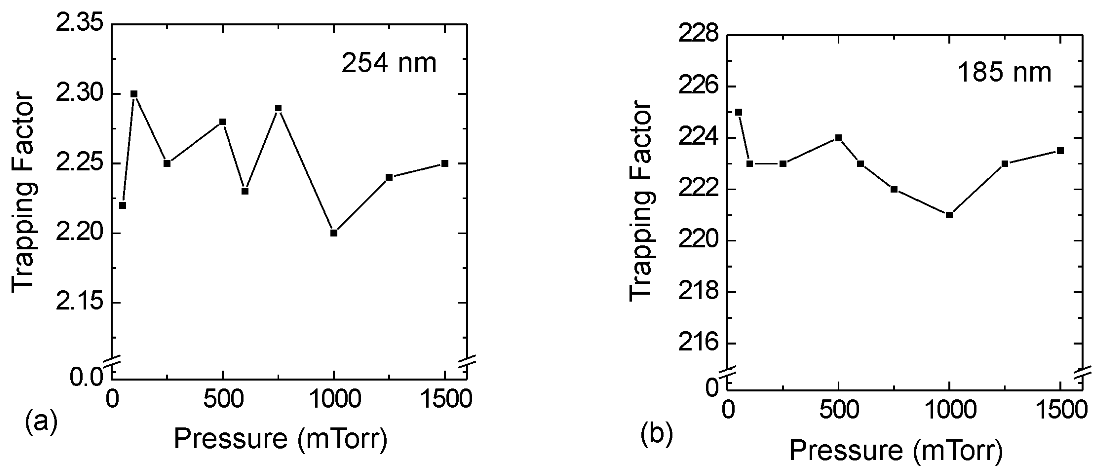

Figure 5.10. Trapping factor as a function of Ar fill pressure for 10 W for the (a) 254 nm and (b) 185 nm transitions, keeping the other parameters at the base values.

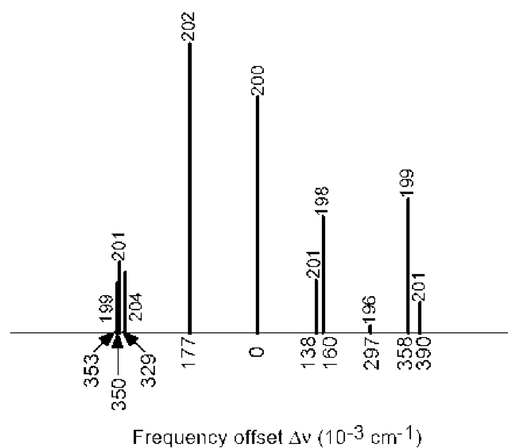

Isotope	Abundance
196	0.146%
198	10.04%
199	16.86%
200	23.08%
201	13.23%
202	29.82%
204	6.82%

	Hyperfine split
199	0.325 : 0.675
201	0.496 : 0.366 : 0.168

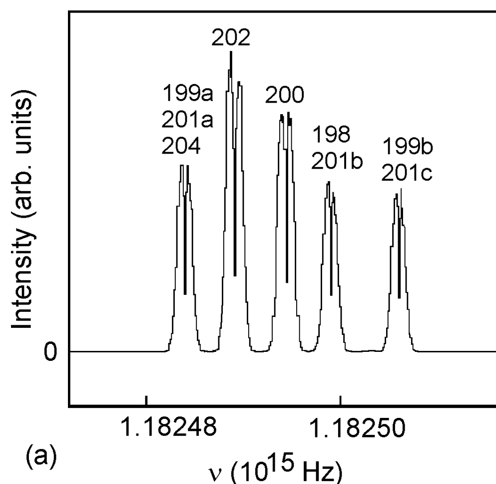

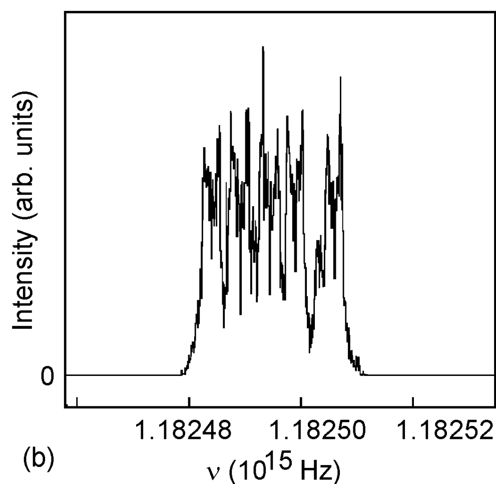

Figure 5.11. Isotopic structure of Hg (above) and Exit spectra when including the complete isotopic structure of Hg for 55 W. (a) 500 mTorr Ar fill pressure, cold spot temperature of 310 K and (b) 1.5 Torr Ar fill pressure, cold spot of 340 K. At the lower pressure and temperature, there is little collisional mixing between the isotopes.

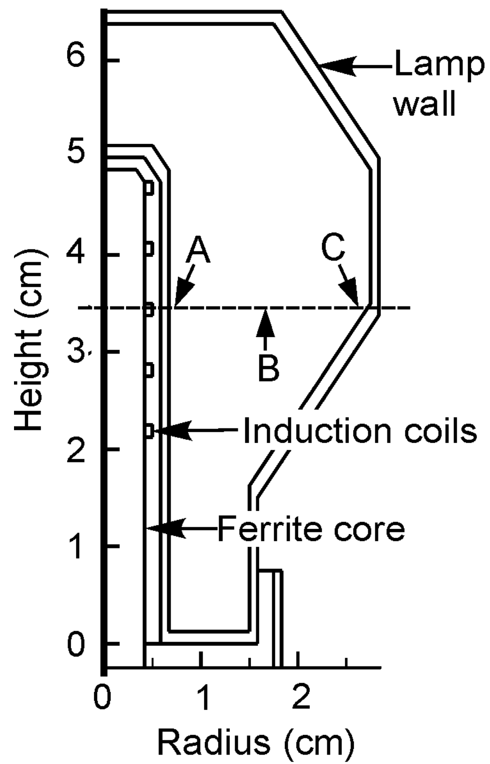

Figure 5.12. Lamp schematic for the simulations to model the effect of radiation transport on electron energy distributions (EEDs). The EEDs are extracted at positions A (region of maximum power deposition), B (bulk plasma), and C (opposite wall, minimum power deposition).

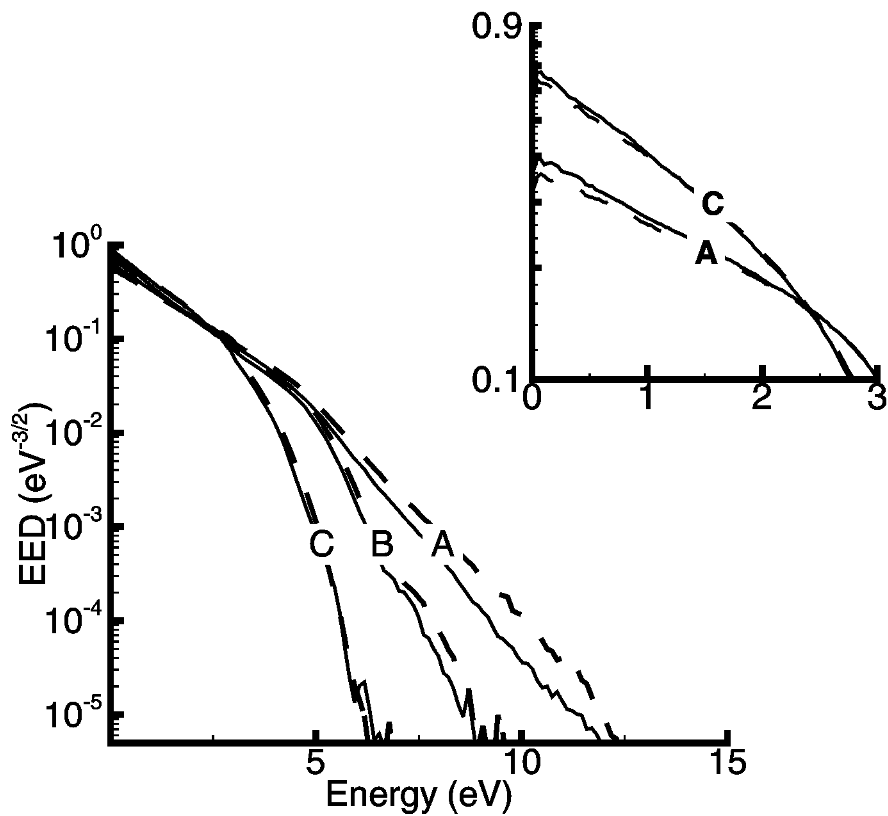

Figure 5.13. The distribution functions for Ar fill of 500 mTorr, and Hg partial pressure of 20 mTorr. The solid lines refer to the simulation including the effect of radiation transport, while the dashed lines refer to the simulation with the radiative lifetime replaced by the vacuum radiative lifetimes. The solid lines have shorter tails and increased bulk electrons (inset), due to an increase in multistep ionization from the radiative excited states.

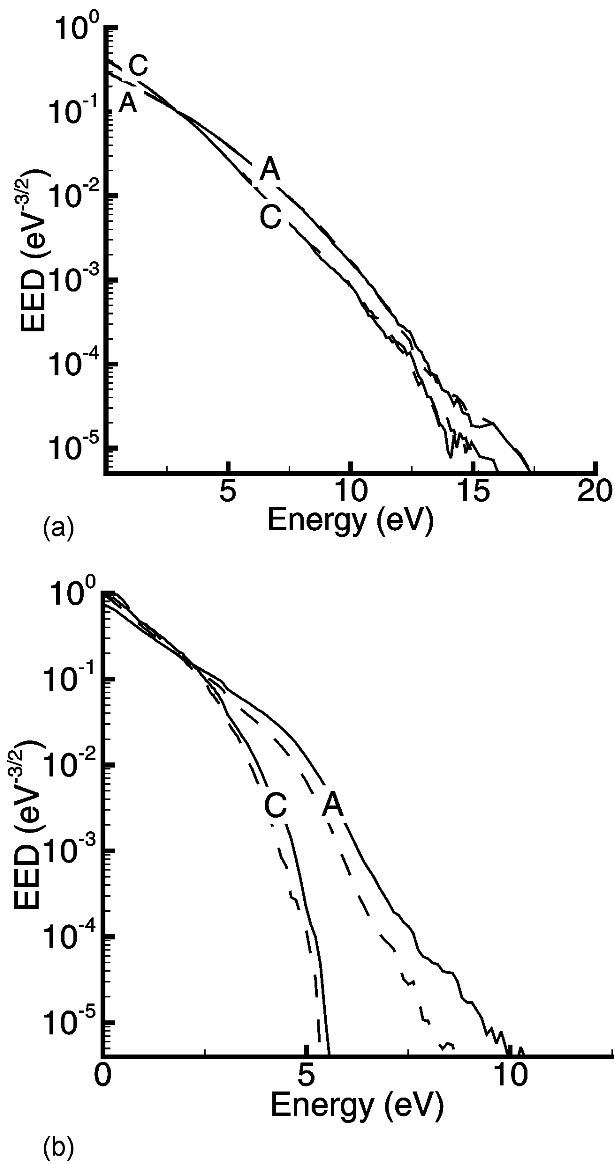

Figure 5.14. Distribution functions with and without the effect of radiation transport. Solid lines refer to the simulation including the effect of radiation transport, while the dashed lines refer to the simulation with the radiative lifetime replaced by the vacuum radiative lifetimes. (a) Ar fill 500 mTorr, Hg partial pressure 5 mTorr: the Hg density is negligible, and does not cause any appreciable change in EEDs due to extended radiative state lifetimes. (b) Ar fill 1.6 Torr, Hg pressure 400 mTorr: at this extremely high Hg density, the superelastic collisions become the dominant process, causing an extension in the EED at higher energies.

5.10 References

1. A. Netten and C.M. Verheij, QL lighting product presentation storybook (Philips Lighting, Eindhoven, Product Literature, 1991; Updated 1994).
2. A. F. Molisch and B. P. Oehry, Radiation Trapping in Atomic Vapours (Clarendon Press, Oxford, 1998).
3. M. A. Liberman and A. J. Lichtenberg, *Principles of Plasma Discharges and Materials Processing* (John Wiley and Sons, Inc., New York, 1994).
4. M. Shinomaya, K. Kobayashi, M. Higashikawa, S. Ukegawa, J. Matsuura, and K. Tanigawa, J. Ill. Engg. Soc. **44** (1991).
5. M. W. Grossman, R. Lagushenko, and J. Maya, Phys. Rev. A **34**, 4094 (1986).
6. A. Hartgers and J. A. M van der Mullen, J. Phys. D **34**, 1907 (2001).
7. K. Wani, J. Appl. Phys. **67**, 6133 (1990).
8. K. Wani, J. Appl. Phys. **68**, 5052 (1990).
9. A. V. Vasenkov and M. J. Kushner,, Phys. Rev. E **66**, 066411 (2002).

6. FLUOROCARBON PLASMAS

6.1 Etching Plasmas

Plasma etching is the process of choice for fabricating sub-micron features in microelectronics fabrication.[1-7] The initiative in research in this field is to increase the number and density of circuit components on an IC chip with each generation of new products. Moore's Law [8] predicts an 18-month doubling of transistor density, which requires a shrinking of minimum feature size. (Fig. 6.1) To keep pace with this trend, the design rules have become more strict, and wet chemical etching processes have been replaced by dry plasma etching.

In wet etching processes, the wafer is immersed in a reactive solution.[9] A patterned etching-resistant photoresist layer provides a mask through which the exposed wafer area is etched. Due to the isotropic nature of liquid etching, the resulting profiles may be undercut, and not of the exact required shape. This places a limit on the attainable feature size. Plasma etching, on the other hand, does not suffer this problem, because the control on anisotropic feature size is possible. This anisotropic etch is due to the channeling of energetic reactants, primarily ions, to the substrate. This energy is controlled by applying a voltage to the substrate to accelerate the ions to 100s of eV in a preferred direction. This voltage is on the order of 100s of volts, providing an energetic as well as anisotropic etch. (Fig. 6.2)

Conventional plasmas are either capacitively coupling (CCP) or inductive coupling (ICP). A schematic of a CCP reactor is shown in Fig. 6.3. A radio frequency (rf) voltage drives a current through a low-pressure gas (100s of mTorr to a few Torr)

between two electrodes, depositing a power of 10s to 1000s of W.[10-11] This power facilitates breakdown of the gas to lead to a weakly ionized (10^{-5} fractional ionization) plasma. The plasma density varies from 10^9 – 10^{11} cm^{-3}, and electron temperature is between 1- 5 eV. In ICP reactors, such as the one shown in Fig. 6.4, the power is coupled to the plasma through electromagnetic fields induced by an antenna.[12-18] The plasma acts a single-turn conductor coupled to a multi-turn rf coil around the dielectric discharge chamber. In these lower pressure devices (10s of mTorr), The fractional ionization in ICPs is higher (10^{-3}) and the electron density is 10^{10}-10^{12} cm^{-3}, while electron temperatures lie between 2-7 eV. The ion energy to the substrate in these plasmas is controlled by independently biasing the substrate electrode using capacitive coupling.

6.2 Plasma Processing of Low-k Dielectrics

The reduction of device sizes on IC chips has resulted in an increase in RC delay time in interconnect wiring.[19] To reduce this delay, novel low-k dielectric materials are being investigated. These may be organic (materials like PTFE, parylene), inorganic (porous silica), or hybrid, as shown in Fig. 6.5.[20] The choice of plasma etching treatment varies for each of these classes of materials.

Inorganic dielectrics are SiO_2 based materials, and are etched in fluorocarbon plasmas. The etching of both porous and solid SiO_2 proceeds through the formation of an overlying polymer layer.[21] This layer is formed by the deposition of C_xF_y precursors.[22] Low energy ion activation enhances the rate of layer growth, while high energy ions and F atoms consume the layer. The polymer layer inhibits the delivery of activation energy to the substrate where SiO_2 polymer complexes are etched away to

volatile SiF_3, and COF_x.[23] This results in an inverse relationship of substrate etch rate (ER) to polymer thickness.[24] However, the composition of the polymer plays an indirect role in the etch process and overlayer formation. This is evident from the fact that the ease of layer growth depends on the number of available open sites for radicals to attach, which in turn depends on the state of fluorination of the $CF_{x\ p}$ site. (Through this dissertation, we shall use the following terminology: C_xF_y refers to neutral gas phase radicals, $C_xF_y^+$ refers to ionic gas phase species, and $CF_{x\ p}$ refers to fluorocarbon sites within the polymer film).

This polymer layer is responsible for the selectivity of etching between SiO_2 and Si.[1] Si substrates do not form complexes with the polymer layer, and there are no intermediates to etch. Etching of Si is due to fluorination of the substrate by neutral fluorine atoms. This process is therefore diffusion dominated, even at small polymer thicknesses. As the polymer layer becomes more than a few nm in thickness, the fluorine atoms cannot diffuse through to the substrate with ease, thereby inhibiting the etch. Ions are also unable to penetrate the thick polymer to deliver activated energy to the susbtrate.

SiO_2 etching, on the other hand, proceeds through multiple channels. Apart from the fluorination process as in Si, the SiO_2 polymer complexes are etched away if a sufficient amount of energy is delivered to the substrate. This energy is carried by ions, and is hence an efficient process if the polymer layer is thin enough to allow the ions to reach the substrate without significant dissipation of energy. Thus in regimes where the polymer thickness is low, the etching of SiO_2 proceeds much quicker than that of Si. This helps in achieving a high selectivity of etch.

Since etching of the wafer occurs through the steady-state fluorocarbon film, it is referred to as an etch-inhibiting film. Some research suggests that at constant ion energy, an increase in thickness of the film results in a reduction in etch rate of the substrate. However, on examining a wider range of process conditions, the film is found to enhance etch in some cases via ion-induced defluorination of the substrate, wherein energetic ions strike the $CF_{x\ p}$ species in the film and release fragmented fluorine atoms that diffuse through to the substrate. This suggests that the extent of fluorine in the film determines the etch rate at these process conditions.

6.3 Plasmas for Deposition

Hydrophobic film coatings have numerous applications in the fields of textiles, biomaterials, and other fields [25-28], for example, in the use of non-fouling substrates and stain-resistant clothes. In addition, these coatings also have low dielectric constants and desirable mechanical properties. A Teflon-like $(CF_2)_n$ structure is found to possess these properties. Fluorocarbon plasmas, are therefore, ideal candidates for the deposition of these films. As such, one needs a good control over generation of the onomer species and incorporation into the polymer network. To achieve this control, modulated (pulsed) fluorocarbon plasma discharges (MD) can be used for deposition of films with the desired hydrophobicity for these applications. Since fluorocarbon plasmas are highly electronegative, and ionic species rapidly recombine with electrons, other ions or diffuse to the walls in the OFF phase of the pulse, the densities and fluxes of charged species can be controlled using MD by varying the duty cycle (the fraction of time the pulse is on).

A reaction mechanism has been proposed by Milella et al for C_2F_4 and C_4F_8 discharges, shown in Fig 6.6.[29] For a low duty cycle (DC), a few radicals are adsorbed onto the surface and diffuse in the OFF phase to reach activated sites before the arrival of other radicals in the ON phase. This leads to the formation of nucleation centers for other incoming CF_x radicals to attach. As a result, the morphology of the polymer structure depends on the duty cycle. For a MD with a low duty cycle, an anisotropic growth leads to films with a ribbon-like structures in an amorphous fluorocarbon film. With larger DC, the morphology is characterized by spherical aggregates, while in the continuous (CW) mode, the coatings are smooth. These trends are shown in Fig 6.7.

6.4 Role of Modeling

The surface kinetics of both etching and deposition plasmas are yet to be understood in their entirety. In this regard, modeling efforts present a low-cost predictive alternative to expensive experiments. The design and execution of an experiment may take days or weeks, while the time taken to run a model is on the order of hours. Also, the modeling approach can be used to efficiently vary external and internal parameters, a choice which is not possible in many experiments.

Two-dimensional plasma models are now used in industry to design plasma processes and equipment.[30-34] These equipment scale models are typically linked to mesoscale and feature scale models to predict the evolution of the properties of microelectronic features. For example, SPEEDIE is a widely used feature profile model using analytic methods.[35] Monte Carlo methods are also used to investigate feature evolution.[5,36-37]

In line with the perception that the overlaying film is etch-inhibiting, most surface modeling research of the etch process characterized the polymer by its thickness. As explained above, this description is incomplete and does not account for etchants arising in the film. Moreover, the rate of film growth (and removal) depends on the constituents of the film. For example, it should be expected that a precursor would bind more easily to a bare C_p site than to a $CF_{2\ p}$ site, due to steric effects and available dangling bonds. The role of plasma generated photons in these processes has not previuolsy been addressed.

One of the applications of deposited hydrophobic films is in the field of biomaterials and nonfouling substrates. The control of structure in these films is, therefore, of extreme importance. The understanding of the underlying surface processes would help in the design of the processes used to deposit hydrophobic films, using process conditions to tailor the properties of the film. Thus, we see that there is a need to address the structure and composition of the fluorocarbon film to understand the etch process in more detail. Hence, a surface model has been developed to resolve the fluorocarbon film structure at a mesoscale level. The state of fluorination of the constituent sites is differentiated. That is, we have C_p, CF_p, $CF_{2\ p}$, and $CF_{3\ p}$ sites in the film. This site differentiation can be viewed in experiment, by XPS, as shown in Fig. 6.8.

6.5 Summary

The motivation for addressing the mesoscale resolved composition of the polymer film formed during etching and deposition has been presented in this chapter. The Surface Kinetics Model used in the studies is described in Chapter 7. The SKM is

interfaced with the HPEM and used to study fluorocarbon plasmas for SiO_2 etching. The results are presented in Chapter 8. The importance of resolving the polymer to account for etchants arising in the film is shown. The etchants released in the film are the dominant etch channels for films where the monomers are strongly bound to the film. The consequences of plasma produced photons on the film are discussed in Chapter 9.

6. 6 Figures

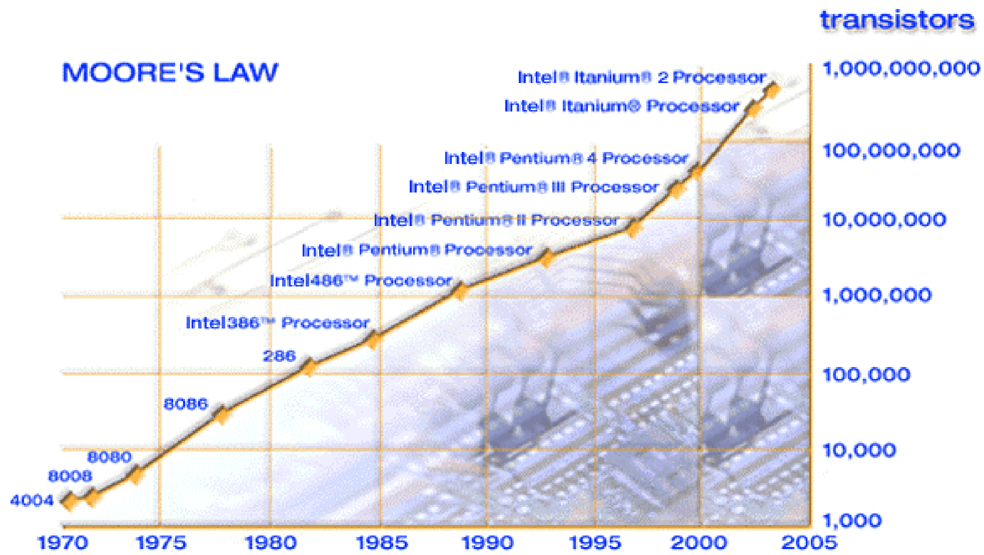

Figure 6.1. Depiction of Moore's Law. [38]

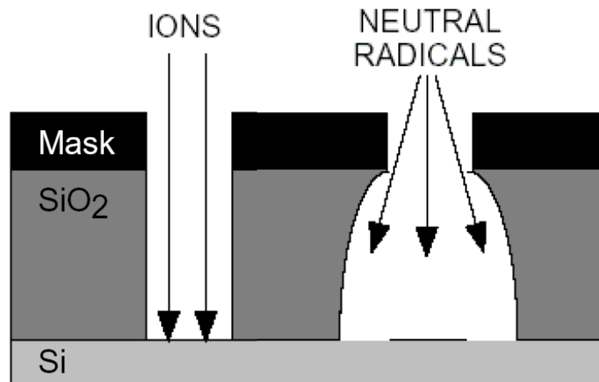

Figure 6.2. Achieving an anisotropic etch profile using energetic ions. The neutrals have isotropic etch profiles.

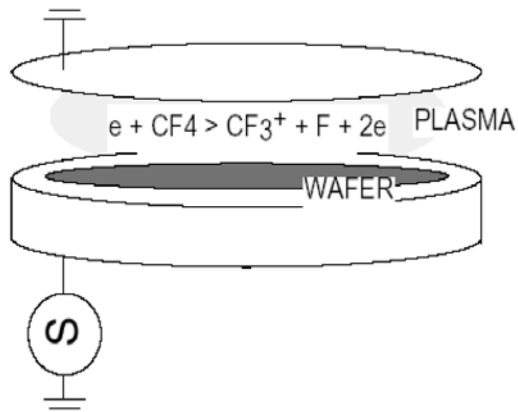

Figure 6.3. Schematic of a capacitively coupled plasma (CCP) reactor

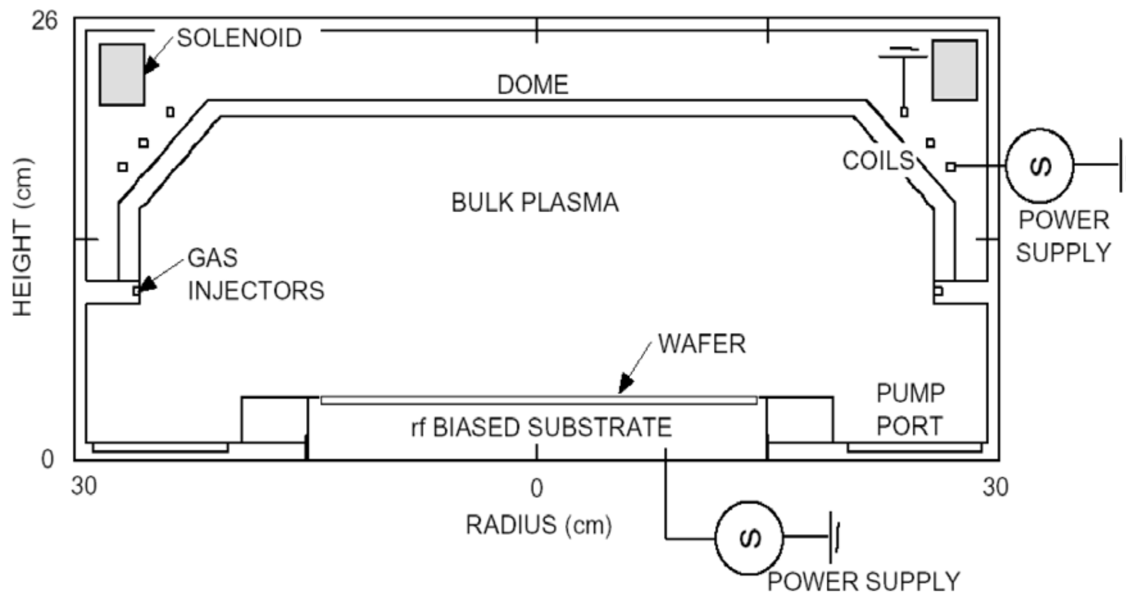

Figure 6.4. Schematic of a typical inductively coupled plasma (ICP) reactor.

Inorganic	Organic	Hybrid
SiO_2	Parylene-N	Benzocyclobutene (BCB)
$SiO_{2-\delta}F_{\gamma}$	Parylene-F	Methyl silsesquioxane (MSQ)
Hydrogen silsesquioxane (HSQ)	Polyarylene ether (PAE-2)	Porous MSQ
Porous HSQ	Polytetrafluoroethylene (PTFE)	Organosilicate glasses (OSG)
Xerogels*	SiLK/porous SiLK	
	Fluorinated polyimide (FPI)	
	FLARE/Porous FLARE	
Fluorocarbon etching chemistry	Oxygen etching chemistry	Fluorocarbon and/ or oxygen chemistry
Resist mask	SiO_2 or Si_3N_4 mask	SiO_2 or Si_3N_4 mask

*contain residual organic groups and could therefore also be listed under hybrid materials

Figure 6.5. Classification of low dielectric constant materials used in microelectronics fabrication. [20]

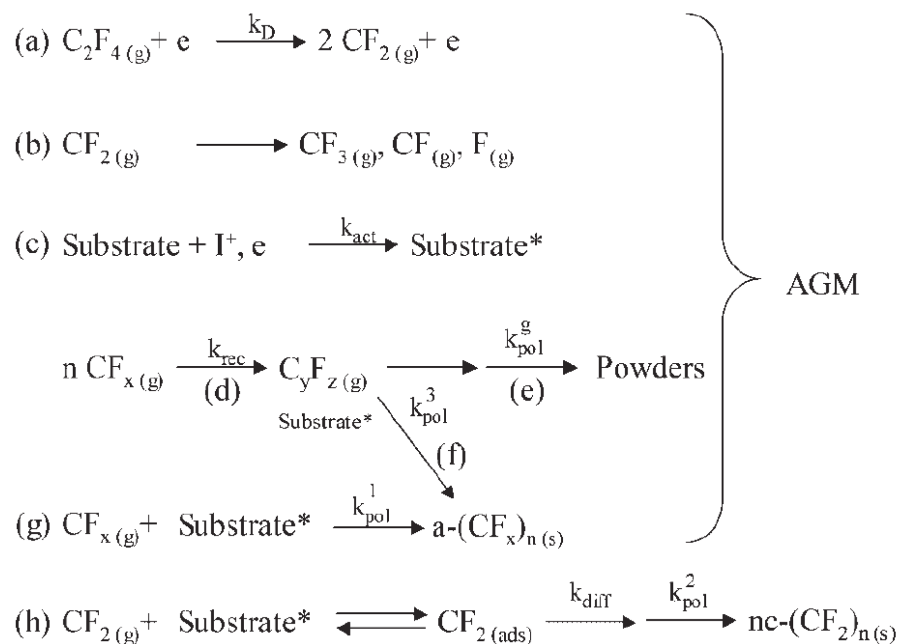

Figure 6.6. Scheme of deposition mechanism for C_2F_4. [29]. AGM refers to the aggregate growth model.

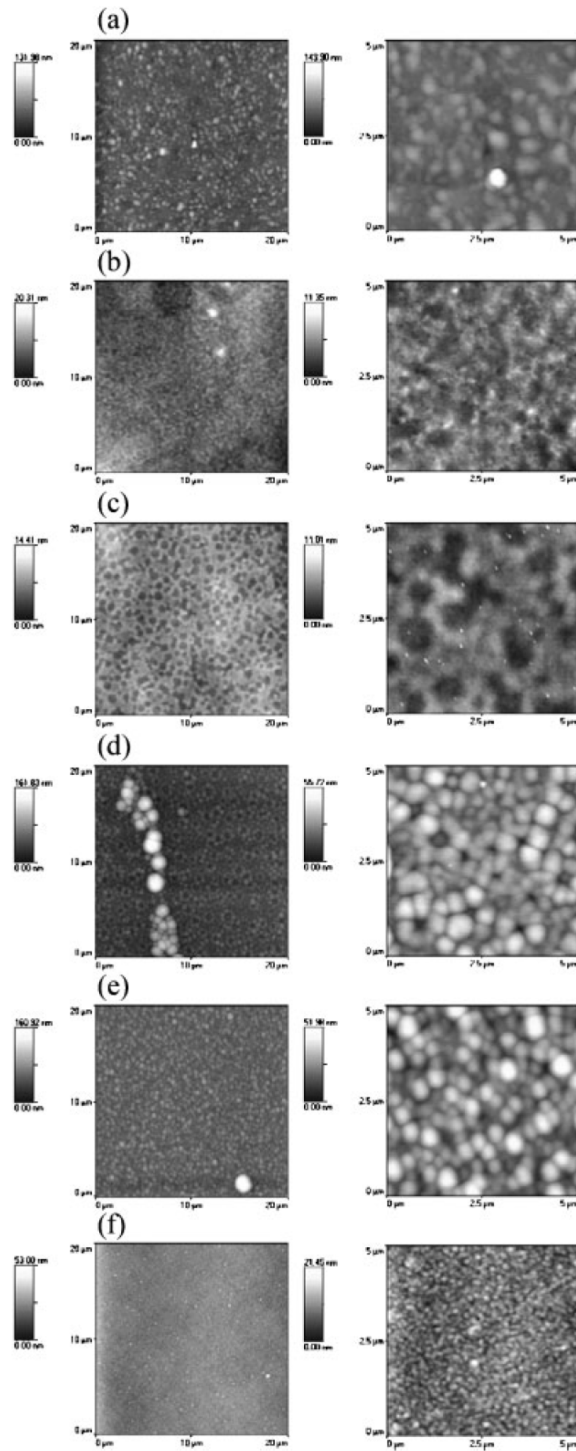

Figure 6.7. AFM images (20 x 20 μm^2, and 5 x 5 μm^2) for 320 ms period in a C_4F_8 (100 W, 300 mTorr) plasma with duty cycle (a) 5%, (b) 10%, (c) 20%, (d) 50%, (e) 70%, and (f) 100%. [29]

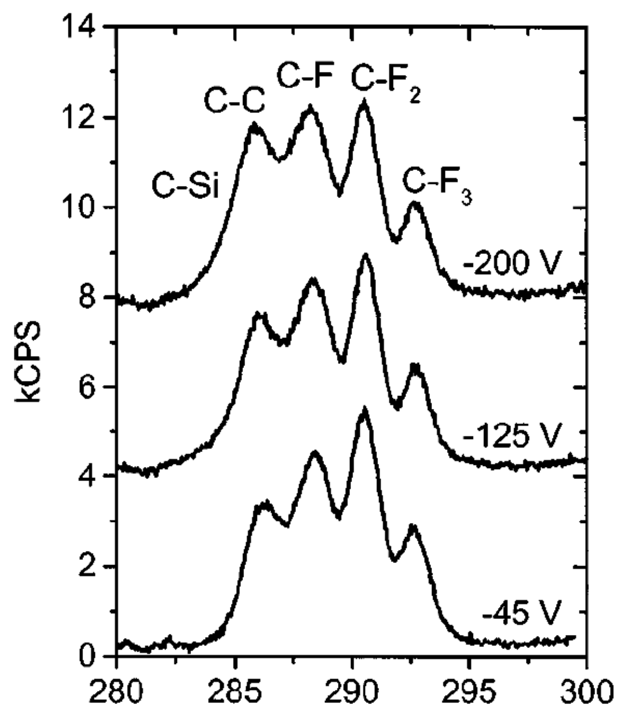

Figure 6.7. Example of XPS spectra of steady-state fluorocarbon films on Si.[39] The surface kinetics model (SKM) has the added capability of resolving the $C\text{-}F_x$ structures above at a mesoscale level.

6.7 References

1. G.S. Oehrlein and J. F. Rembetski, IBM J. Res. Develop. **36**, 140 (1992).
2. Plasma Etching: An Introduction. Edited by D. M. Manos and D. L. Flamm, Academic Press, 1989.
3. M. Inayoshi, M. Ito, M. Hori, and T. Goto, J. Vac. Sci. Technol. A **16**, 233 (1998).
4. M. Armacost, P. D. Hoh, R. Wise, W. yan, J. J. Brown, J. H. Keller, G. A. Kaplita, S. D. Halle, K. P. Muller, M. D. Naeem, S. Srinivasan, H. Y. Ng, M. Gutsche, A. Gutann, and B. Spuler, IBM J. Res. Develop. **43**, 39 (1999).
5. J. P. Chang, A. P. Mahorowala, and H. H. Sawin, J. Vac. Sci. Technol. A **16**, 217 (1998).
6. G. Y. Yeom and M. J. Kushner, Appl. Phys. Lett. **56**, 857 (1990).
7. C. Lee, M. A. Lieberman, and D. B. Graves, Plasma Chem. Plasma. Proc. **16**, 99 (1996).
8. G. E. Moore, Proc. Caltech. Conf. On Very Large Scale Integration, California Institute of Technology, Pasadena, California (1979).
9. J. Hopwood, Plasma Sources Sci. Technol. **1**, 109 (1992).
10. B. N. Chapman, Glow Discharge Processes, John Wiley & Sons Inc., New York, 1980.
11. S. J. Choi, P. L. G. Ventzcek, R. J. Hoekstra, and M. J. Kushner, Plasma Sources Sci. Technol. **3**, 418 (1994).

12. J. B. Carter, J. P. Holland, E. Peltzer, B. Richardson, E. Bogle, H. T. Nguyen, Y. Melaku, D. Gates, and M. Ben-Dor, J. Vac. Sci. Technol. B **11**, 1301 (1993).

13. M. S. Barnes, J. C. Foster, and J. H. Keller, Appl. Phys. Lett. **62**, 2622 (1993).

14. J. R. Woodworth, M. E. Riley, P. A. Riley, and G. A. Hebner, J. Appl. Phys. **81**, 5950 (1997).

15. M. Puttock, Surface and Coatings Technol. **97**, 10 (1997).

16. K. B. Jung, E. S. Lambers, J. R. Childress, S. J. Pearton, M. Jenson, and A. T. Hurst Jr., J. Electrochem. Soc. **145**, 4025 (1998).

17. P. Colpo, E. Ernst, and F. Rossi, J. Appl. Phys. **85**, 1366 (1999).

18. M. V. Malyshev, V. M. Donnelly, and S. Samukawa, J. Appl. Phys. **84**, 1222 (1998).

19. S.-J. Wang, H.-H Park, and G.-Y. Yeom, Jap. J. Appl. Phys. **39**, 7007 (2000).

20. G. S. Oehrlein, T. E. F. M. Standaert, and P. J. Matsuo, in *Solid State Technology; Vol. May 2000*, 125(2000).

21. A. J. Bariya, C. W. Frank, and J. P. McVittie, J. Electrochem. Soc. **137**, 2575 (1990).

22. T. E. F. M. Standaert, M. Schaepkens, N. R. Rueger, P. G. M. Sebel, G. S. Oehrlein, and J. M. Cook, J. Vac. Sci. Technol. A **16**, 239 (1998).

23. M. Matsui, T. Tatsumi, and M. Sekine, J. Vac. Sci. Technol. A **19**, 2089 (2001).

24. N. R. Rueger, J. J. Beulens, M. Schaepkens, M. F. Doemling, J. M. Mirza, T. E. F. M. Standaert, and G. S. Oehrlein, J. Vac. Sci. Technol. A **15**, 1881 (1997).

25. V. Panchalingam, B. Poon, H. H. Huo, C. R. Savage, R. B. Timmons, and R. C. Eberhart, J. Biomat. Sci. Polym. Ed. **5**, 131 (1993).

26. S. J. Limb, K. K. Gleason, D. J. Edell, and E. F. Gleason, J. Vac. Sci. Technol. A **15**, 1814 (1997).

27. S. R. Coulson, I. S. Woodward, S. A. Brewer, C. Willis, and J. P. B. Badyal, Chem. Mater. **12**, 2031 (2000).

28. S. J. Limb, K. K. S. Lau, D. J. Edell, E. F. Gleason, and K. K. Gleason, Plasmas Polym. **4**, 21 (1999).

29. A. Milella, F. Palumbo, P. Favia, G. Cicala, and R. d'Agostino, Plasma Process Polym. **I**, 164 (2004).

30. G. DiPeso, V. Vahedi, D. W. Hewett, and T. D. Rognlien, J. Vac. Sci. Technol. A **12**, 1387 (1994).

31. D. P. Lymberopoulos and D. J. Economou, J. Appl. Phys. **73**, 3668 (1993).

32. P. L. G. Ventzek, R. J. Hoekstra, T. J. Sommerer, and M. J. Kushner, J. Vac. Sci. Technol. B **12**, 461 (1994).

33. J. P. D. Passchier and W. J. Goedheer, J. Appl. Phys **74**, 3744 (1993).

34. D. J. Economou, T. J. Bartel, R. S. Wise, and D. P. Lymberopoulos, IEEE Trans. Plasma Sci. **23**, 581 (1995).

35. J. I. Ulacia F. and J. P. McVittie, J. Appl. Phys. **65**, 1484 (1989).

36. A. P. Mahorowala and H. H. Sawin, J. Vac. Sci. Technol. B **20**, 1084 (2002).

37. A. Sankaran and M. J. Kushner, J. Vac. Sci. Technol. A **22**, 1242 (2004).

38. Intel research in Si, http://www.intel.com/research/silicon/mooreslaw.htm

39. T. E. F. M. Standaert, C. Hedlund, E. A. Joseph, G. S. Oehrlein, and T. J. Dalton, J. Vac. Sci. Technol. A **22**, 53 (2004).

7. SURFACE KINETICS MODEL

7.1 Introduction

Plasma processing reactors for etching and deposition have reactive species that interact with walls and substrates. This is especially true in low-pressure reactors, where the mean free path for species transport is large.[1] In the case of etching reactors, the consequences of the plasma-surface interactions on the etch as well as the bulk plasma have been studied.[2-6] Schaepkens et al have shown that the wall temperature of an etch chamber affects the sticking coefficient of the fluorocarbon radicals on the walls.[4] This has effects on the etch rate, as well as the bulk gas phase densities. There have been models that address the plasma equipment, bulk and surface processes separately [7-11], but very few research efforts that consistently study both simultaneously, to account for feedback of surface interactions to bulk processes.

To this end, the HPEM (Chapter 3) has been interfaced with a Surface Kinetics Model (SKM). Most of the physics of this model has been developed earlier, and is reviewed again here.[12] The SKM implements a modified surface-site balance algorithm along the plasma-surface boundary, and outputs, surface coverages, thickness and composition of overlaying films, reactive sticking coefficients, and modified fluxes of species returning to the plasma. Aside from the gaseous species being directly available as surface reactants, there is also the possibility (e.g. in fluorocarbon plasmas), of overlaying films, through which the gaseous species diffuse to the available surface sites. In addition, the constituents of the film may also react with the gaseous species and

the underlying substrate. The SKM is capable of handling all of the above processes. A comparison of a conventional surface site balance model and the SKM is shown in Fig. 7.1.

7.2 Description of Surface Kinetics Model

For each plasma species interacting with a surface, a reaction probability S_{im} for the ith plasma species and the mth material is defined. Depending on the surface reaction mechanism, species are "reflected" back into the plasma. The reflecting flux of a species back to the bulk plasma is

$$\Phi^{R}{}_{im} = \left(1 - S_{im}\right) \cdot \Phi^{I}{}_{im}\,, \tag{7.1}$$

where $\Phi^{I}{}_{im}$ is the incident flux of the species i to the surface m. We also specified that each incident species may produce other species on the surface. So for a species i incident onto surface m, the flux of the jth generated species returning to the plasma is

$$\Phi^{R}{}_{ijm} = f_{ijm} \cdot \Phi^{I}{}_{im}\,, \tag{7.2}$$

where f_{ijm} is the fractional generation rate. For example, consider an CF_2 ion (species 1) striking a wall passivated by a CF_{3p} polymer (material 4), neutralizing to form ground state CF_2 (species 2) with unity probability and sputtering CF_3 (species 3) with probability of 0.01. The coefficients are $S_{14} = 1, f_{124} = 1, f_{134} = 0.2$.

The values of S_{im} and f_{ijm} ultimately depend on surface coverages, and on the

fluxes and energies of reactants, and therefore the SKM is needed. The SKM identifies specified surface locations on chosen materials, sets the initial surface species coverages, and extracts reactive fluxes to the surface. Based on a specified surface reaction mechanism, differential equations for fractional occupancy of surface sites and thickness and composition of overlaying polymer layers are integrated in time. These simulations may or may not be performed in lockstep integration with the plasma model. This process is continued for a user-specified time, and the resulting coefficients S_{ik} and f_{ijk} are fed back to the plasma model for the subsequent iteration. Etching or deposition rates are obtained based on the surface coverages and reactive fluxes at the end of the call to the SKM. The flow chart of the integrated model is shown in Fig. 7.2.

As described in the reference, there are three classes of surface processes used in the SKM.[12] The first class involves the reactions of non-ionic plasma species with the first exposed layer of the boundary. This may be an exposed substrate site, or a polymer site. In the absence of overlayer formation, this class of reactions would be sufficient to model the surface evolution. The generic form of these reactions is

$$A_g + B_s \xrightarrow{k_i} C_s + D_g + E_g, \tag{7.3}$$

where the subscript g denotes a gas phase species and the subscript s denotes a surface resident species or a surface site, and k_i is the reaction probability of the ith reaction. The evolution rate of the surface coverage of species species B on m contributed by the ith reaction $(\partial\theta_{Bm} /\partial t)_i$ is

$$\left(\frac{\partial \theta_{Bm}}{\partial t}\right)_i = -\frac{1}{T} R_{im} , \tag{7.4}$$

where T is the total surface site density per unit area, and

$$R_{im} = k_i \cdot \Phi^I_{Am} \cdot \theta_{Bm} , \tag{7.5}$$

where Φ^I_{Am} is the incident plasma flux of species A on m, θ_{Bm} is the fractional surface coverage of surface species or site B on m. The surface reaction coefficient S_{Am} for incident plasma species A on material m, which is used in the bulk plasma model, is then the sum of the reaction rates of all processes including A as a reactant:

$$S_{Am} = \sum_{j=1}^{s} \sum_{i=1}^{n} \frac{R_{iAjm}}{\Phi^I_{Am}} = \sum_{j=1}^{s} \sum_{i=1}^{n} k_i \theta_{jm} , \tag{7.6}$$

For ion-energy dependent surface processes, the rates of the reactions are typically characterized by a threshold energy and an exponential energy dependence [13],

$$p(E) = p_0 \cdot \frac{E^m - E^m_{th}}{E^m_{ref} - E^m_{th}} , \tag{7.7}$$

where $p(E)$ is the reaction probability for an ion with energy E, E_{th} is the threshold energy of the process, E_{ref} is a reference energy, and p_0 is the reaction probability at the reference energy. The value of $m = 1/2$ was used in this work.

The second class of reactions is between surface species, or between a surface species and a polymer species. This includes reactions that form SiO_2-CF_x complexes at the interface between substrate and polymer. The rates of these reactions are (for polymer species B and surface species A):

$$R_{AB} = \nu \cdot \frac{[A_s]}{T} \cdot \frac{[B_p]}{T \cdot L^t}, \tag{7.8}$$

where ν is a user-supplied "frequency", T is the surface density of sites (10^{15} cm^{-2}), L^t is the thickness of the polymer (in monolayers), $[B_p]$ is the contribution of species B to the polymer (in monolayers), and $[A_s]$ is the surface density of species A.

The third class of reactions involves the transport of species through the overlayers. As explained in the previous chapter, in etching plasmas, the thickness of the layers inhibits the energy transported by the ions to the substrate. The SKM first solves for the thickness of the polymer layer. In the case of the resolved composition of the polymer, this is just given by

$$L^t = \sum_{i=0}^{3} [CF_{i\ p}] \tag{7.9}$$

where $[CF_{i\,p}]$ is the effective thickness of the $CF_{i\,p}$ component of the polymer layer.

The ion inhibition at the substrate due to the traversal through the overlayer is governed by

$$p(E) \propto \frac{1}{(1+\alpha L^t)^2} \tag{7.10}$$

where α is a parameter which is chosen to be 0.3 for the purposes of the study. Thus, as the polymer becomes thicker, the ion loses most of its energy in the first few monolayers.

7.3 Surface Reaction Mechanisms in Fluorocarbon Plasma Etching of SiO_2

The SiO_2 reaction mechanism is schematically shown in Fig. 7.3, and described in Table 7.1. The major steps in the mechanism are as follows. In summary, a polymer is grown on the SiO_2 surface by C_xF_y deposition. Low-energy ion bombardment activates polymer surface sites for faster neutral sticking. Ion sputtering, F atom etching, and ion assisted polymer-wafer interaction consume the polymer, and the steady state thickness of the polymer is reached as the balance of its deposition and consumption. The polymer-wafer interaction consumes the SiO_2 wafer as well as the polymer. $CF_{x\leq 2}$ chemisorption on SiO_2 sites produces SiF_xCO_2 surface complexes which dissociate to SiF_x sites upon ion bombardment or F atom interaction. The SiF_x species are then removed by either ion chemical sputtering or F atom etching. Because the polymer passivation layer limits mass diffusion and dissipates energy, the rates of reactions

involving energy transfer or species diffusion through the polymer are polymer thickness dependent.

The polymer strongly influences the etch rate by limiting the fluxes of reactants to the wafer, dissipating ion bombarding energy, and providing reactants for removal of oxygen from the film. SiO_2 and Si etch rates generally decrease with increasing polymer thickness due to this barrier to mass and energy transport [4]. The first step in describing the surface reaction mechanisms is to capture the kinetics of the polymer formation. The precursors for the polymer growth are generally believed to be C_mF_n radicals with sufficient dangling bonds to build a polymeric network [5,14]. In our work, these polymerizing species are C, CF, CF_2, CF_3, C_2F_3, and C_2F_4. In the surface reaction mechanism, the steric factors in rates have been taken into account. For example, a CF radical attaches easier to a surface site than a bulkier CF_3 radical. Also, the number of dangling bonds has also been taken into account. That is, a radical would attach with greater ease to a C_p site than to a CF_p site. There is only physisorption onto a $CF_{3\ p}$ site, as there are no available bonds to accommodate incoming radicals.

It has been observed that polymer layers can achieve a steady state thickness during etching [10,15], which implies that some polymer consumption processes occur simultaneously during its deposition. One such process is the F atom etching of the polymer. F atoms terminate the dangling bonds of carbon in the polymer to form volatile products such as CF_4. As F atoms can diffuse into the polymer to react internally, this process appears to be a bulk reaction. Another polymer consuming process is energetic ion sputtering. For example, Oehrlein et al. observed decreasing polymer thickness with increasing substrate bias in inductively coupled plasmas [10]. In these systems the

substrate bias does not significantly change the magnitude of the reactant flux and only changes the ion bombarding energy. As such, the decreasing passivation thickness with increasing bias should be attributed to the increasing rate of ion sputtering consumption of the polymer. Another role ions may play in polymerization kinetics is to activate surface sites. Sputtering dominates the contribution of ions to the polymerization kinetics when the ion energy is large (e.g., > 100 eV). However, when the ion energy is low (10s of eV), enhancement of polymer formation by ions has been observed.[16] These observations were attributed to the low-energy ion activation of polymeric surface sites for neutral radical sticking. We modeled the ion activation process as having an ion-energy-dependent reaction probability *k* of

$$k = k_0 \times \text{Max}\left(0, 1 - \frac{E_i}{E_c}\right), \tag{7.11}$$

where E_i is the incident ion energy, E_c is the maximum energy allowable for the process, and k_0 is the probability at zero incident ion energy. After being activated, the surface sites are more likely to chemisorb polymerizing neutrals.

Another important process is that of ion-induced defluorination.[17] Energetic ions strike the $CF_{x\ p}$ site and remove an F radical which can then diffuse through the substrate to facilitate an etch. Though this is, in principle, a bulk process, most of the ion energy dissipation occurs in the first few nm of the layer, and we are justified in treating this as a surface process. Moreover, the surface model is well-mixed and homogeneous. That is, there is no variation of composition spatially, and that the densities of the surface species are assumed to be homogeneous throughout the surface. For this reason, there is no method to

identify at what position the F atom is released in the layer, and hence of the distance to the SiO_2 substrate. Therefore, we assume that the F releases into the gas phase, as shown in the reaction chemistry. As an alternative, we assumed that the fluorine released due to ion impact is taken as a different species (F_d), which has a higher rate of reaction with the substrate. This higher rate is intended to reflect the shorter distance that the impact-released fluorine has to traverse to reach the substrate. Results from these two models are presented in Chapter 8.

Another consuming process for the polymer occurs at the polymer-wafer interface. Experiments have shown that for the same process conditions, thinner passivation occurs on SiO_2 than on Si [15]. After the passivation thickness exceeds one monolayer, the kinetics of polymer growth should be the same for different wafer materials if the kinetics depends only on incident neutral and ion fluxes. The observation that the polymer thickness depends on the wafer material implies that interactions at the polymer-wafer interface can consume the polymer. For SiO_2 substrates, the oxygen atoms in the film react with the carbon atoms in the polymer to release volatile products such as CO_2 [18]. The polymer-wafer interactions, however, require activation energy which must be provided by ion bombardment through the overlying polymer layer. During the transfer of the ion bombarding energy through the layer, some portion of the energy is dissipated in the polymer by bond breaking and heating with only a fraction reaching the surface. Consequently, the efficiency of the energy transfer decreases with increasing polymer thickness, and as a result the probabilities of polymer-wafer reactions depend on the polymer thickness. We therefore use Eq. 7.10 to describe the decay in ion energy due to traversal through the polymer.

In addition to polymer consumption, polymer-surface interactions also contribute to wafer etching. The carbon atoms in the polymer in contact with SiO_2, coincident with ion bombardment through the polymer layer, abstract oxygen atoms from the oxide. This process generates volatile CO_2 and leaves the target Si atoms in the oxide partially passivated by F atoms. The F atoms which diffuse through the polymer successively passivate the Si sites, eventually forming volatile SiF_n products. In this part of the mechanism the first layer of the polymer passivation is a precursor for etching.

Another pathway for neutral passivation of the SiO_2 wafer is through direct $CF_{x\leq2}$ neutral chemisorption to SiO_2 sites to form SiF_xCO_2 intermediate complexes. These complexes dissociate to SiF_x surface sites and CO_2 gas upon ion bombardment or F atom passivation. As in Si etching, F atoms then saturate the dangling bonds of SiF_x until producing volatile products.

In Chapter 9, we study the effects of UV photons on the SiO_2 etch process. These photons are assumed to defluorinate the layer like in ion-induced defluorination. However, photons can penetrate the layer, and hence UV-induced defluorination is a bulk process.

7.4 Summary

The Surface Kinetics Model has been described in this chapter. A more detailed description can be found in the work by Zhang and Kushner.[12] A surface reaction chemistry for fluorocarbon plasmas has been developed. As input, the SKM also needs the incident fluxes from the bulk plasma model. In the upcoming chapter, this model

shall be interfaced with a two-dimensional model (HPEM), to validate and parametrize the effect of bulk plasma conditions on the surface.

7.5 Tables

Table 7.1 Surface reactions for SiO_2 Etching in Fluorocarbon (FC) plasma.

Species	Symbol
Polymerizing radicals	CF_x, C_xF_y
Ions	I^+ (non-FC), CF_3^+ (generic FC)
Activated sites	* (superscript)
Surface species	s (subscript)
Gas phase species	g (subscript)
Polymer species	p (subscript)

Reaction[a,b]	Probability	
Formation of complex at polymer-SiO_2 interface:		
$SiO_{2\,s} + CF_{x\,g} \rightarrow SiO_2CF_{x\,p}$	1.	d
$SiO_{2\,s} + C_xF_{y\,g} \rightarrow SiO_2C_xF_{y\,p}$	1.	d
$SiO_{2\,s} + CF_{x\,p} \rightarrow SiO_2CF_{x\,p}$	1.	d
Low energy ion activation of polymer site		
$CF_{x\,p} + I^+ \rightarrow CF_x{}^*{}_p$	k_0=0.011	e

Table 7.1 (contd.)

$C_xF_{y\,p} + I^+ \rightarrow CF_x^{*}{}_p$	k_0=0.011	e
Ion activated dissociation of complex		
$SiO_2CF_{x\,p} + CF_3^+{}_g \rightarrow CF_{3\,g} + CO_{2\,g} + SiF_{x\,s}$	p_0=0.3	f,h
$SiO_2CF_{x\,p} + I^+{}_g \rightarrow I_g + CO_{2\,g} + SiF_{x\,s}$	p_0=0.3	f,h
$SiO_2CF_x^{*}{}_p + CF_3^+{}_g \rightarrow CF_{3\,g} + CO_{2\,g} + SiF_{x\,s}$	p_0=0.3	f,h
$SiO_2CF_x^{*}{}_p + I^+{}_g \rightarrow I_g + CO_{2\,g} + SiF_{x\,s}$	p_0=0.3	f,h
Etch reactions		
$SiF_{x\,s} + CF_3^+{}_g \rightarrow CF_{3\,g} + SiF_{x\,g} + SiO_{2\,s}$	p_0=0.023	f,g,h
$SiF_{x\,s} + I^+{}_g \rightarrow I_g + SiF_{x\,g} + SiO_{2\,s}$	p_0=0.023	f,g,h
$SiF_{3\,s} + F_g \rightarrow SiF_{4\,g}$	p_0=0.023	f,g
Fluorination		
$SiF_s + F_g \rightarrow SiF_{2\,s}$	0.0005	f
$SiF_{2\,s} + F_g \rightarrow SiF_{3\,s}$	0.0005	f
$SiF_{3\,s} + F_g \rightarrow SiF_{4\,g}$	0.0005	f,g
$SiF_s + F_{d\,g} \rightarrow SiF_{2\,s}$	0.005	f, i
$SiF_{2\,s} + F_{d\,g} \rightarrow SiF_{3\,s}$	0.005	f, i
$SiF_{3\,s} + F_{d\,g} \rightarrow SiF_{4\,g}$	0.007	f, i, g
$SiO_2CF_p + F_g \rightarrow SiF_{2\,s} + CO_{2\,g}$	0.0001	f
$SiO_2CF_{2\,p} + F_g \rightarrow SiF_{3\,s} + CO_{2\,g}$	0.0001	f
$SiO_2CF^{*}{}_p + F_g \rightarrow SiF_{2\,s} + CO_{2\,g}$	0.0001	f

Table 7.1 (contd.)

$SiO_2CF_2{}^*{}_p + F_g \rightarrow SiF_{3\,s} + CO_{2\,g}$	0.0001	f
$SiO_2CF_p + F_{d\,g} \rightarrow SiF_{2\,s} + CO_{2\,g}$	0.005	f, i
$SiO_2CF_{2\,p} + F_{d\,g} \rightarrow SiF_{3\,s} + CO_{2\,g}$	0.005	f, i
$SiO_2CF^*{}_p + F_{d\,g} \rightarrow SiF_{2\,s} + CO_{2\,g}$	0.005	f, i
$SiO_2CF_2{}^*{}_p + F_{d\,g} \rightarrow SiF_{3\,s} + CO_{2\,g}$	0.005	f, i
$C_p + F_g \rightarrow CF_p$	0.0005	
$CF_p + F_g \rightarrow CF_{2\,p}$	0.0006	
$CF_{2\,p} + F_g \rightarrow CF_{3\,p}$	0.0005	
$CF_{3\,p} + F_g \rightarrow CF_{4\,g}$	0.0005	
$C^*{}_p + F_g \rightarrow CF_p$	0.0008	
$CF^*{}_p + F_g \rightarrow CF_{2\,p}$	0.0007	
$CF_2{}^*{}_p + F_g \rightarrow CF_{3\,p}$	0.0006	
$CF_3{}^*{}_p + F_g \rightarrow CF_{4\,g}$	0.0006	
Reactions at polymer surface		
$C_p + C_g \rightarrow C_p + C_p$	0.003	
$C^*{}_p + C_g \rightarrow C_p + C_p$	0.01	
$C_p + CF_g \rightarrow C_p + CF_p$	0.002	
$C^*{}_p + CF_g \rightarrow C_p + CF_p$	0.015	
$C_p + CF_{2\,g} \rightarrow C_p + CF_{2\,p}$	0.001	
$C^*{}_p + CF_{2\,g} \rightarrow C_p + CF_{2\,p}$	0.02	

Table 7.1 (contd.)

$C_p + CF_{3\,g} \rightarrow C_p + CF_{3\,p}$	0.001
$C^*_p + CF_{3\,g} \rightarrow C_p + CF_{3\,p}$	0.004
$C_p + C_2F_{3\,g} \rightarrow C_p + CF_p + CF_{2\,p}$	0.001
$C^*_p + C_2F_{3\,g} \rightarrow C_p + CF_p + CF_{2\,p}$	0.004
$C_p + C_2F_{4\,g} \rightarrow C_p + CF_{2\,p} + CF_{2\,p}$	0.001
$C^*_p + C_2F_{4\,g} \rightarrow C_p + CF_{2\,p} + CF_{2\,p}$	0.004
$C_p + C_2F_{5\,g} \rightarrow C_p + CF_{2\,p} + CF_{3\,p}$	0.001
$C^*_p + C_2F_{5\,g} \rightarrow C_p + CF_{2\,p} + CF_{3\,p}$	0.005
$CF_p + C_g \rightarrow CF_p + C_p$	0.004
$CF^*_p + C_g \rightarrow CF_p + C_p$	0.025
$CF_p + CF_g \rightarrow CF_p + CF_p$	0.003
$CF^*_p + CF_g \rightarrow CF_p + CF_p$	0.02
$CF_p + CF_{2\,g} \rightarrow CF_p + CF_{2\,p}$	0.002
$CF^*_p + CF_{2\,g} \rightarrow CF_p + CF_{2\,p}$	0.01
$CF_p + CF_{3\,g} \rightarrow CF_p + CF_{3\,p}$	0.001
$CF^*_p + CF_{3\,g} \rightarrow CF_p + CF_{3\,p}$	0.001
$CF_p + C_2F_{3\,g} \rightarrow CF_p + CF_p + CF_{2\,p}$	0.001
$CF^*_p + C_2F_{3\,g} \rightarrow CF_p + CF_p + CF_{2\,p}$	0.003
$CF_p + C_2F_{4\,g} \rightarrow CF_p + CF_{2\,p} + CF_{2\,p}$	0.001
$CF^*_p + C_2F_{4\,g} \rightarrow CF_p + CF_{2\,p} + CF_{2\,p}$	0.003

Table 7.1 (contd.)

$CF_p + C_2F_{5\,g} \rightarrow CF_p + CF_{2\,p} + CF_{3\,p}$	0.001
$CF^*_p + C_2F_{5\,g} \rightarrow CF_p + CF_{2\,p} + CF_{3\,p}$	0.003
$CF_{2\,p} + C_g \rightarrow CF_{2\,p} + C_p$	0.003
$CF_2^*{}_p + C_g \rightarrow CF_{2\,p} + C_p$	0.01
$CF_{2\,p} + CF_g \rightarrow CF_{2\,p} + CF_p$	0.001
$CF_2^*{}_p + CF_g \rightarrow CF_{2\,p} + CF_p$	0.01
$CF_{2\,p} + CF_{2\,g} \rightarrow CF_{2\,p} + CF_{2\,p}$	0.001
$CF_2^*{}_p + CF_{2\,g} \rightarrow CF_{2\,p} + CF_{2\,p}$	0.01
$CF_{2\,p} + CF_{3\,g} \rightarrow CF_{2\,p} + CF_{3\,p}$	0.001
$CF_2^*{}_p + CF_{3\,g} \rightarrow CF_{2\,p} + CF_{3\,p}$	0.004
$CF_{2\,p} + C_2F_{3\,g} \rightarrow CF_{2\,p} + CF_p + CF_{2\,p}$	0.001
$CF_2^*{}_p + C_2F_{3\,g} \rightarrow CF_{2\,p} + CF_p + CF_{2\,p}$	0.001
$CF_{2\,p} + C_2F_{4\,g} \rightarrow CF_{2\,p} + CF_{2\,p} + CF_{2\,p}$	0.001
$CF_2^*{}_p + C_2F_{4\,g} \rightarrow CF_{2\,p} + CF_{2\,p} + CF_{2\,p}$	0.001
$CF_{2\,p} + C_2F_{5\,g} \rightarrow CF_{2\,p} + CF_{2\,p} + CF_{3\,p}$	0.001
$CF_2^*{}_p + C_2F_{5\,g} \rightarrow CF_{2\,p} + CF_{2\,p} + CF_{3\,p}$	0.001
$CF_{3\,p} + C_g \rightarrow CF_{3\,p} + C_p$	0.001
$CF_3^*{}_p + C_g \rightarrow CF_{3\,p} + C_p$	0.002
$CF_{3\,p} + CF_g \rightarrow CF_{3\,p} + CF_p$	0.001
$CF_3^*{}_p + CF_g \rightarrow CF_{3\,p} + CF_p$	0.002

Table 7.1 (contd.)

$CF_{3\,p} + CF_{2\,g} \rightarrow CF_{3\,p} + CF_{2\,p}$	0.001	
$CF_3^*{}_{p} + CF_{2\,g} \rightarrow CF_{3\,p} + CF_{2\,p}$	0.002	
$CF_{3\,p} + CF_{3\,g} \rightarrow CF_{3\,p} + CF_{3\,p}$	0.001	
$CF_3^*{}_{p} + CF_{3\,g} \rightarrow CF_{3\,p} + CF_{3\,p}$	0.002	
$CF_{3\,p} + C_2F_{3\,g} \rightarrow CF_{3\,p} + CF_{p} + CF_{2\,p}$	0.0001	
$CF_3^*{}_{p} + C_2F_{3\,g} \rightarrow CF_{3\,p} + CF_{p} + CF_{2\,p}$	0.0005	
$CF_{3\,p} + C_2F_{4\,g} \rightarrow CF_{3\,p} + CF_{2\,p} + CF_{2\,p}$	0.0001	
$CF_3^*{}_{p} + C_2F_{4\,g} \rightarrow CF_{3\,p} + CF_{2\,p} + CF_{2\,p}$	0.0005	
$CF_{3\,p} + C_2F_{5\,g} \rightarrow CF_{3\,p} + CF_{2\,p} + CF_{3\,p}$	0.0001	
$CF_3^*{}_{p} + C_2F_{5\,g} \rightarrow CF_{3\,p} + CF_{2\,p} + CF_{3\,p}$	0.0005	
$C_{p} + CF_3^+{}_{g} / I^+{}_{g} \rightarrow CF_{3\,g} / I_{g} + C_{g}$	p_0=0.1	h, E_{th}=8
$CF_{p} + CF_3^+{}_{g} / I^+{}_{g} \rightarrow CF_{3\,g} / I_{g} + CF_{g}$	p_0=0.1	h, E_{th}=6
$CF_{2\,p} + CF_3^+{}_{g} / I^+{}_{g} \rightarrow CF_{3\,g} + CF_{2\,g} / I_{g}$	p_0=0.1	h, E_{th}=4
$CF_{3\,p} + CF_3^+{}_{g} / I^+{}_{g} \rightarrow CF_{3\,g} + CF_{3\,g} / I_{g}$	p_0=0.1	h, E_{th}=2
Ion-induced defluorination		
$CF_{p} + CF_3^+{}_{g} / I^+{}_{g} \rightarrow C_{p} + CF_{3\,g} / I_{g} + F_{g}$	p_0=0.1	h, E_{th}=2
$CF_{2\,p} + CF_3^+{}_{g} / I^+{}_{g} \rightarrow CF_{p} + CF_{3\,g} / I_{g} + F_{g}$	p_0=0.1	h, E_{th}=2
$CF_{3\,p} + CF_3^+{}_{g} / I^+{}_{g} \rightarrow CF_{2\,p} + CF_{3\,g} / I_{g} + F_{g}$	p_0=0.1	h, E_{th}=2
$CF_{p} + CF_3^+{}_{g} / I^+{}_{g} \rightarrow C_{p} + CF_{3\,g} / I_{g} + F_{d\,g}$	p_0=0.1	h, i, E_{th}=2
$CF_{2\,p} + CF_3^+{}_{g} / I^+{}_{g} \rightarrow CF_{p} + CF_{3\,g} / I_{g} + F_{d\,g}$	p_0=0.1	h, i, E_{th}=2

Table 7.1 (contd.)

$CF_{3\,p} + CF_3{}^+{}_g / I^+{}_g \rightarrow CF_{2\,p} + CF_{3\,g} / I_g + F_{d\,g}$	p_0=0.1	h, i, E_{th}=2
Photon-induced defluorination		
$CF_p + h\nu \rightarrow C_p + F_{d\,g}$	P_{phot}=0.1	i, j, Eth=11 eV
$CF_{2\,p} + h\nu \rightarrow CF_p + F_{d\,g}$	P_{phot}=0.1	i, j, Eth=11 eV
$CF_{3\,p} + h\nu \rightarrow CF_{2\,p} + F_{d\,g}$	P_{phot}=0.1	i, j, Eth=11 eV

Notes:

a. Unless otherwise specified, all ions neutralize on all surfaces, returning as their neutral counterparts.

b. The sum of probabilities of gas phase species with surface sites shown here may not sum to unity. The remaining probability is assigned to the incident species reflecting without reaction.

c. All gas phase species have units of flux ($cm^{-2}s^{-1}$). All surface species have units of fractional coverage. All polymer species have units of monolayers. Polymer reactions are normalized by the thickness of the polymer. Derivatives for surface species are divided by the surface site density N_s (=10^{15} cm^{-2}).

d. See Eq. 7.6. $\nu = 5 \times 10^3$.

e. See Eq. 7.9.

f. See Eq. 7.8.

g. Wafer Etch step.

h. See Eq. 7.4. E_r=50 eV, E_{th}=5 eV, unless specified. All energies are in eV.

i. These reactions are for Model B (as described in the text).

j. These reactions are for UV photon effects, and are only used in Chapter 9.

7.6 Figures

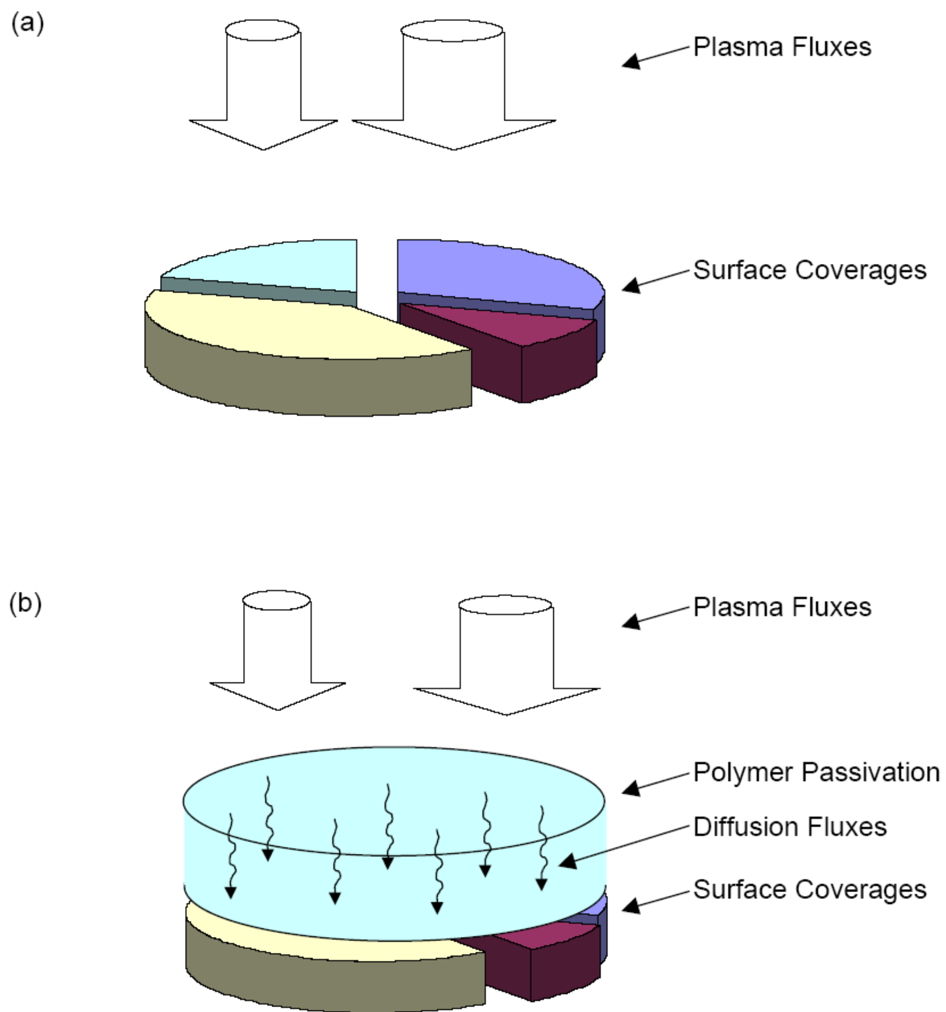

Figure 7.1. Schematic of the (a) conventional site balance model and (b) the Surface Kinetics Model.[12]

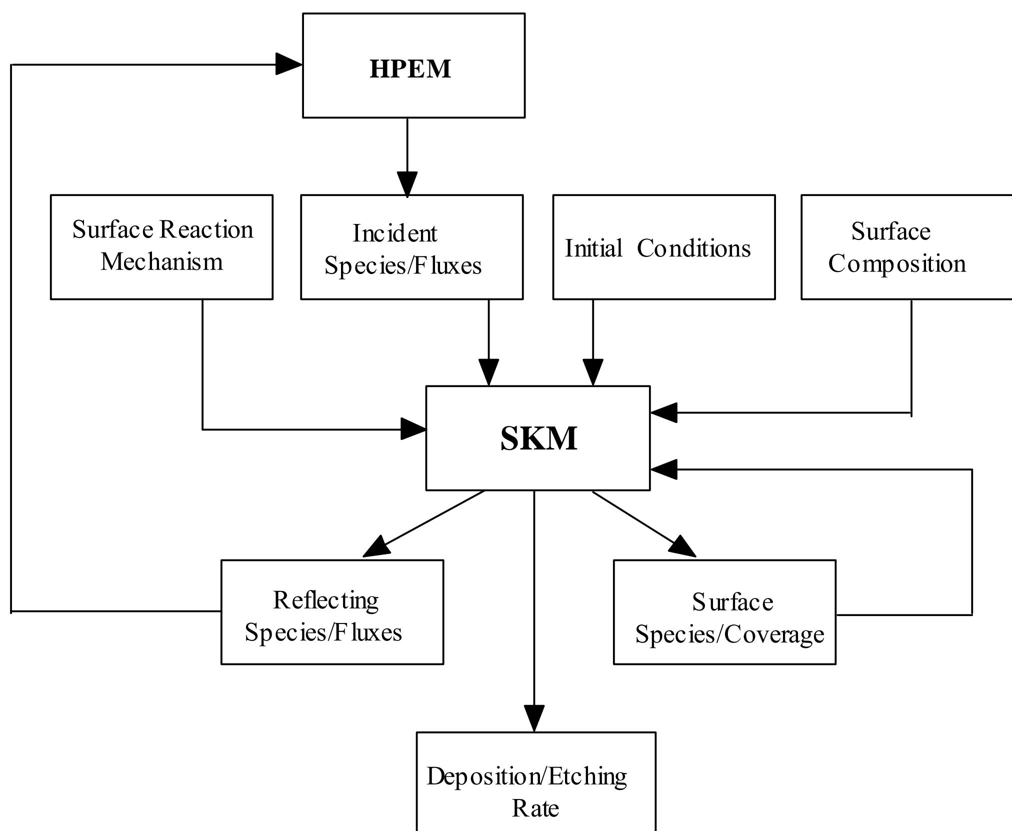

Fig. 7.2. Flow diagram of the integrated plasma-surface model.

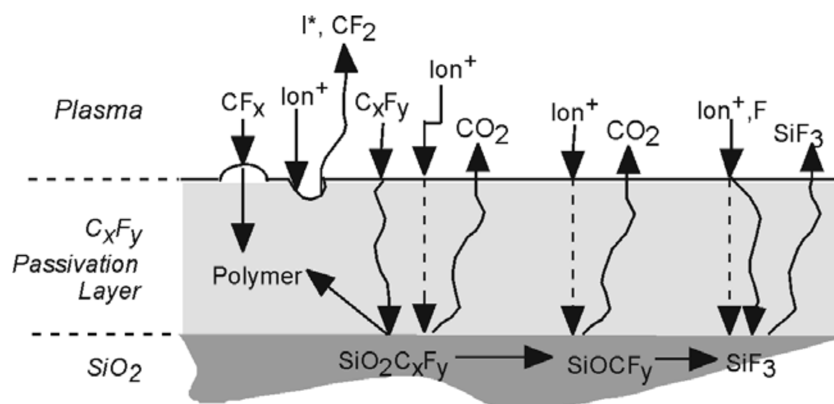

Fig. 7.3. Schematic of surface reaction mechanism for SiO2. The dashed lines represent energy transfer through the polymer.

7.7 References

1. J. T. C. Lee, N. Layadi, K. V. Guinn, H. L. Maynard, F. P. Klemens, D. E. Ibbotson, I. Tepermeister, P. O Egan, and R. A. Richardson, J. Vac. Sci. Technol. B **14**, 2510 (1996).
2. B. E. E. Kastenmeier, P. J. Matsuo, G. S. Oehrlein, and J. G. Langan, J. Vac. Sci. Technol. A **16**, 2047 (1998).
3. K. Nishikawa, T. Oomori, and K. Ono, J. Vac. Sci. Technol. B **17**, 127 (1999).
4. M. Schaepkens, R. C. M. Bosch, T. E. F. M. Standaert, and G. S. Oehrlein, J. Vac. Sci. Technol. A **16**, 2099 (1998).
5. T. E. F. M. Standaert, M. Schaepkens, N. R. Rueger, P. G. M. Sebel, G. S. Oehrlein, and J. M. Cook, J. Vac. Sci. Technol. A **16**, 239 (1998).
6. N. R. Rueger, J. J. Beulens, M. Schaepkens, M. F. Doemling, J. M. Mirza, T. E. F. M. Standaert, and G. S. Oehrlein, J. Vac. Sci. Technol. A **15**, 1881 (1997).
7. W. Z. Collison, T. Q. Ni, and M. S. Barnes, J. Vac. Sci. Technol. A **16**, 100 (1998).
8. N. Mantzaris, A. Boudovis, and E. Gogolides, J. Appl. Phys. **77**, 6169 (1995).
9. E. Meeks, R. S. Larson, S. R. Vosen, and J. W. Shon, J. Electrochem. Soc. **144**, 357 (1997).
10. B. A. Helmer and D. B. Graves, J. Vac. Sci. Technol. A **16**, 3502 (1998).
11. D. E. Hanson, A. F. Voter, and J. D. Kress, J. Appl. Phys. **86**, 2263 (1999).
12. D. Zhang and M. J. Kushner, J. Vac. Sci. Technol. A **19**, 524 (2001).
13. C. F. Abrams and D. B. Graves, J. Appl. Phys. **86**, 2263 (1999).
14. K. Teii, M. Hori, and T. Goto, J. Appl. Phys. **87**, 7185 (2000).

15. M. Schaepkens, T. E. F. M. Standaert, N. R. Rueger, P. G. M. Sebel, G. S. Oehlein, and J. M. Cook, J. Vac. Sci. Technol. A **17**, 26 (1999).

16. M. Inayoshi, M. Ito, M. Hori, and T. Goto, J. Vac. Sci. Technol. A **16**, 233 (1998).

17. T. E. F. M. Standaert, C. Hedlund, E. A. Joseph, G. S. Oehrlein, and T. J. Dalton, J. Vac. Sci. Technol. A **22**, 53 (2004).

18. G. S. Oehrlein and J. F. Rembetski, IBM J. Res. Develop. **36**, 140 (1992).

8. POLYMER FILMS IN FLUOROCARBON ETCHING PLASMAS

8.1 Introduction

The motivation for studying a polymer-resolved plasma deposition mechanism has been explained in Chapter 6. In this chapter, the results from interfacing the Surface Kinetics Model (Chapter 7) with a two-dimensional plasma equipment model (HPEM, Chapter 3), will be discussed here. Results from the SKM as used for plasmas sustained in C_4F_8 and C_2F_6 plasmas at a few mTorr with a substrate bias are discussed in Sections 8.2 and 8.3. Section 8.4 contains the conclusion to this section.

8.2 C_4F_8 Plasmas

8.2.1 Base Case Plasma Parameters

The plasma etching reactor shown in Fig. 8.1 is an inductively coupled plasma (ICP) reactor patterned after the apparatus used by Standaert *et al.*[8] Inductive power is supplied through a three-turn coil, 16 cm in diameter. The coil sits on a 2 cm thick quartz window which is 23 cm in diameter. The wafer is on a substrate 7 cm below the quartz window and can be independently biased. The process conditions used in this study were 10 mTorr and 50 sccm flow rate of C_4F_8. The coil is at 13.56 Mhz and delivers an inductive power of 1400 W.

Power deposition is restricted to near the antenna and is within the skin depth of the electromagnetic field, which is a few cm. The high power and large electron density ($\approx 10^{11}$ cm^{-3}) highly dissociates the feed gas, whose density peaks near the input nozzle. The electron density is large in these plasmas ($\approx 10^{11}$ cm^{-3}) and there is a large degree of

dissociation of the C_4F_8. The C_4F_8 is dissociated into C_2F_4 which is further dissociated into smaller CF_2, and other small molecules. The dominant ions are CF_3^+, CF_2^+, and F^+. At the low pressures of operation, the density profile is determined primarily by diffusion processes. Ambipolar fields lead to large rates of recombination of CF_2^+ at the walls, causing an increase in CF_2 density increases near the walls of the reactor.

Radical and ion fluxes to the wafer for the base case conditions are shown in Fig. 8.2. Lower F atom and ion fluxes may result in a thicker passivation layer near the edge of the wafer. In contrast, decreasing neutral radical fluxes result in lowered deposition at the edges. The net result of these two effects is that the etch rates near the edge of the wafer were slightly lower than those at the center. The fluxes are relatively uniform, showing a minor dropoff in the ion fluxes to the edge of the wafer.

8.2.2 SiO_2 Etch Rates and Polymer Film Properties

To assess the importance of the fluorine released through the ion-induced defluorination in the polymer (Table 7.I), the following study was performed. For the first set of cases, the fluorine released because of ion impact was assumed to have the same effect as fluorine produced by gas phase reactions (Model A). This assumption is made because the surface model is well-mixed and the polymer is assumed to be spatially uniform. In the absence of quantifying the gradient of film composition with height, the point of release of the fluorine in the polymer is not known. As a result, the model treats this fluorine diffusing through the layer same as fluorine from the plasma. This model underpredicts the etch rates of SiO_2 (Fig. 8.3a), especially at lower biases, where the fluorine channel for etching SiO_2 is more important than the direct ion etching. In the

second set of cases (Model B), the fluorine released due to ion impact is assumed to be a different species (F_d), which has a higher rate of reaction with the substrate. This higher rate is intended to reflect the shorter distance that the fluorine from the ion-induced defluorination has to traverse to reach the substrate. The etch rates predicted by Model B are in closer agreement to the experimental results, as shown in Fig. 8.3a. The ion impact produced fluorine is important in the etching at higher biases as well, which implies that the ion-induced defluorination process competes with the direct ion etching at high biases. In principle, the rate of reaction of gaseous fluorine with the substrate sites in Model A could have been assigned a higher rate. This would, however, shift the dependence of the etch process from ion impact to bulk gas phase processes. For example, a higher inductive power in the plasma would lead to increased dissociation of fluorocarbons into fluorine and carbon, and this increased density of F atoms would lead to an overestimated etch rate, while the fluorine dissociated from the film remains the same.

The thickness of the polymer film predicted from experiment and predicted by the model (Model B) are compared in Fig. 8.3(b). The experimental results show a minimum thickness of 0.7 nm (around a monolayer). The model underpredicts the minimum thickness, and the results are of sub-monolayer thickness. This result should be interpreted as there being sites with no coverage and sites with a monolayer coverage, which on average over the whole wafer surface, is less than a monolayer. The compositional dependence with self-bias voltage is in Fig. 8.4(a). The percentage contribution of C_p increases with self-bias, because of the defluorination of CF_p and CF_{2p}. The percentage contribution of $CF_{3\ p}$ does not appreciably change. The bonding of $CF_{3\ g}$

radicals to the surface is sterically hindered, due to the larger size of the molecule. The removal of a $CF_{3\,p}$ site is easy because the bond to the surface is weaker than for a $CF_{2\,p}$ site. The amount of $CF_{3\,p}$ is therefore a result of balance between deposition and removal of the CF_{3g} radicals. The percentage contribution of CF_p also does not change appreciably because the density of CF_p sites is a result of the balance between defluorination of $CF_{2\,p}$ sites (to form CF_p) and defluorination of CF_p sites to form C_p. As the ion energy increases, both of these processes increase equally, causing only a very slight increase in the CF_p percentage contribution to the polymer. This trend in composition is also seen in experiment. Standaert et al have measured the XPS spectra at varying self-bias voltages and see an increasing contribution of C_p as compared to $CF_{2\,p}$.[8]

8.2.3 Ion-induced Defluorination

The extent of defluorination of the film has been measured by Standaert et al. They define the amount of defluorination as the difference in the fluorine content (F/C ratio) of a film deposited at zero substrate bias, and the F/C ratio of the steady state polymer film being studied. The F/C ratio is defined as

$$F/C = \frac{\sum_{i=1}^{3} iA(C-F_i)}{A(C-Si)+A(C-C)+\sum_{i=1}^{3} A(C-F_i)} \qquad (8.1)$$

where A(…) is the area of the fitted Gaussian function for each constituent. In our study, we replace A(…) by the density of monolayers of each species. The defluorination is

plotted against the SiO_2 etch rate in Fig. 8.4(b). The etch rate is found to be linearly dependent on the defluorination at all values of self-bias. This leads us to believe that ion-induced defluorination is a significant process for SiO_2 etching, even in the regimes for direct ion etching.

8.2.4 Parameterizations

The surface reaction mechanism parameters should be independent of the actual plasma properties, if all of the possible species interactions with the surface have been accounted for. This allows us the freedom of changing the bulk plasma gas chemistry and process conditions without having to reevaluate the mechanism at each run. (For example, at a power of 1400 W, C and F are the dominant neutrals, while at 200 W, there is negligible amount of C). Having a complete reaction set may slow down the calculation, but this cost is negligible in our computational infrastructure.

The surface model developed was used to parameterize the power deposition in the plasma. The results are shown in Fig. 8.5 for polymer thickness and composition. The evolution of the surface depends on neutral sticking as well as ion reactions. At low powers, the C_4F_8 is not fragmented enough to form precursors, and the film is very thin. The film in this regime is composed of roughly equal CF_p, CF_{2p}, and CF_{3p} sites. As power increases, the C_4F_8 fragments into C_2F_4, which is a precursor on the surface. The C_2F_4, in principle, may deposit as a powder, and not incorporate into the polymer film, but for the purpose of this study, we assume that the C_2F_4 radical deposits as two CF_{2p} sites. As a result of this deposition, the percentage contribution of CF_{2p} is very large at lower powers, and thick films are formed

As power increases further, the ionization increases, and the flux of ions to the surface increases. This ionization leads to some defluorination, increasing the percentage of CF_p and C_p. The increase in CF_p is also due to the fragmentation of CF_2 and C_2F_3 in the gas phase. However, over the whole power range, since the dominant pathways for breakdown involve C_2F_4 and CF_2, the film composition is predominantly CF_{2p}. The increased ion sputtering results in a dropoff in film thickness as well. At even higher powers, the feed fluorocarbon gas is increasingly broken down into fluorine, which has a very high chemical etching property, which leads to thinner films.

8.3 Polymer Film Properties in C_2F_6 Plasmas

The same surface reaction mechanism was applied to the study of C_2F_6 plasmas. The operating conditions were the same as for the C_4F_8 plasmas. The pathways for bulk phase reactions are different in these plasmas. The primary radical at 1400 W power is CF_3, not CF_2, as shown in the fluxes in Fig. 8.6. The SiO_2 etch rates and the fluorocarbon film thickness are shown in Fig. 8.7, as a function of substrate bias. The etch rates are higher than in the case of C_4F_8 plasmas, and this may be because of the increased F/C ratio in a CF_3-dominated plasma. Once again, the thickness is underpredicted by our model at high biases, due to the possibility of having sub-monolayer thicknesses in the model.

The composition of these films produced in C_2F_6 plasmas with a change in substrate bias is shown in Fig. 8.8. Due to the prevalence of CF_{3g}, the contribution of CF_{3p} to the film is larger than in the case of C_4F_8 plasmas. However, as the self-bias increases, the CF_{3p} percentage drops because of the loose binding of CF_{3p} to the film,

which can easily be removed by ion impact. Defluorination also plays an important role in this case, which causes the densities of CF_{2p} to increase at first, and then decrease, as the rate of defluorination of CF_{2p} to CF_p increases. However, when the defluorination (Eqn. 8.1) is plotted against etch rate, the trend is not exactly linear as it was for C_4F_8 plasmas, as seen in Fig. 8.8. We conclude that ion-induced defluorination is the dominant etch-causing process, only if the CF_{xp} radicals are well incorporated in the film. When processes such as ion sputtering of CF_{3p} come into play, the relationship of etch to ion-induced defluorination no longer holds.

The effect of power deposition on film thickness and composition are shown in Fig. 8.9. The film thickness follows the same trends as in a C_4F_8 plasma, but the thickness of the polymer for C_2F_6 plasmas is lesser. This is because of ion sputtering of CF_{3p}, as well as the reduced deposition probability of radicals to CF_{3p} sites. At higher powers, the fluorination is the dominant process, leading to extremely thin films. The composition of the films shows a very appreciable reduction in the CF_{3p} contribution. This is primarily due to fluorination of the CF_{3p} to CF_{4g} , and the ion impact to form CF_{2p}.

8.4 Summary

In conclusion, the passivation layer formed during SiO_2 etching in a fluorocarbon plasma has been resolved at a meso-scale level and interfaced with a two-dimensional plasma equipment model. The state of fluorination of the carbon sites in the polymers are differentiated. This is necessary to understand the relation of the stiochiometric composition of the polymer film to the SiO_2 etch rate, and to evaluate the importance of ion-induced defluorination of the polymer layer. For plasma conditions that result in

precursors that bind strongly to the polymer film, the ion-induced defluorination is the dominant etch process, even for film thicknesses of < 1 nm. This is validated by the almost linear dependence of SiO_2 etch rates on the amount of defluorination. For plasmas (like C_2F_6), the precursors are loosely bound to the film, and are easily removed by ion sputtering as well as fluorine etching. In these cases, the ion-induced defluorination is no longer the primary process for SiO_2 etching.

8.5 Figures

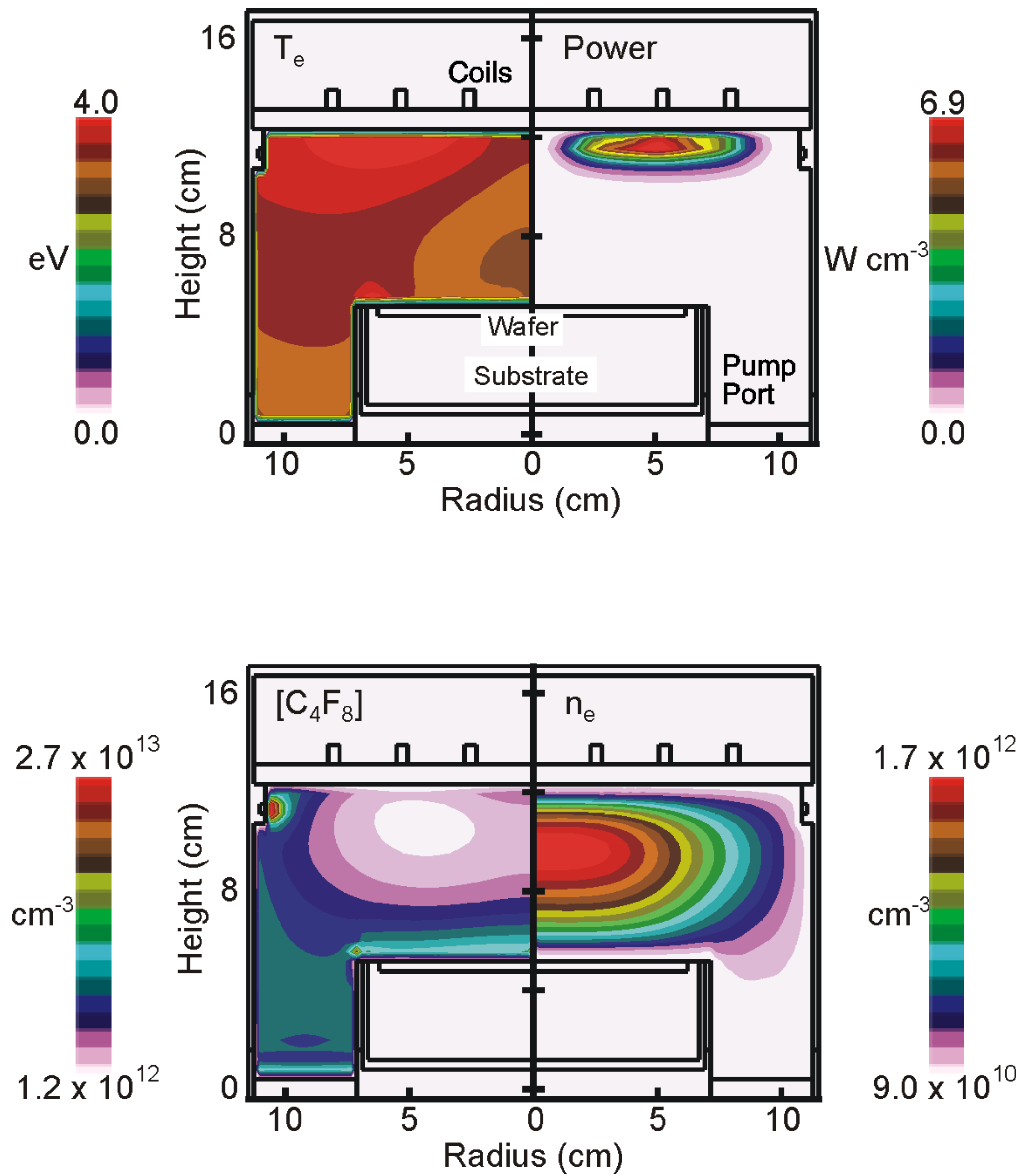

Figure 8.1. Schematic of the ICP reactor and densities of major species, for the base case conditions of 10 mTorr, 100% C_4F_8, 50 sccm, 1400 W ICP power.

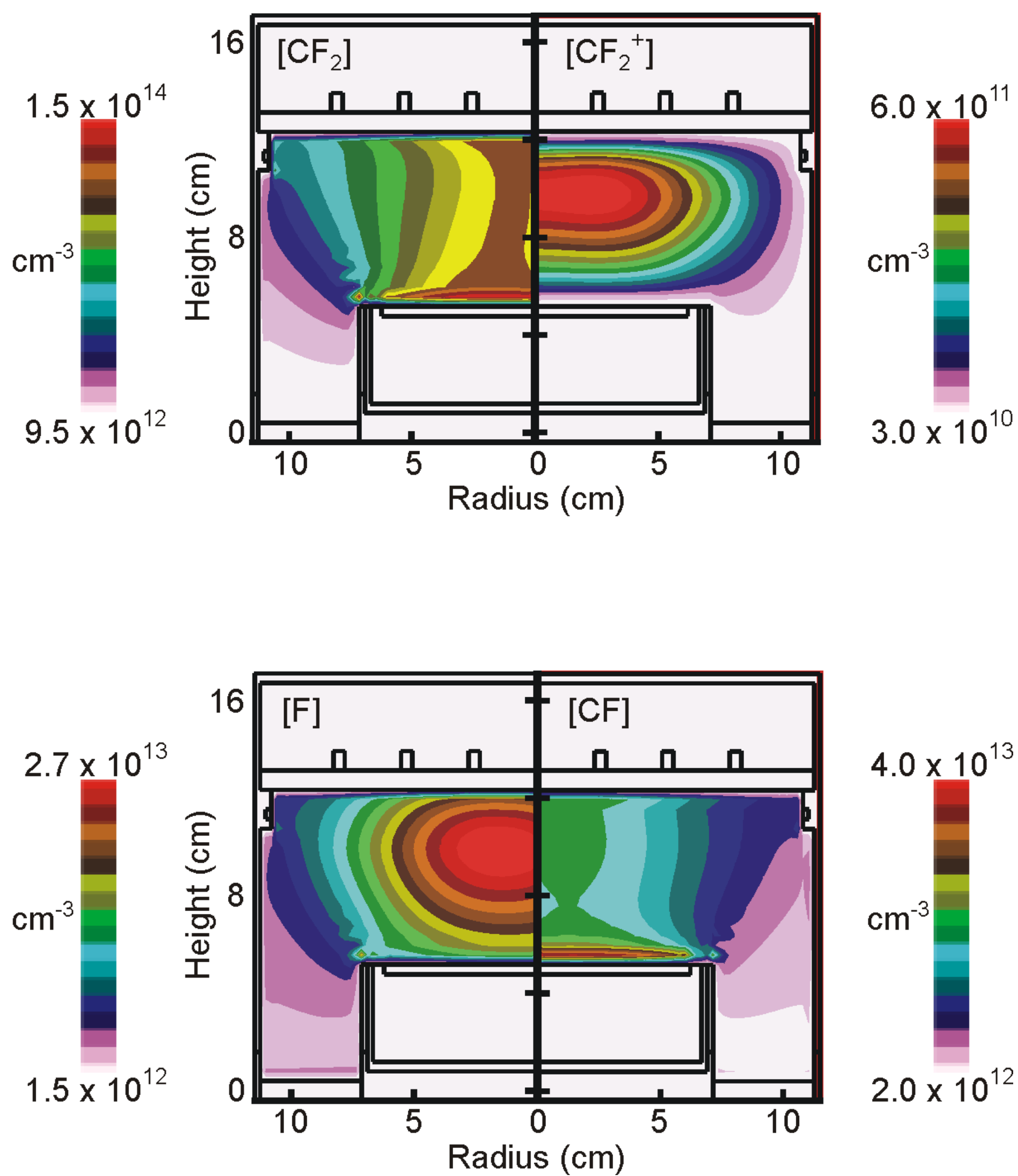

Figure 8.1. (contd.) Schematic of the ICP reactor and densities of major species, for the base case conditions of 10 mTorr, 100% C_4F_8, 50 sccm, 1400 W ICP power.

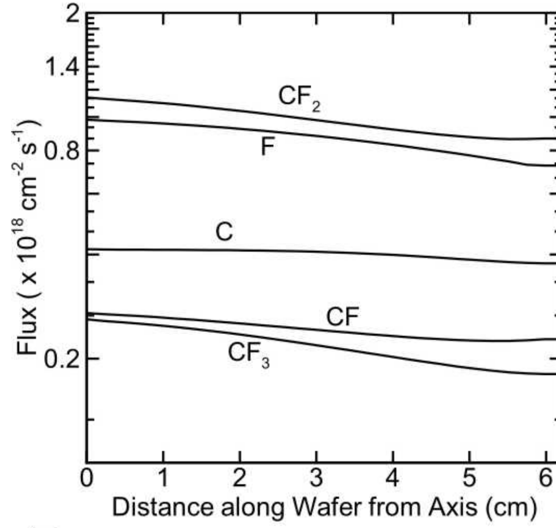

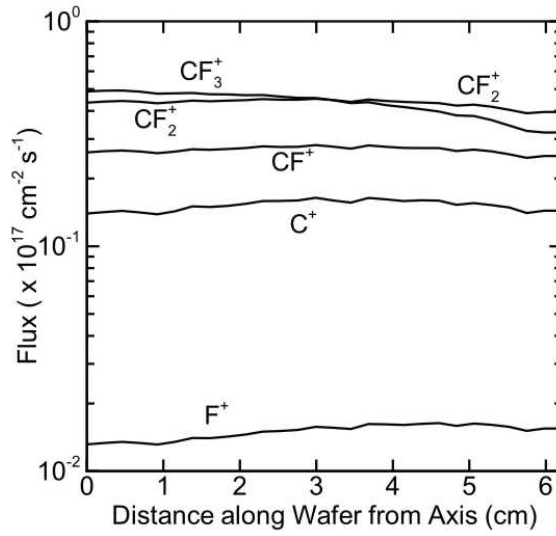

Figure 8.2. Fluxes to the wafer as a function of radius for the base case. (a) Fluxes of CF_2, CF_3 CF, C, and F. (b) Fluxes of CF_2^+, CF_3^+ CF^+, C^+, and F^+.

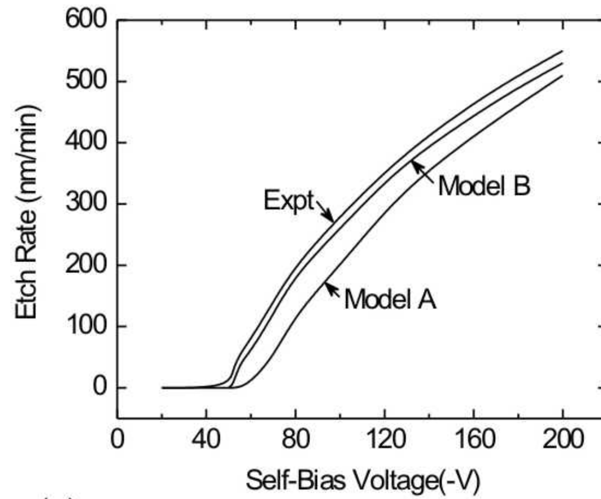

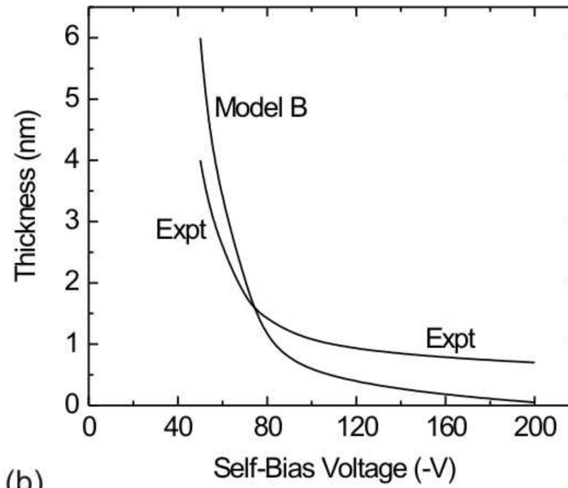

Figure 8.3. Variation of etch rates and thickness with self-bias voltage. (a) Etch rates for experiment [8], and two simulation models. Model B accounts for the enhanced etch due to ion-induced defluorination. (b) Thickness of film with self-bias for experiment and Model B. At higher biases > 100 V, there is only a monolayer of thickness.

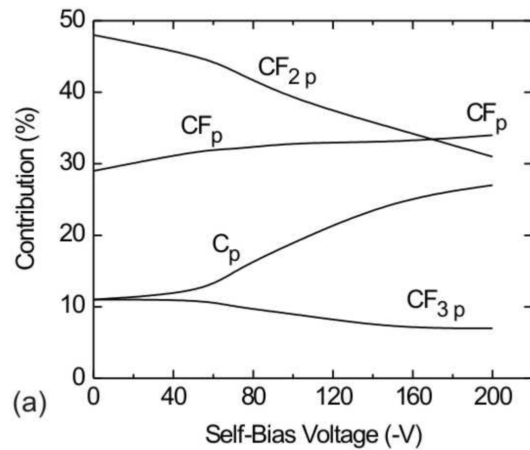

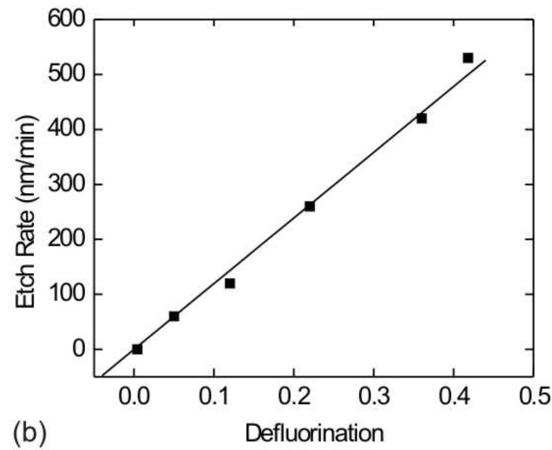

Figure 8.4. Variation of composition with self-bias voltage. (a) Composition of the CF_{xp} sites, showing a sharp dropoff in the CF_{2p} percentage, balanced by an increase in C_p. This is due to ion-induced defluorination. (b) Etch rates versus defluorination, as defined by Eqn 7. The etch rates show a linear trend with defluorination, showing that even at high biases and low film thicknesses, the dominant etch process is defluorination.

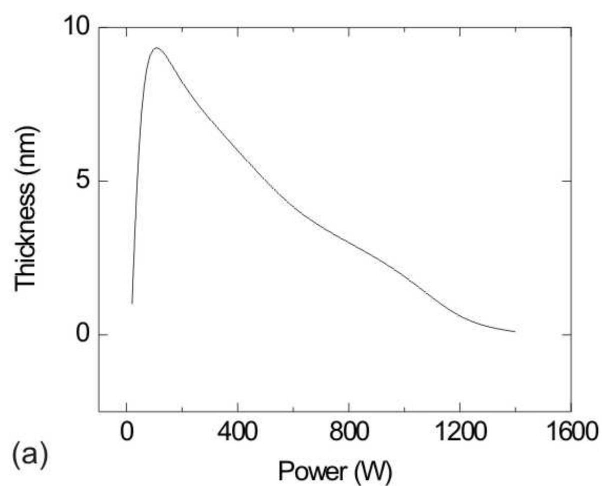

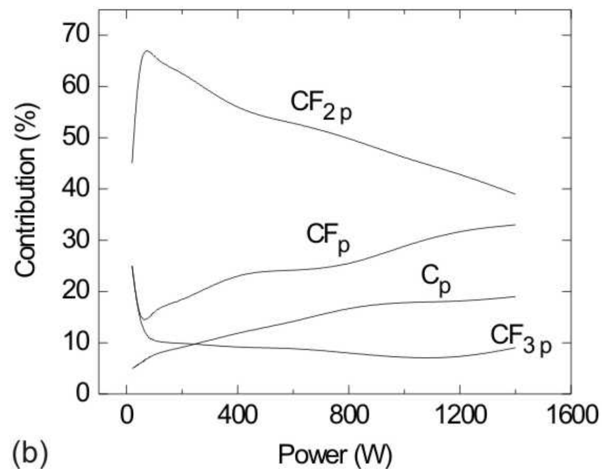

Figure 8.5. Variation of film properties with ICP power. (a) Film thickness shows a sharp rise with the increase in depositing precursors, and then exhibits a drop-off as ion sputtering and defluorination take place at higher dissociations of the feed gas. (b) Composition of the film. At lower powers, the composition reflects the pathways for gas-phase radical production. At higher powers, increase gas-phase dissociation, fluorination and ion-induced defluorination leads to an increase in CF_p.

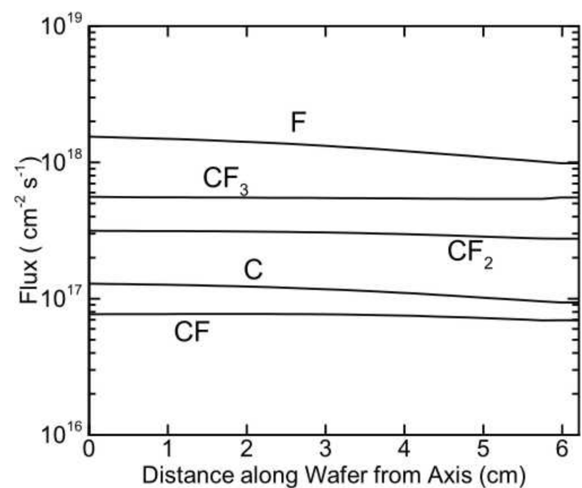

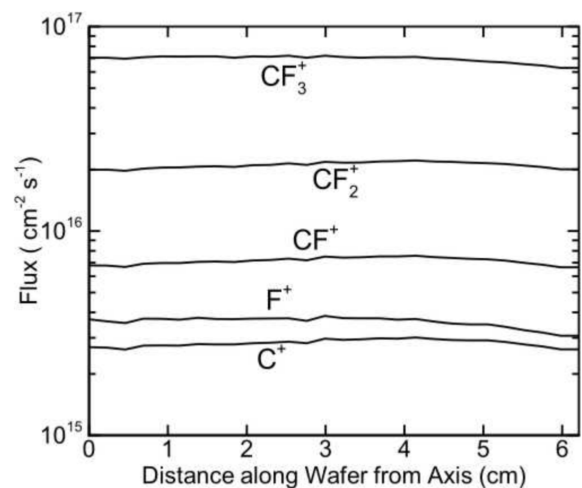

Figure 8.6. Fluxes to the wafer as a function of radius for a C_2F_6 plasma for the base case of 50 sccm, 1400 W ICP Power and 10 mTorr, (a) Fluxes of CF_2, CF_3 , CF, C, and F. (b) Fluxes of CF_2^+, CF_3^+ CF^+, C^+, and F^+. For this plasma, the CF_3 radicals are the most dominant.

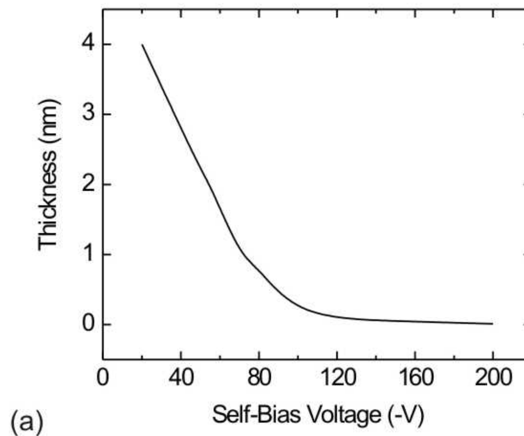

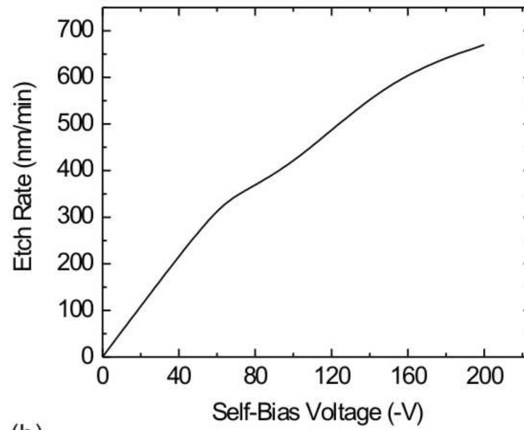

Figure 8.7. Variation of etch rates and thickness with self-bias voltage for a C_2F_6 plasma. (a)) Thickness of film with self-bias. At higher biases > 100 V, there is only a monolayer of thickness. (b) Etch rates. The etch rates are higher than for a C_4F_8 plasma.

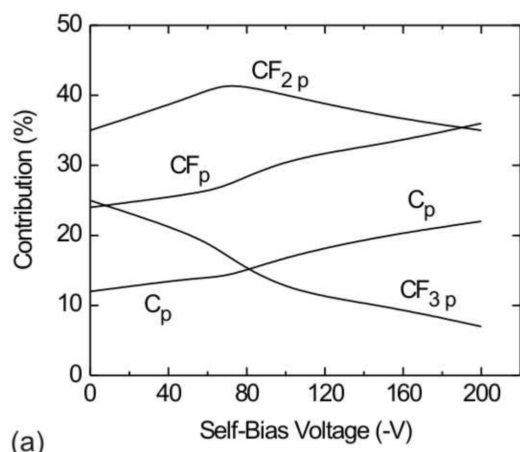

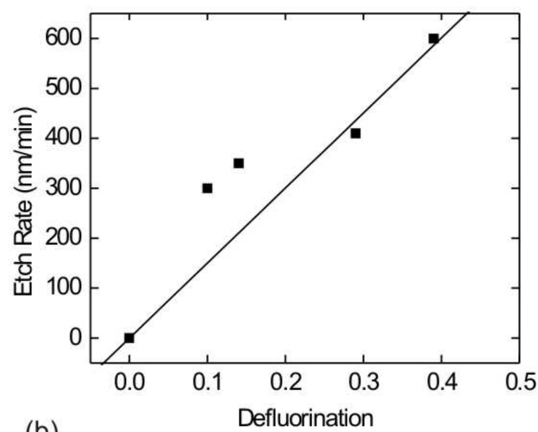

Figure 8.8. Variation of composition with self-bias voltage for a C_2F_6 plasma.. (a) Composition of the CF_{xp} sites, showing a sharp dropoff in the CF_{3p} percentage, balanced by an increase in C_p. This is due to ion-induced defluorination and ion sputtering of CF_{3p}. (b) Etch rates versus defluorination, as defined by Eqn 7. The etch rates do not show a linear trend with defluorination, showing that for films that are not well-incorporated, the dominant etch process is not necessarily defluorination.

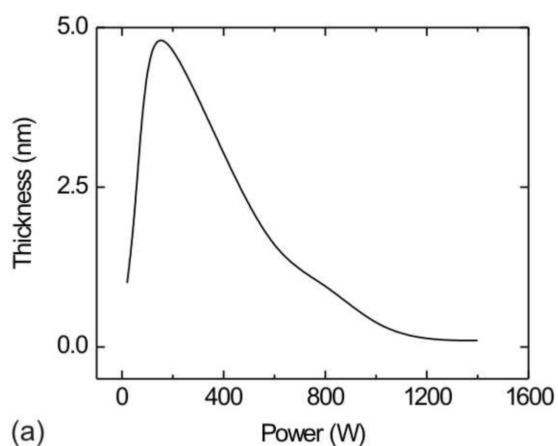

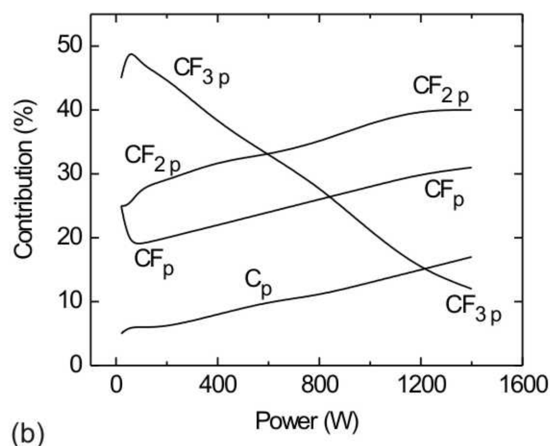

Figure 8.9. Variation of film properties with ICP power. (a) Film thickness shows a sharp rise with the increase in depositing precursors, and then exhibits a drop-off as ion sputtering and defluorination take place at higher dissociations of the feed gas. The film thicknesses are lower than for a C_4F_8 plasma due to steric factors. (b) Composition of the film. At lower powers, the composition reflects the pathways for gas-phase radical production. At higher powers, increase gas-phase dissociation, fluorination and ion-induced defluorination leads to an increase in CF_p, and a sharp dropoff in CF_{3p}.

8.6 References

1. T. C. Lee, N. Layadi, K. V. Guinn, H. L. Maynard, F. P. Klemens, D. E. Ibbotson, I. Tepermeister, P. O Egan, and R. A. Richardson, J. Vac. Sci. Technol. B **14**, 2510 (1996).
2. B. E. E. Kastenmeier, P. J. Matsuo, G. S. Oehrlein, and J. G. Langan, J. Vac. Sci. Technol. A **16**, 2047 (1998).
3. K. Nishikawa, T. Oomori, and K. Ono, J. Vac. Sci. Technol. B **17**, 127 (1999).
4. M. Schaepkens, R. C. M. Bosch, T. E. F. M. Standaert, and G. S. Oehrlein, J. Vac. Sci. Technol. A **16**, 2099 (1998).
5. T. E. F. M. Standaert, M. Schaepkens, N. R. Rueger, P. G. M. Sebel, G. S. Oehrlein, and J. M. Cook, J. Vac. Sci. Technol. A **16**, 239 (1998).
6. N. R. Rueger, J. J. Beulens, M. Schaepkens, M. F. Doemling, J. M. Mirza, T. E. F. M. Standaert, and G. S. Oehrlein, J. Vac. Sci. Technol. A **15**, 1881 (1997).
7. W. Z. Collison, T. Q. Ni, and M. S. Barnes, J. Vac. Sci. Technol. A **16**, 100 (1998).
8. N. Mantzaris, A. Boudovis, and E. Gogolides, J. Appl. Phys. **77**, 6169 (1995).
9. E. Meeks, R. S. Larson, S. R. Vosen, and J. W. Shon, J. Electrochem. Soc. **144**, 357 (1997).
10. B. A. Helmer and D. B. Graves, J. Vac. Sci. Technol. A **16**, 3502 (1998).
11. D. E. Hanson, A. F. Voter, and J. D. Kress, J. Appl. Phys. **86**, 2263 (1999).
12. D. Zhang and M. J. Kushner, J. Vac. Sci. Technol. A **19**, 524 (2001).

13. C. F. Abrams and D. B. Graves, J. Appl. Phys. **86**, 2263 (1999).

14. M. J. Grapperhaus and M. J. Kushner, J. Appl. Phys.**81**, 569 (1997).

15. T. E. F. M. Standaert, C. Hedlund, E. A. Joseph, G. S. Oehrlein, and T. J. Dalton, J. Vac. Sci. Technol. A **22**, 53 (2004).

9. ETCHING IN C_4F_8 / ARGON PLASMAS : EFFECT OF UV RADIATION

9.1 Introduction

In the previous chapters, the motivation for studying surface reaction mechanisms for plasma etch processes has been discussed. In Chapter 8, the fluorine released from the film due to ion impact was seen to be the most important channel for etching in C_4F_8 plasmas. In this chapter, we focus on fluorocarbon plasmas containing Ar, which produces UV radiation which may affect the etch process due to photon-induced surface processes.

Argon is added to fluorocarbon mixtures to increase the effect of ion bombardment relative to reactive ion etching. Extensive experimental studies have been performed on these fluorocarbon/Ar mixtures.[1,2] It is found that increasing the fraction of Ar leads to a decrease in the CF and CF_2 radicals, which in turns leads to control over selectivity. Another application of Ar is its use for diagnostics in fluorocarbon plasmas, when introduced in traces.[3] In both of these applications, Ar is excited by electron impact and produces resonance radiative transitions from the excited to ground states. The resonance radiation may be absorbed and re-emitted many times in the plasma during its transit from the initial sites of emission to exiting the plasma, similar to the photons emitted by Hg in the lamps discussed in Chapters 4 and 5. This radiation trapping may take place if the partial pressure of the rare gas is appreciable (> 1 mTorr)

The UV radiation is known to participate in processes that damage the wafer during processing.[4] However, few studies have been done of the influence of the UV radiation on the polymer film. Due to energetic UV photons striking the film, there may

be bond-rearrangement, bond straining and bond-breaking processes. This may modify the process significantly, depending on the extent of the modification. Enhanced crosslinking due to UV photons may result in enhanced (or depressed) rate in polymer growth processes. Stress and strain on bonds may lead to morphological rearrangements which affect the transport of ions through the film, as well as the surface interactions of bulk plasma and surface species.

In this article, we shall consider the effects of UV photon bombardment on defluorination. For example, bond-breaking of CF_{xp} sites in the polymer film may release fluorine that diffuses through the film to the surface, enhancing etch rate. This would illustrate the importance of UV photons in the SiO_2 etch process. While crosslinking may be the dominant process affected by UV photons, we use this work as a proof-of-principle study.

In this chapter, we study the effects of radiation transport on the etching processes in the reactor. The Monte Carlo Radiation Transport Model (MCRTM, Chapter 4), and the mesoscale surface model (SKM, Chapter 7) are interfaced with a two-dimensional hybrid plasma equipment model (HPEM). Section 9.2 contains the changes to the surface reaction mechanism used in Chapter 8. Section 9.3 contains the results for radiation trapping in C_4F_8/Ar mixtures, and the results for the effect of radiation transport on etching in these mixtures is disccused in Section 9.4.

9.2 UV Photon Surface Reactions

The surface reaction mechanism has been detailed in Chapter 7. In this study, we add the following reactions to the mechanism. (Table 7.1, Photon-induced defluorination)

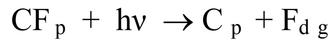

$$CF_{p} + h\nu \rightarrow C_{p} + F_{d\,g}$$

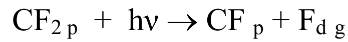

$$CF_{2\,p} + h\nu \rightarrow CF_{p} + F_{d\,g}$$

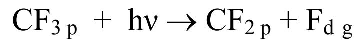

$$CF_{3\,p} + h\nu \rightarrow CF_{2\,p} + F_{d\,g}$$

where the p subscript refers to polymer sites, and g to gaseous phase radicals. The above reactions take place with a probability p_{phot} (=0.1). $F_{d\,g}$ refers to fluorine in the gaseous phase, which is released within the polymer layer, and was described in Chapter 8. Ion-impact processes typically take place within the first few monolayers of the polymer film, which means that they can be considered, for all practical purposes, as polymer-surface processes. Photons can penetrate the polymer layer, and cause defluorination anywhere in the layer, and are therefore, bulk processes.

To ascertain the rates for the above reactions, the photon fluxes are needed. This flux is computed by the following method. The statistics for the exit UV flux are collected on each surface mesh point. The frequency corresponding to the threshold energy for the reactions is calculated, and the flux spectra above this energy is integrated to provide the flux of photons having energy greater than the threshold.

The $Ar(^1P_1)$ to $Ar(^1S_0)$ transition occurs with a linecenter wavelength of 105 nm, and a vacuum radiative lifetime of 1.96 ns. The fluorocarbon gases do not emit in the UV region, and are therefore not considered for the purposes of radiation influence.

9.3 Radiation Trapping in C_4F_8/Ar Plasmas

The etching reactor shown in Fig 9.1 has been described in Chapter 8. The process conditions were 1400 W ICP power, 10 mTorr, and 50 sccm flow rate of feed gas mixture (C_4F_8/Ar). Due to the high power and electron density, the feed gases are efficiently fragmented and ionized, and the dominant ions are Ar^+, CF_2^+, and F^+. The radiative species, $Ar(^1P_1)$ is primarily on axis. This is because the Ar ($^1P_1$) is formed by electron impact excitation from the ground state, so the region of maximum $Ar(^1P_1)$ is determined by the region of high electron density as well as high [Ar]. This predominantly occurs on axis.

The trapping factors are shown with an increase in Ar additive, along with exit spectra for resonance radiation from $Ar(^1P_1)$ to $Ar(^1S_0)$ in Fig. 9.2. When keeping the power constant, the density of emitters (excited states) is approximately constant, while the [Ar $^1S_0$] increases. The trapping factors are seen to increase almost linearly with the Ar fraction, in Figure 9.2(a). Three exit spectra are shown at varying fractions of Ar. At higher opacities of Ar, the photons near line-center are absorbed and re-emitted muiltiple times. After each such absorption and re-emission, the photon frequency is shifted towards the wings of the lineshape until the photon mean free path is sufficiently large for the photon to exit the plasma. This causes the phenomenon of line-reversal, due to which the spectra show a dip near line center and a maximum in the wings of the profile. At 1% Ar, there is negligible trapping, and the spectrum exhibits no line-reversal. At 30% Ar and 90% Ar, the trapping is much more pronounced. Radiation trapping, therefore, is an important process in low-pressure plasmas, and should be a consideration for better understanding the plasma processes.

As substrate bias increases, the trapping factors decrease. (Fig. 9.3b) This is because the radiative state Ar($^1P_1$) being in closer proximity to the walls with increasing power. The substrate bias provides an additional source of power to the plasma. With an increase in power deposition in the plasma, there is more ionization and excitation of Ar $^1S_0$. However, this power is coupled capacitively to the plasma, unlike the power deposited by the coils. The power deposition by the substrate is directly related to the magnitude of the electric field. Due to the geometric nature of capacitive coupling, and neglecting edge effects, the electric field lines are normal to the substrate. Hence, the power deposition by the substrate is predominantly in a cylindrical region with radius equal to the radius of the substrate.

With a lower substrate bias (Fig. 9.1), the maximum Ar ionization is in a region close to the axis. However, due to the excess power deposition in a larger radius, the region of ionization extends radially. This is shown in Fig. 9.3a. This increased ionization leads to a higher electron density, which in turn leads to increased excitation of the Ar($^1S_0$) state. Thus, with an increase in substrate bias, the number of excited states increases, as does their proximity to the walls. This leads to the decrease in trapping factors. by around 10-15% over a self-bias from 0 to 200 V.

As substrate bias increases, the field near the wafer increases, and there is more ion flux to the wafer. These ions return from the surface as their neutral counterparts, and this increases the density of ground states near the wafer. This increased density near the walls, in principle, should increase the trapping factor because the photons have to traverse a larger column density of absorbers. However, the majority of the photon emitting Ar($^1P_1$) states are distant enough from the walls that this increase in column density does not make an appreciable difference. In addition to this, the number of Ar ions is around three or four

orders of magnitude less than that of the Ar($^1S_0$). Thus, the neutralization of ions at the walls does not cause a significant increase in column density near the walls to affect the trapping factors meaningfully.

The effect of flow on radiation transport was also considered in this study. Due to the disparate time scales of radiation transport (100s of nanoseconds) and the residence time (10s of milliseconds), the flow rate is not expected to change the radiation trapping factors significantly. This is indeed the case, as seen in Fig. 9.4.

9.4 Etch Rates in C_4F_8/Ar Plasmas

The etch rate falls sharply with an increase in added Ar. (Fig. 9.5) This is related to the fluorine content in the polymer film. As the percentage of Ar in the plasma increases, the ion density increases. This is because Ar ions have a negligible ion-electron recombination cross-section. The fluorocarbon ions are electronegative and recombine with electrons rapidly. This implies that the ion density in the plasma increases with increased Ar additive. The ion bombardment of the polymer substrate, therefore, increases, causing defluorination, which leads to an etch. Oehrlein et al have studied the effects of adding Ar at 600 W power.[5] In this regime, the polymer layer is defluorinated, leading to a lot of strongly bound C_p in the film, which also leads to thick films. As the films become thicker, the ion-induced defluorination is the only process causing etch, while the direct ion etch decreases. This leads to a drop in the etch rate at large (> 60%) Ar additive. At the powers of operation we study here, there is a lot of fluorine in the plasma, and this leads to thinner films. We also find a significant number density of C_g, which deposits as C_p. Thus, the fluorine content in the film is reduced, and the etch rate decreases.

The effect of UV radiation on the the etch rate is also shown in Fig. 9.5b. There are two offsetting processes in this case. As the percentage of Ar in the plasma increases, the photon flux increases, which releases more $F_{d\ g}$ from the film. However, the amount of fluorine in the film is reduced due to the lack of precursors, reducing the $F_{d\ g}$ that can be released. Thus, for lower concentrations of Ar, the photon flux causes a small increase in the etch rate. The difference between etch rates computed with and without the UV effects reduce as % Ar in the plasma is increased. The maximum difference in etch rate is around 5%.

The reduction in depositing radicals with increase in Ar fraction, and increased ion sputtering leads to a sharp fall in thickness of the polymer film (Fig. 9.6a). The relative importance of Ar ion-induced defluorination increases with an increased percentage of Ar, causing an increase in C_p sites. The photon reactions are relatively unimportant in this case, as shown by the etch rates. The composition of the film with UV effects included is nearly the same as that without UV.

The photon-induced defluorination probability parameter p_{phot} is user-defined, and it is therefore necessary, to perform a sensitivity analysis to examine the variation of the results with changes in p_{phot}. Results for this analysis are shown in Fig. 9.7. We found that the etch rates are not affected considerably by the photon defluorination parameter. At p_{phot}=1, all the photons participate in defluorination reactions. However, even in this extreme case scenario, the etch rate is increased by a maximum factor of around 10%. This is due to the fact that at high substrate biases, the energetics of the ion-induced processes result in the rates photon processes being lesser than ion-induced processes by at least an order of magnitude. In addition, the amount of fluorine in the film determines the sensitivity of the etch rate to

photon-induced defluorination. At high % Ar, there is almost no fluorine in the film, and so the change in p_{phot} does not result in a significant difference in etch rates. At intermediate Ar additives, the sensitivity of etch rate to p_{phot} is around 10%. Thus, we can conclude that, at the etching plasma conditions we have studied, the dependence of the etch rate on the photon defluorination parameter is relatively unimportant.

At a fixed Ar percentage of 50% Ar, the substrate bias was varied from 0 to 200 V. (Fig. 9.8) Due to increased ion-induced defluorination, the etch rate increases with bias. In this case, the photon flux does not vary much with substrate bias.(Fig 9.8b) The photon flux is a function of the $Ar(^1P_1)$ and Ar densities and spatial distributions, which depend only on bulk plasma properties to zero order. The increase in self-bias causes an increase in excited state density, as explained earlier. This change causes the flux to change by a factor of 3 from bias 0 V to bias 200 V. However, the magnitude of photon-induced defluorination reduces in comparison to ion-induced defluorination and direct-ion etch processes. Both these factors together result in the etch rate predicted by the model (UV included) being larger than the etch rate without UV by a constant amount.

The film thickness drops sharply with substrate bias, similar to the case in Chapter 8. The trends of change of composition of the film with self-bias are similar to those seen in pure C_4F_8 plasmas, as shown in Fig. 9.9. Ion-induced defluorination causes the amount of CF_{2p} to fall,and the percentage contribution of C_p to increase significantly. Once again, the photon flux causes a relatively insignificant change to the composition of the film.

9.5 Summary

In this chapter, the effects of UV radiation on SiO_2 etching in C_4F_8/Ar plasmas were discussed. This was done by interfacing both the MCRTM and the SKM with the HPEM. It is seen that radiation transport for the Ar line is important in parameter regimes where the partial pressure of Ar > 1 mTorr. The etch rates decrease with increasing Ar, due to the change in precursor density in the plasma. The photon flux causes the etch rate to increase by only a few percent due to photon-induced defluorination, even though it is a bulk process. This is because of the low thickness of the film and low fluorine content, as well as the relative importance of photon-induced and ion-induced reactions. While this was only a proof-of-principle study, more experimental data would allow us to validate our mechanism for photon processes, and we could increase the role of UV to processes such as crosslinking,

9.6 Figures

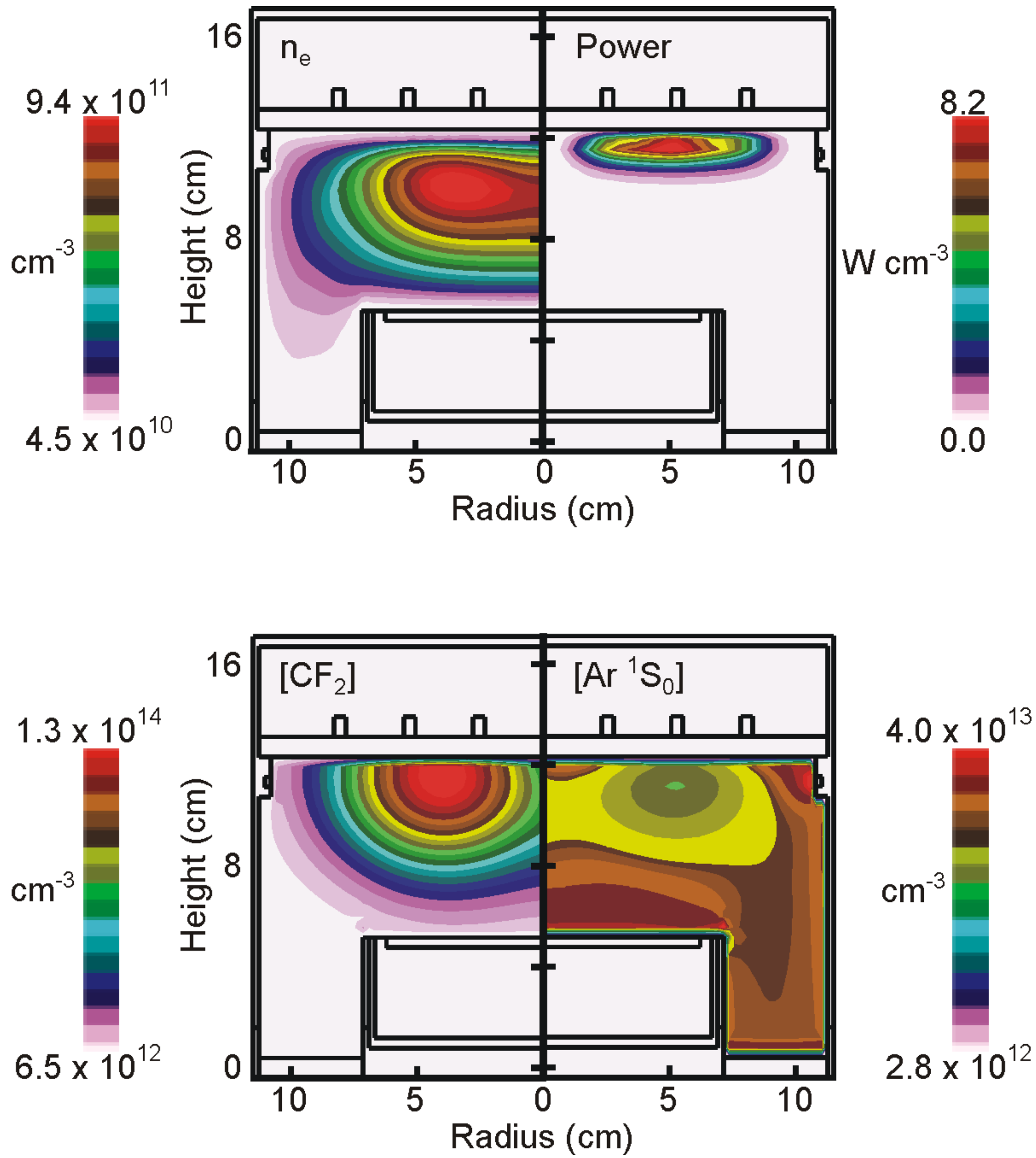

Figure 9.1. Plasma Parameters for C_4F_8/Ar plasma. The conditions are: Pressure 10mTorr, ICP Power 1400 W, Substrate Bias 100 V, 50% Ar/50% C_4F_8, and 40 sccm. The reactor geometry is same as that in Fig. 8.2.

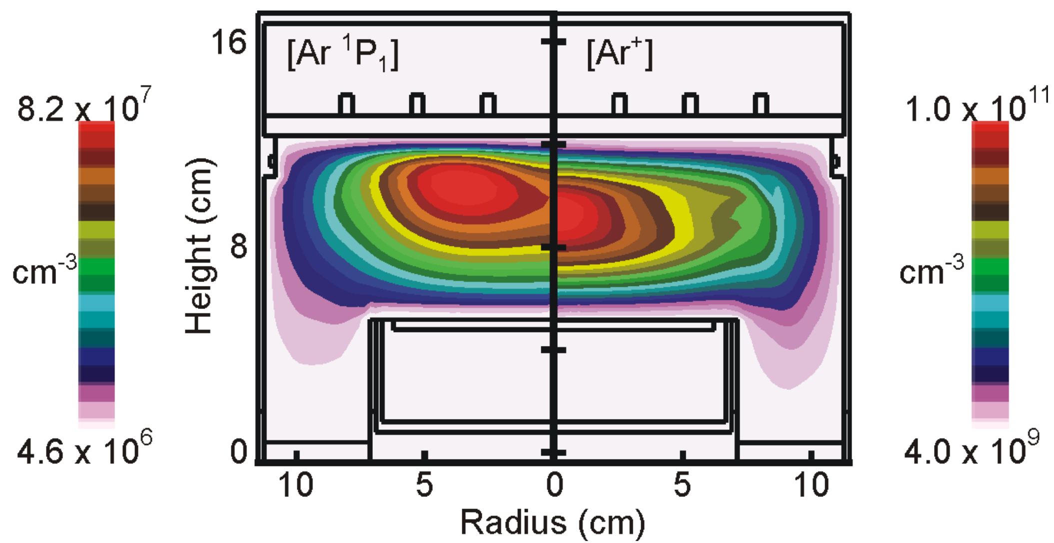

Figure 9.1. (contd) Plasma Parameters for C_4F_8/Ar plasma. The conditions are: Pressure 10mTorr, ICP Power 1400 W, Substrate Bias 100 V, 50% Ar/50% C_4F_8, and 40 sccm. The reactor geometry is same as that in Fig. 8.2.

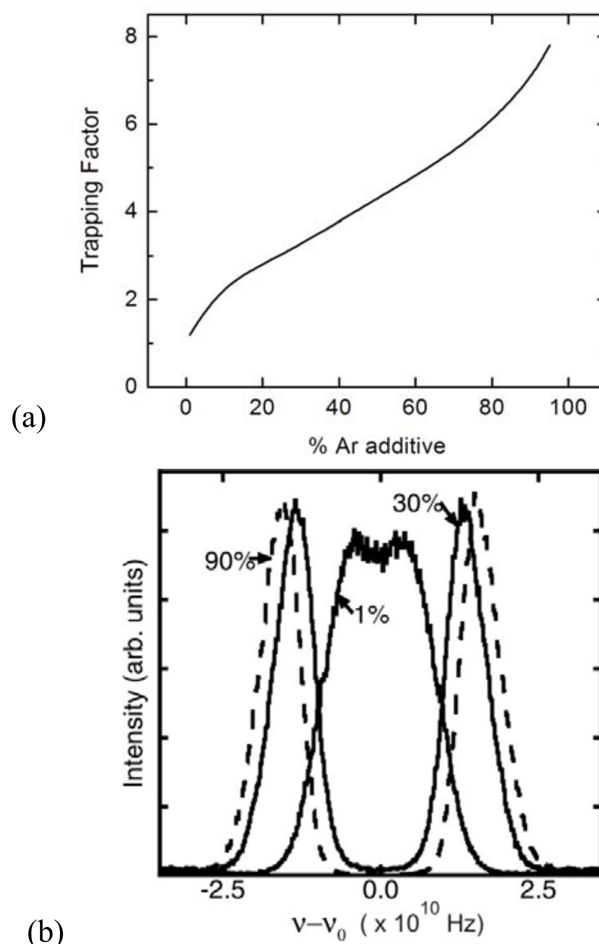

Figure 9.2 Trapping factors with increase in Ar additive. (a) Trapping factors increase with Ar additive, due to more ground state absorber density. (b) Exit spectra for 1%, 30%, and 90% Ar. At Ar partial pressures > 1 mTorr, trapping becomes important.

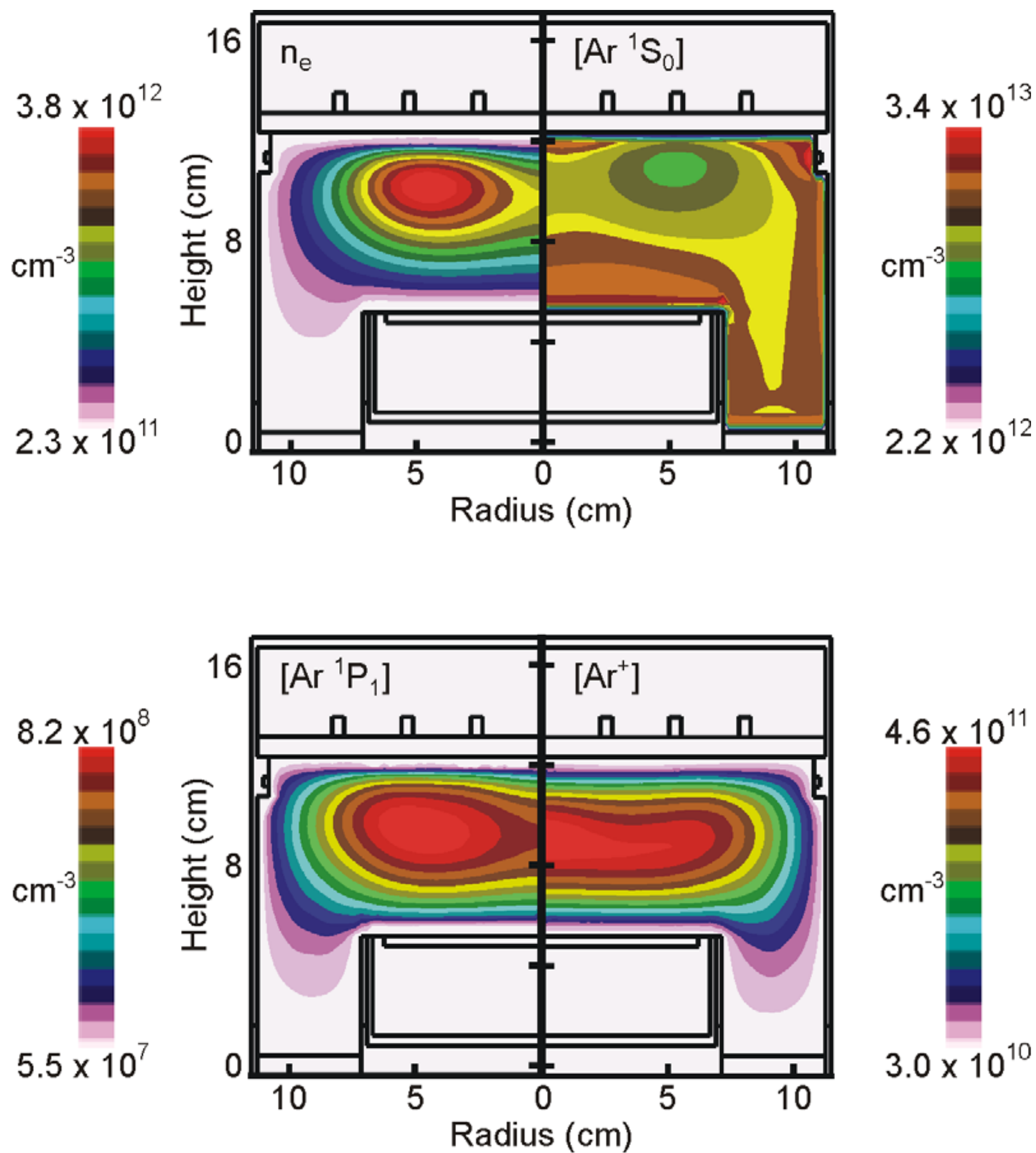

Figure 9.3(a). The effect of increased substrate bias on species densities. This is at substrate bias of 200 V, Pressure 10mTorr, ICP Power 1400 W, 50% Ar/50% C_4F_8, and 40 sccm. Comparing with Fig. 9.1, we find an extended region for Ar ionization due to the capacitive power coupling from the substrate.

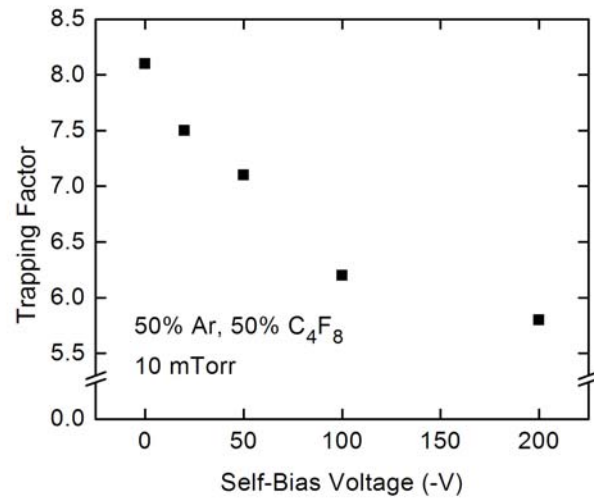

(b)

Figure 9.3(b) Trapping Factors with Substrate Bias. The geometrical effects of substrate coupling result in emitter density profiles closer to walls, leading a decrease din trapping factors.

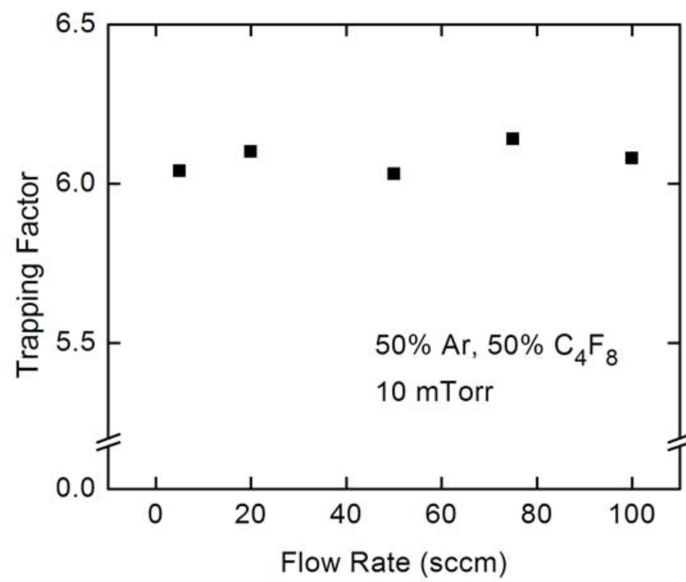

Figure 9.4 Trapping Factors with Flow Rate. Due to short timescales for radiation transport, the trapping is not affected by the flow.

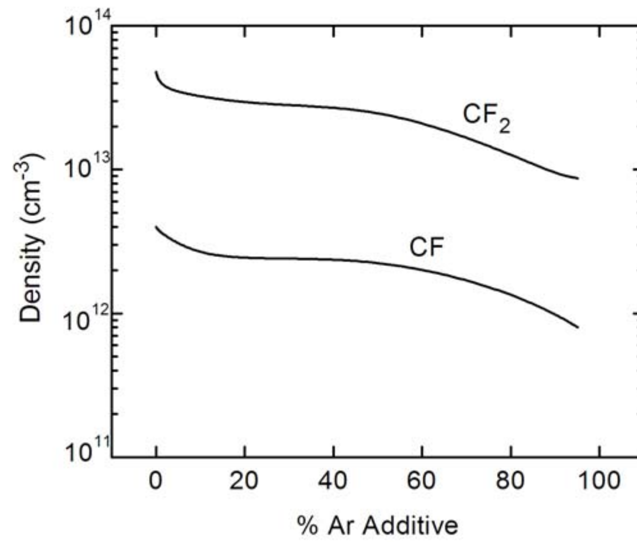

(a)

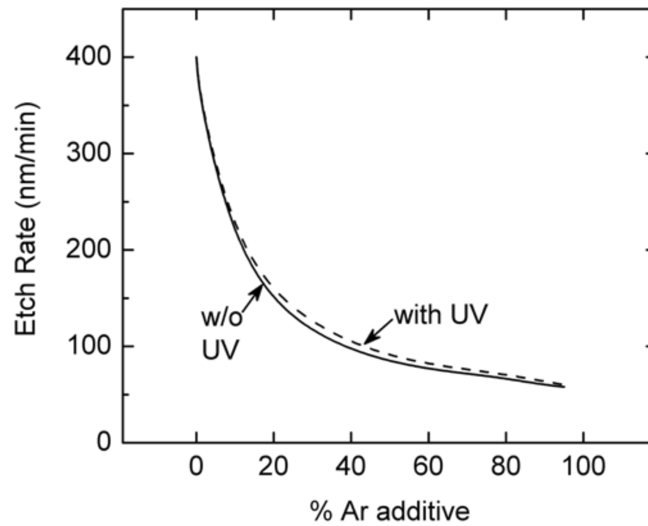

(b)

Figure 9.5 Etch Rate as a function of Ar additive. (a) The density of precursor radicals falls with an increase in Ar, leading to less fluorine in the film. (b) Due to decreased fluorine, the etch rates drop. The photon flux increases the etch rate due to photon-induced defluorination.

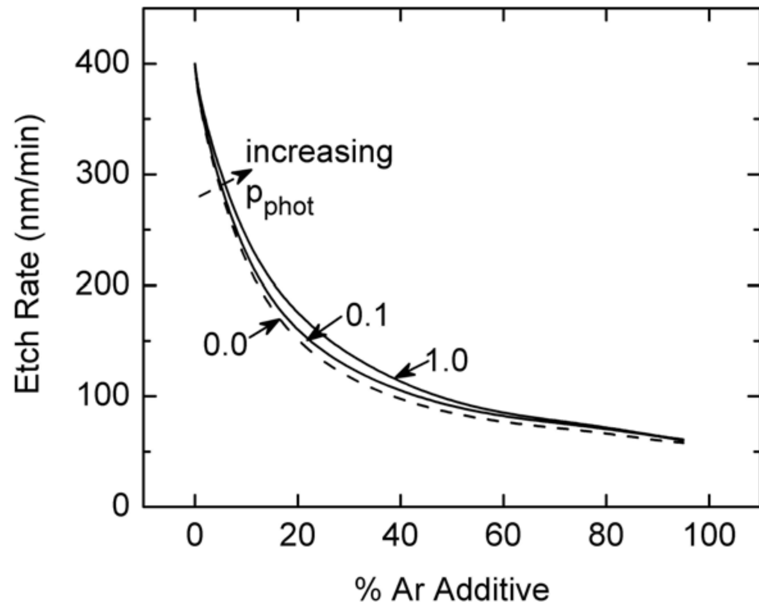

Figure 9.6 Etch Rate as a function of Ar additive and p_{phot}. The sensitivity of the model to photon defluorination depends on the amount of fluorine in the film.

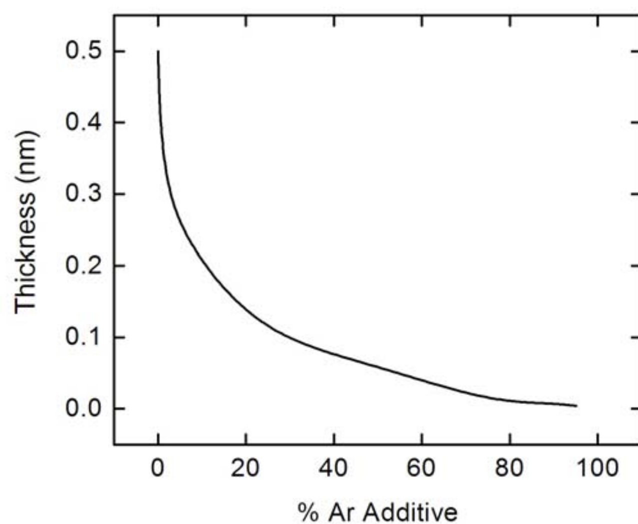

(a)

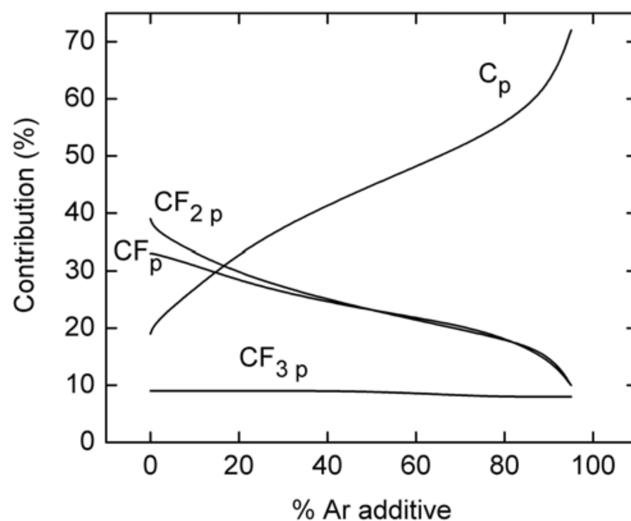

(b)

Figure 9.6. Film properties as a function of Ar additive for 100 V substrate bias. (a) The thickness of the film decreases with increase in Ar additive, due to the reduction in precursor radicals. (b) The composition of the film with % Ar additive. The amount of bare C_p increases due to a relative increase in Ar ion-induced defluorination.

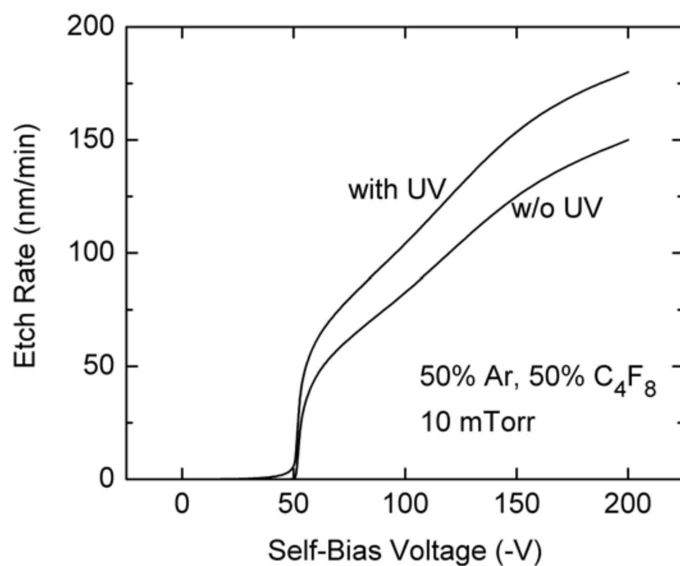

(a)

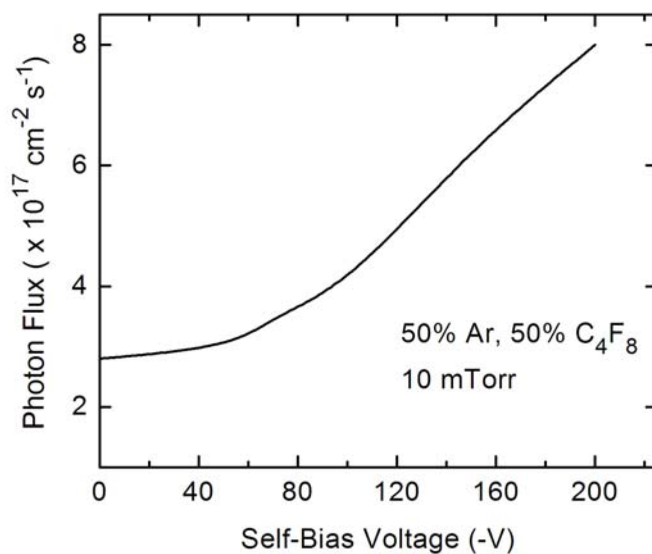

(b)

Figure 9.8 Etch rates as a function of substrate bias. (a) The etch rates increase with substrate bias because of enhanced ion-induced defluorination. (b) The photon flux to the substrate increases with a rise in substrate bias, due to an increase in $Ar(^1P_1)$ density. The enhanced photon flux leads to an increase in etch rates with self-bias.

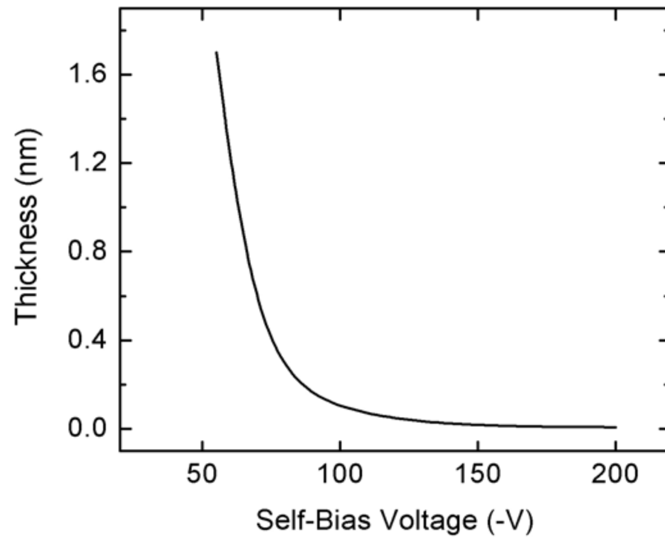

(a)

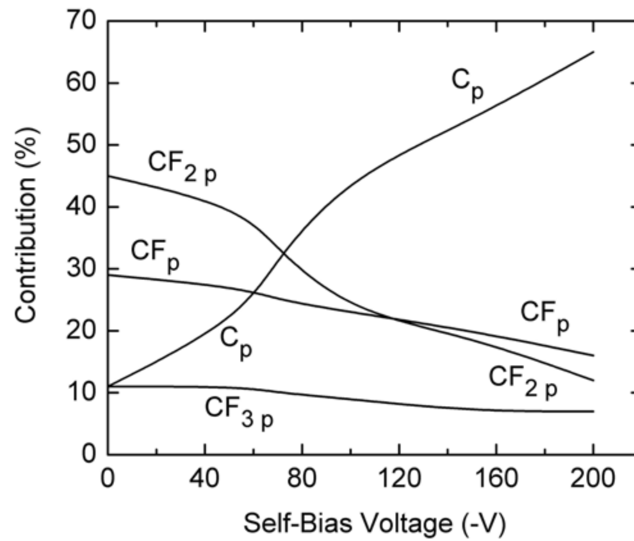

(b)

Figure 9.9 Film properties as a function of substrate bias for 50% Ar. (a) The thickness of the film decreases with increase in substrate bias, with ion sputtering. (b) The composition of the film with substrate bias. Bare Cp increases due to a relative increase in Ar ion-induced defluorination.

9.7 References

1. T. E. F. M. Standaert, M. Schaepkens, N. R. Rueger, P. G. M. Sebel, G. S. Oehrlein, and J. M. Cook, J. Vac. Sci. Technol. A **16**, 239 (1998).
2. C J Choi, O S Kwon, Y S Seol, Y W Kim, and I H Choi, J. Vac. Sci. Technol. B **18**, 811 (2000).
3. M. J. Schabel, V. M. Donnelly, A. Kornblit, and W. W. Tai, J. Vac. Sci. Technol. A **20**, 555 (2002).
4. J. J. Lauer, J. L. Shohet, and R. W. Hansen, J. Vac. Sci. Technol. A **21**, 1253 (2003).
5. X. Li, X. Ha, L. Ling, G. S. Oehrlein, M. Barela, and H. M. Anderson, J. Vac. Sci. Technol. A **20**, 2052 (2002).

10. CONCLUSIONS AND FUTURE EXTENSIONS

10.1 Conclusions

As wafer sizes decrease, and selectivity requirements for etch processes become more critical, fine control of the substrate etch process becomes more important. To this end, the surface reactions occurring at the surface of the wafer need to be understood completely. However, the mechanisms for these surface reactions are not yet known in their entirety, especially the influence of UV radiation on wafer damage and the etching process. This is increasingly important because UV radiation is now used in processing ultra low-k dielectrics ($k < 2$), which are then etched to form the desired features.

Plasma modeling provides a convenient technique to test and validate mechanisms. Simulations are cheaper then experiments, which may have to be run a number of times to test hypotheses. Modeling also allows the researcher to test parameter regimes that are not experimentally realizable. In this study, the surface reaction mechanisms of the etching process in fluorocarbon plasmas have been elucidated. The importance of the polymer film formed during etching is discussed, and the polymer has been resolved into constituent sites to understand the relation of the composition and thickness of the film to the etching. This reaction mechanism is then used with a Surface Kinetics Model (SKM) and interfaced with a plasma equipment model (HPEM) to model fluorocarbon plasma ICP reactors. It is found that the defluorination of the polymer layer has a direct relation to the etch rate for filsm with strongly bound monomers.

To investigate the effect of radiation on the etch process, a Monte Carlo Radiation Transport Model (MCRTM) was developed and integrated with the HPEM. The MCRTM arose out of a need to address radiation transport in geometries and plasma parameter regimes where simple analytic approximations would not hold. The HPEM and MCRTM are capable of handling diverse plasma conditions and reactor geometries. This is shown by the application of the MCRTM to the study of electrodeless lamps. The conclusions from the combined plasma and radiation model are that the spatial distribution of radiating and absorbing species is the most important determinant of the radiation transport through the lamp. This spatial distribution is strongly affected by the diffusion of species to the walls due to ambipolar fields.

The combined MCRTM and HPEM model was then applied to the fluorocarbon etch plasmas (C_4F_8/Ar mixtures), to perform a proof-of-principle study showing the importance of UV radiation on the etch rate. The assumption made was that the UV radiation would only participate in the defluorination of the polymer layer. With this assumption, it is seen that the etch rates decrease with increasing Ar, because the increasing photon flux due to the increased radiator density, is not enough to balance out the decrease in etch rate because of reduced fluorine precursors in the plasma. At these conditions, it is seen that the substrate bias results in an increase of radiaton flux to the surface, but this increase is dominated by the increase in the rates of ion-induced reactions.

10.2 Future Extensions

As written above, only a proof-of-principle study has been performed to understand the effects of UV radiation on etching processes. In reality, the UV photons may participate in numerous processes. These may include crosslinking of the polymer films, bond-straining of the polymer, and direct damage of the underlying dielectric to form electronic defects in the material. The experimental data needed to evaluate these processes is beginning to be published, and in the future, could be used to arrive at a complete reaction mechanism. Feature evolution on the scale of sub-microns can also be addressed using the reaction mechanism developed in this dissertation, with Monte Carlo surface profile codes.

The range of plasma conditions studied in this dissertation has been limited to fluorocarbon and fluorocarbon/Ar mixtures. Using the resolution of the polymer film provided by the surface model, studies can be performed on other gas chemistries, with oxygen and hydrogen, to understand the compositional dependence of the film on etch rate and on plasma conditions.

APPENDIX A: LIST OF REACTIONS FOR Ar/Hg [a]

Reaction	Rate coefficient[a]	Reference
$e + Ar \rightarrow Ar + e$	b	1
$e + Ar \rightarrow Ar(4s) + e$	b	2
$e + Ar \rightarrow Ar^+ + e + e$	b	3
$e + Ar(4s) \rightarrow Ar + e$	b	2, c
$e + Ar(4s) \rightarrow Ar^+ + e + e$	b	4, d
$e + Hg(6^1S_0) \rightarrow Hg(6^1S_0) + e$	b	5
$e + Hg(6^1S_0) \rightarrow Hg(6^3P_0) + e$	b	5
$e + H(6^1S_0) \rightarrow Hg(6^3P_1) + e$	b	5
$e + Hg(6^1S_0) \rightarrow Hg(6^3P_2) + e$	b	5
$e + Hg(6^1S_0) \rightarrow Hg(6^1P_1) + e$	b	5
$e + Hg(6^1S_0) \rightarrow Hg(6^3D_{J,}\ 7^3S_1) + e$	b	5
$e + Hg(6^1S_0) \rightarrow Hg^+ + e + e$	b	5
$e + Hg(6^3P_0) \rightarrow Hg(6^3P_0) + e$	b	5
$e + Hg(6^3P_0) \rightarrow Hg(6^1S_0) + e$	b	6,c
$e + Hg(6^3P_0) \rightarrow Hg(6^3P_1) + e$	b	6, c
$e + Hg(6^3P_0) \rightarrow Hg(6^3P_2) + e$	b	5
$e + Hg(6^3P_0) \rightarrow Hg(6^1P_1) + e$	b	6
$e + Hg(6^3P_0) \rightarrow Hg(6^3D_J) + e$	b	6
$e + Hg(6^3P_0) \rightarrow Hg(7^3S_1) + e$	b	6

$e + Hg(6^3P_0) \rightarrow Hg^+ + e + e$	b	7
$e + Hg(6^3P_1) \rightarrow Hg(6^3P_1) + e$	b	5
$e + Hg(6^3P_1) \rightarrow Hg(6^1S_0) + e$	b	6,c
$e + Hg(6^3P_1) \rightarrow Hg(6^3P_0) + e$	b	6,c
$e + Hg(6^3P_1) \rightarrow Hg(6^3P_2) + e$	b	5
$e + Hg(6^3P_1) \rightarrow Hg(6^1P_1) + e$	b	6
$e + Hg(6^3P_1) \rightarrow Hg(6^3D_J) + e$	b	6
$e + Hg(6^3P_1) \rightarrow Hg(7^3S_1) + e$	b	6
$e + Hg(6^3P_1) \rightarrow Hg^+ + e + e$	b	7
$e + Hg(6^3P_2) \rightarrow Hg(6^3P_2) + e$	b	5
$e + Hg(6^3P_2) \rightarrow Hg(6^1S_0) + e$	b	6,c
$e + Hg(6^3P_2) \rightarrow Hg(6^3P_0) + e$	b	6,c
$e + Hg(6^3P_2) \rightarrow Hg(6^3P_1) + e$	b	6,c
$e + Hg(6^3P_2) \rightarrow Hg(6^1P_1) + e$	b	6,c
$e + Hg(6^3P_2) \rightarrow Hg(6^3D_J) + e$	b	6
$e + Hg(6^3P_2) \rightarrow Hg(7^3S_1) + e$	b	6
$e + Hg(6^3P_2) \rightarrow Hg^+ + e + e$	b	6
$e + Hg(6^1P_1) \rightarrow Hg(6^1P_1) + e$	b	5
$e + Hg(6^1P_1) \rightarrow Hg(6^1S_0) + e$	b	5,c
$e + Hg(6^1P_1) \rightarrow Hg(6^3P_0) + e$	b	5,c
$e + Hg(6^1P_1) \rightarrow Hg(6^3P_1) + e$	b	5,c
$e + Hg(6^1P_1) \rightarrow Hg(6^3P_2) + e$	b	5,c

$e + Hg(6^1P_1) \rightarrow Hg^+ + e + e$	b	7
$e + Hg(6^3D_J) \rightarrow Hg(6^3D_J) + e$	b	5
$e + Hg(6^3D_J) \rightarrow Hg(6^1S_0) + e$	b	5,c
$e + Hg(6^3D_J) \rightarrow Hg(6^3P_0) + e$	b	5,c
$e + Hg(6^3D_J) \rightarrow Hg(6^3P_1) + e$	b	5,c
$e + Hg(6^3D_J) \rightarrow Hg(6^3P_2) + e$	b	5,c
$e + Hg(6^3D_J) \rightarrow Hg^+ + e + e$	b	7
$e + Hg(7^3S_1) \rightarrow Hg(7^3S_1) + e$	b	5
$e + Hg(7^3S_1) \rightarrow Hg(6^1S_0)+ e$	b	5,c
$e + Hg(7^3S_1) \rightarrow Hg(6^3P_0) + e$	b	5,c
$e + Hg(7^3S_1) \rightarrow Hg(6^3P_1) + e$	b	5,c
$e + Hg(7^3S_1) \rightarrow Hg(6^3P_2) + e$	b	5,c
$e + Hg(7^3S_1) \rightarrow Hg^+ + e + e$	b	7
$Ar(4s) + Ar(4s) \rightarrow Ar^+ + Ar + e$	5.0×10^{-10}	e
$Ar(4s) + Hg(6^1S_0) \rightarrow Hg^+ + Ar + e$	9.0×10^{-10}	8
$Ar(4s) + Hg \rightarrow Hg^+ + Ar + e$	9.0×10^{-10}	8,f
$Hg^* + Hg^* \rightarrow Hg^+ + Hg(6^1S_0) + e$	3.5×10^{-10}	9,i
$Ar^+ + Hg(6^1S_0) \rightarrow Hg^+ + Ar$	1.5×10^{-11}	10
$Ar^+ + Ar \rightarrow Ar + Ar^+$	4.6×10^{-10}	11
$Hg^+ + Hg \rightarrow Hg + Hg^+$	1.0×10^{-9}	f,g
$Hg(6^3P_1) \rightarrow Hg(6^1S_0) + h\nu$	$8.0 \times 10^6\ s^{-1}$	12,h
$Hg(6^1P_1) \rightarrow Hg(6^1S_0) + h\nu$	$7.5 \times 10^8\ s^{-1}$	12,h

$Hg(7^3S_1) \rightarrow Hg(6^3P_0) + h\nu$	$2.0 \times 10^7\ s^{-1}$	13
$Hg(7^3S_1) \rightarrow Hg(6^3P_1) + h\nu$	$6.0 \times 10^7\ s^{-1}$	13
$Hg(7^3S_1) \rightarrow Hg(6^3P_2) + h\nu$	$5.0 \times 10^7\ s^{-1}$	13
$Hg(6^3D_J) \rightarrow Hg(6^3P_0) + h\nu$	$2.2 \times 10^7\ s^{-1}$	13
$Hg(6^3D_J) \rightarrow Hg(6^3P_1) + h\nu$	$6.6 \times 10^7\ s^{-1}$	13
$Hg(6^3D_J) \rightarrow Hg(6^3P_2) + h\nu$	$2.0 \times 10^7\ s^{-1}$	13

Footnotes:

a. Rate coefficients have units of ($cm^3\ s^{-1}$) unless noted otherwise.

b. Rate coefficients are calculated in the EETM using cross sections from the indicated references.

c. Cross-section obtained by detailed balance.

d. By analogy with potassium.

e. Estimated as a gas phase kinetic rate constant.

f. Hg here represents all states.

g. Estimated.

h. Untrapped value which is modified by the MCRTM.

i. Hg* refers to each of the states 6^3P_0, 6^3P_1, 6^3P_2, 6^1P_1, 6^3D_J, and 7^3S_1.

A.1 References

1. M. Hayashi, Nagoya Institute of Technology Report No. IPPJ-AM-19 (1991).

2. K. Tachibana, Phys. Rev. A **34**, 1007 (1986).

3. D. Rapp and P. Englander-Golden, J. Chem. Phys. **43**, 1464 (1965).

4. R. H. MacFarland and J. D Kinney, Phys. Rev. **137**, A1058 (1965).

5. S. D. Rockwood, Phys. Rev. A **8**, 2348 (1973).

6. C. Kenty, J. Appl. Phys. **21**, 1309 (1950).

7. L. Vriens and A. H. M. Smeets, Phys. Rev. A **22**, 940 (1980).

8. D. J. Wren and D. W. Setser, J. Chem. Phys. **74**, 2331 (1981).

9. S. Majetich, E. M. Boczar, and J. R. Wiesenfeld, J. Appl. Phys. **66**, 475 (1989).

10. R. Johnsen, M. T. Leu and M. A. Biondi, Phys. Rev. A **8**, 1808 (1973).

11. J. D. C. Jones, D. G. Lister, K. Birkinshaw, and N. D. Twiddy, J. Phys. B **13**, 799 (1980).

12. T. J. Sommerer, J. Appl. Phys. **74**, 1579 (1993).

13. E. C. Benck, J. E. Lawler, and J. T. Dakin, J. Opt. Soc. Am. B **6**, 11 (1989).

APPENDIX B: LIST OF REACTIONS FOR C_4F_8 / Ar

B.1. Electron Impact Excitation, Ionization, and Dissociation Reactions.[a]

Reaction	Rate coefficient[b]	Reference
Collisions with argon		
$e + Ar \rightarrow Ar + e$	c	1
$e + Ar \rightarrow Ar^{*} + e$	c	2
$e + Ar \rightarrow Ar^{**} + e$	c	2
$e + Ar \rightarrow Ar^{+} + e + e$	c	3
$e + Ar^{*} \rightarrow Ar^{+} + e + e$	c	4
$e + Ar^{*} \rightarrow Ar + e$	c	2, d
$e + Ar^{*} \rightarrow Ar^{**} + e$	c	5
$e + Ar^{**} \rightarrow Ar + e$	c	2, d
$e + Ar^{**} \rightarrow Ar^{+} + e + e$	c	6
$e + Ar^{**} \rightarrow Ar^{*} + e$	c	5, d
$e + F \rightarrow F + e$	c	7
$e + F \rightarrow F(ex) + e$	c	7
$e + F \rightarrow F^{+} + e + e$	c	7
$e + F_2 \rightarrow F_2 + e$	c	8
$e + F_2 \rightarrow F_2(v) + e$	c	8
$e + F_2 \rightarrow F_2(ex) + e$	c	8

$e + F_2 \rightarrow F_2 + e$	c	8
$e + F_2 \rightarrow F^- + F$	c	8
$e + F_2 \rightarrow F_2^+ + e + e$	c	8
$e + CF \rightarrow CF + e$	c	9, e
$e + CF \rightarrow CF(v) + e$	c	9, e
$e + CF \rightarrow C + F + e$	c	9,e
$e + CF \rightarrow CF^+ + e + e$	c	10
$e + CF_2 \rightarrow CF_2 + e$	c	11, f
$e + CF_2 \rightarrow CF_2(v) + e$	c	11, f
$e + CF_2 \rightarrow CF + F^-$	c	11, f
$e + CF_2 \rightarrow CF + F + e$	c	11, f
$e + CF_2 \rightarrow CF_2^+ + e + e$	c	12
$e + CF_2 \rightarrow CF^+ + F + e + e$	c	12
$e + CF_3 \rightarrow CF_3 + e$	c	11, f
$e + CF_3 \rightarrow CF_3(v) + e$	c	11, f
$e + CF_3 \rightarrow CF_2 + F + e$	c	11, f
$e + CF_3 \rightarrow CF_3^+ + e + e$	c	12
$e + CF_3 \rightarrow CF_2^+ + F + e + e$	c	12
$e + CF_3 \rightarrow CF_2 + F^-$	c	11, f
$e + CF_4 \rightarrow CF_4 + e$	c	11
$e + CF_4 \rightarrow CF_4(v) + e$	c	11

$e + CF_4 \rightarrow CF_3 + F^-$	c	11
$e + CF_4 \rightarrow CF_3^- + F$	c	11
$e + CF_4 \rightarrow CF_3 + F + e$	c	11
$e + CF_4 \rightarrow CF_3^+ + F + e + e$	c	11
$e + CF_4 \rightarrow CF_2 + F + F + e$	c	11
$e + CF_4 \rightarrow CF_3^+ + F^- + e$	c	11
$e + CF_4 \rightarrow CF + F + F_2 + e$	c	11
$e + C_2F_3 \rightarrow CF + CF_2 + e$	$1 \times 10^{-8} T_e^{0.91} \exp(-5.0/T_e)$	13, g
$e + C_2F_4 \rightarrow C_2F_4 + e$	c	14,15
$e + C_2F_4 \rightarrow C_2F_4(v) + e$	c	14,15
$e + C_2F_4 \rightarrow CF_2 + CF_2 + e$	c	14,15
$e + C_2F_4 \rightarrow C_2F_4^+ + e + e$	c	14,15
$e + C_2F_4 \rightarrow C_2F_3^+ + F + e$	c	14,15
$e + C_2F_4 \rightarrow CF^+ + CF_3 + e + e$	c	14,15
$e + C_2F_5 \rightarrow C_2F_5 + e$	c	16, h
$e + C_2F_5 \rightarrow C_2F_5(v) + e$	c	16, h
$e + C_2F_5 \rightarrow CF_3^- + CF_2$	c	16, h
$e + C_2F_5 \rightarrow CF_3 + CF_2 + e$	c	16, h
$e + C_2F_5 \rightarrow CF_3^+ + CF_2 + e + e$	c	17
$e + C_2F_5 \rightarrow C_2F_5^+ + e + e$	c	17
$e + C_2F_6 \rightarrow CF_3^+ + CF_3 + e + e$	c	16

$e + C_2F_6 \rightarrow C_2F_6 + e^-$	c	16
$e + C_2F_6 \rightarrow C_2F_6(v) + e^-$	c	16
$e + C_2F_6 \rightarrow CF_3 + CF_3^-$	c	16
$e + C_2F_6 \rightarrow C_2F_5 + F^-$	c	16
$e + C_2F_6 \rightarrow CF_3 + CF_3 + e$	c	16
$e + C_3F_5 \rightarrow C_2F_3 + CF_2 + e$	$1.8 \times 10^{-8}\ T_e^{\ 0.52} \exp(-12.3/T_e)$	14,15, g,i
$e + C_3F_5 \rightarrow C_2F_4 + CF + e$	$1.8 \times 10^{-8}\ T_e^{\ 0.52} \exp(-12.3/T_e)$	14,15’ g,i
$e + C_3F_6 \rightarrow C_3F_6^+ + e + e$	$1.4 \times 10^{-8}\ T_e^{\ 0.68} \exp(-10.6/T_e)$	14,15, g,i
$e + C_3F_6 \rightarrow C_2F_3 + CF_3 + e$	$1.8 \times 10^{-8}\ T_e^{\ 0.52} \exp(-12.3/T_e)$	14,15, g,i
$e + C_3F_6 \rightarrow C_2F_4 + CF_2 + e$	$1.8 \times 10^{-8}\ T_e^{\ 0.52} \exp(-12.3/T_e)$	14,15, g,i
$e + C_3F_7 \rightarrow C_2F_4 + CF_3 + e$	$1.8 \times 10^{-8}\ T_e^{\ 0.52} \exp(-12.3/T_e)$	14,15, g,i
$e + C_4F_7 \rightarrow C_2F_4 + C_2F_3 + e$	$5.7 \times 10^{-8}\ T_e^{\ 0.28} \exp(-8.0/T_e)$	16, g,h
$e + C_4F_7 \rightarrow C_4F_7^+ + e + e$	$1.4 \times 10^{-8}\ T_e^{\ 0.68} \exp(-10.6/T_e)$	16, g,h
$e + C_4F_8 \rightarrow C_4F_8 + e$	c	18
$e + C_4F_8 \rightarrow C_4F_8(v) + e$	c	18
$e + C_4F_8 \rightarrow C_2F_4 + C_2F_4 + e$	c	18, j
$e + C_4F_8 \rightarrow C_4F_8^{-}*$	c	18
$e + C_4F_8 \rightarrow F^- + C_4F_7$	c	18
$e + C_4F_8 \rightarrow C_3F_5^+ + CF_3 + e + e$	c	19
$e + C_4F_8 \rightarrow C_2F_4^+ + C_2F_4 + e + e$	c	19
$e + C_4F_8 \rightarrow F^+ + C_4F_7 + e + e$	c	19
$e + C_4F_8 \rightarrow CF_3^+ + C_3F_5 + e + e$	c	19

$e + C_4F_8 \rightarrow CF_2^+ + C_3F_6 + e + e$ c 19

$e + C_4F_8 \rightarrow CF^+ + C_3F_7 + e + e$ c 19

Fitting parameters used in Eqs. (1-3)

	C_4F_8 (v)	C_4F_8 (dissociation)	C_2F_4 (v1)	C_2F_4 (v2)
f_0	0.0339	0.7165	0.0412	0.1206
α	0.0057	0.7426	0.0010	9.15×10^{-5}
β	0.8252	1.0158	0.5248	0.5190
Ω	1.2279		0.9391	0.9369
c		0.7602		

Notes:

a. Only reactions directly affecting species densities are included in the FKM. The additional electron impact collisions such as momentum transfer and excitation of vibrational and electronic states are included in the EETM to account for the transport and energy loses of electron. Vibrational cross sections for c-C_4F_8 and C_2F_4 were analytically represented using Eqs. (8) and (9) and fitting parameters are listed on the bottom of the table.

b. Rate coefficients have units of cm^3/s unless noted otherwise.

c. Rate coefficient is calculated from electron energy distribution obtained in the EETM using the cross section from the cited reference.

d. Cross section was obtained by detailed balance.

e. Estimated by analogy to NF.

f. Estimated by analogy to CF_4.

g. Estimated using Maxwellian distribution.

h. Estimated by analogy to C_2F_6.

i. Estimated by analogy to C_2F_4.

j. Cross section was analytically represented using Ref. 48, Eqn (11).

B.2. Neutral Heavy Particle Reactions.

Reaction	Rate coefficient[a]	Reference
Excitation transfer and radiative decay		
$Ar^* + CF_2 \rightarrow CF + F + Ar$	6.0×10^{-11}	20, b
$Ar^* + CF_3 \rightarrow CF_2 + F + Ar$	6.0×10^{-11}	20, b
$Ar^* + CF_4 \rightarrow CF_2 + F_2 + Ar$	6.0×10^{-11}	20
$Ar^* + C_2F_4 \rightarrow CF_2 + CF_2 + Ar$	4.0×10^{-11}	20, b
$Ar^* + C_2F_5 \rightarrow C_2F_5 + Ar$	4.0×10^{-11}	20, b
$Ar^* + C_2F_6 \rightarrow CF_3 + CF_3 + Ar$	4.0×10^{-11}	20
$Ar^* + C_3F_5 \rightarrow C_3F_5 + Ar$	4.0×10^{-11}	20, b
$Ar^* + C_3F_6 \rightarrow C_3F_6 + Ar$	4.0×10^{-11}	20, b
$Ar^* + C_3F_7 \rightarrow C_3F_7 + Ar$	4.0×10^{-11}	20, b
$Ar^* + C_4F_8 \rightarrow C_2F_4 + C_2F_4 + Ar$	9.0×10^{-10}	20, b
$Ar^* + Ar^* \rightarrow Ar^+ + Ar + e$	1.2×10^{-9}	21

$Ar^{**} + Ar^{**} \rightarrow Ar^{+} + Ar + e$	1.2×10^{-9}		21
$Ar^{**} + Ar^{*} \rightarrow Ar^{+} + Ar + e$	1.2×10^{-9}		21
$Ar^{**} \rightarrow Ar^{*}$	10^{5} s^{-1}		d
$Ar^{+} + Ar \rightarrow Ar^{+} + Ar$	5.7×10^{-10}		22
$C + C_2F_4 \rightarrow C_2F_3 + CF$	1.91×10^{-10}		23
$CF_2 + CF_3 \rightarrow C_2F_5$	1.0×10^{-12}		24
$CF_2 + CF_2 \rightarrow C_2F_4$	7.21×10^{-14}		25
$CF_3 + CF_3 + M \rightarrow M + C_2F_6$	3.94×10^{-29}	cm^{6} s^{-1}	26
$CF_3 + CF_3 \rightarrow C_2F_6$	8.30×10^{-12}		24
$F + CF_3 \rightarrow CF_4$	2.0×10^{-11}		27
$F + CF_2 \rightarrow CF_3$	1.8×10^{-11}		28
$F + CF \rightarrow CF_2$	9.96×10^{-11}		29
$F + F + M \rightarrow F_2 + M$	6.77×10^{-34}	cm^{6} s^{-1}	26
$F + C_2F_4 \rightarrow CF_3 + CF_2$	4.8×10^{-11}		30
$F + C_2F_5 \rightarrow CF_3 + CF_3$	1.0×10^{-11}		31
$F + C_4F_7 \rightarrow C_2F_4 + C_2F_4$	1.0×10^{-11}		e
$F + C_3F_6 \rightarrow C_3F_7$	1.0×10^{-12}		31, e
$F + C_2F_3 \rightarrow C_2F_4$	1.0×10^{-12}		31
$F + CF_3 + M \rightarrow CF_4 + M$	1.6×10^{-28}		30
$F_2 + CF_2 \rightarrow CF_3 + F$	8.3×10^{-14}		29
$F_2 + CF_3 \rightarrow CF_4 + F$	1.9×10^{-14}		32
$F_2 + C_2F_4 \rightarrow C_2F_5 + F$	3.5×10^{-16}		33

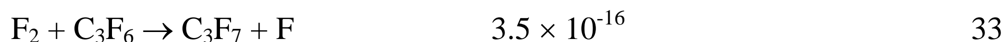

$F_2 + C_3F_6 \rightarrow C_3F_7 + F$ 3.5×10^{-16} 33

<u>Notes:</u>

a. Rate coefficients have units of $cm^3\ s^{-1}$ unless noted otherwise.

b. Estimated by analogy to CF_4.

c. Estimated by analogy to C_2F_6.

d. Estimated for a mildly trapped optical transition.

e. Estimated.

B.3. Ion-molecule Reactions.

Reaction	Rate coefficient[a]	Reference
Charge exchange collisions		
$Ar^+ + CF_2 \rightarrow CF^+ + Ar + F$	5.0×10^{-10}	34, b
$Ar^+ + CF_3 \rightarrow CF_2^+ + Ar + F$	5.0×10^{-10}	34, b
$Ar^+ + CF_4 \rightarrow CF_3^+ + Ar + F$	4.8×10^{-10}	34
$Ar^+ + C_2F_6 \rightarrow CF_3^+ + CF_3 + Ar$	5.0×10^{-10}	35, c
$Ar^+ + C_4F_8 \rightarrow CF_3^+ + C_3F_5 + Ar$	1.0×10^{-10}	35, c
$Ar^+ + C_4F_8 \rightarrow C_3F_5^+ + CF_3 + Ar$	3.0×10^{-10}	35, c
$Ar^+ + C_4F_8 \rightarrow C_2F_4^+ + C_2F_4 + Ar$	3.0×10^{-10}	35, c
$Ar^+ + C_4F_8 \rightarrow CF^+ + C_3F_7 + Ar$	1.0×10^{-10}	35, c

$C^+ + C \rightarrow C^+ + C$	3.0×10^{-9}	18, d,e
$C^+ + CF \rightarrow CF^+ + C$	3.18×10^{-9}	18
$CF^+ + CF \rightarrow CF^+ + CF$	1.0×10^{-9}	36, f,e
$CF^+ + CF_2 \rightarrow CF_2^+ + CF$	1.0×10^{-9}	36, f
$CF^+ + CF_3 \rightarrow CF_3^+ + CF$	1.71×10^{-9}	36
$CF_2^+ + CF_2 \rightarrow CF_2^+ + CF_2$	1.0×10^{-9}	18, f,e
$CF_2^+ + CF_3 \rightarrow CF_3^+ + CF_2$	1.48×10^{-9}	18
$CF_3^+ + C_3F_5 \rightarrow C_3F_5^+ + CF_3$	7.04×10^{-10}	37
$CF_3^+ + C_3F_7 \rightarrow C_3F_7^+ + CF_3$	7.04×10^{-10}	37, g
$CF_3^+ + CF_3 \rightarrow CF_3^+ + CF_3$	1.0×10^{-9}	18, b,e
$C_2F_4^+ + C_2F_4 \rightarrow C_2F_4 + C_2F_4^+$	4.0×10^{-9}	e
$C_2F_5^+ + C_2F_5 \rightarrow C_2F_5 + C_2F_5^+$	4.0×10^{-9}	e
$C_3F_5^+ + C_3F_5 \rightarrow C_3F_5^+ + C_3F_5$	3.0×10^{-9}	e
$C_3F_7^+ + C_3F_7 \rightarrow C_3F_7^+ + C_3F_7$	3.0×10^{-9}	e
$C^+ + CF_3 \rightarrow CF_2^+ + CF$	2.48×10^{-9}	18
$CF^+ + CF_4 \rightarrow CF_3^+ + CF_2$	1.80×10^{-10}	38
$CF^+ + C_2F_4 \rightarrow CF_3^+ + CF + CF$	2.60×10^{-10}	37
$CF^+ + C_2F_4 \rightarrow C_3F_5^+$	1.30×10^{-10}	37
$CF^+ + C_2F_6 \rightarrow CF_3^+ + C_2F_4$	2.0×10^{-10}	38
$CF_2^+ + C_4F_8 \rightarrow C_3F_5 + C_2F_4 + F$	2.10×10^{-11}	18
$CF_2^+ + C_2F_4 \rightarrow C_2F_4^+ + CF_2$	1.00×10^{-9}	37
$CF_2^+ + C_2F_6 \rightarrow C_2F_5^+ + CF_3$	3.50×10^{-11}	18,39

$CF_2^+ + CF_4 \rightarrow CF_3^+ + CF_3$	0.40×10^{-9}	38
$CF_2^+ + CF \rightarrow CF_3^+ + C$	2.06×10^{-9}	18
$CF_2^+ + C \rightarrow CF^+ + CF$	1.04×10^{-9}	18
$CF_3^+ + C_2F_4 \rightarrow C_3F_7^+$	3.30×10^{-11}	37
$CF_3^+ + C_2F_6 \rightarrow C_2F_5^+ + CF_4$	2.50×10^{-12}	38
$CF_3^- + F \rightarrow CF_3 + F^-$	5.0×10^{-8}	40
$CF_3^- + CF_3 \rightarrow C_2F_6 + e$	1.0×10^{-10}	i
$C_2F_4^+ + C_2F_4 \rightarrow C_3F_5^+ + CF_3$	2.0×10^{-11}	37
$C_3F_7^+ + C_2F_4 \rightarrow CF_3^+ + C_4F_8$	2.0×10^{-11}	37
$C_4F_8^- + F \rightarrow C_4F_8 + F^-$	1.0×10^{-9}	i
$F^+ + F \rightarrow F^+ + F$	1.0×10^{-9}	18, e,h
$F^+ + F_2 \rightarrow F_2^+ + F$	7.94×10^{-10}	18
$F^+ + C \rightarrow C^+ + F$	1.17×10^{-9}	18
$F^+ + CF \rightarrow C^+ + F_2$	2.71×10^{-9}	18
$F^+ + CF_2 \rightarrow CF^+ + F_2$	2.28×10^{-9}	18
$F^+ + CF_3 \rightarrow CF_2^+ + F_2$	2.90×10^{-9}	18
$F^+ + CF_4 \rightarrow CF_3^+ + F_2$	1.0×10^{-9}	18
$F^+ + C_2F_4 \rightarrow C_2F_3^+ + F_2$	1.0×10^{-9}	18
$F^+ + C_2F_6 \rightarrow C_2F_5^+ + F_2$	1.0×10^{-9}	18
$F^+ + C_2F_5 \rightarrow C_2F_4^+ + F_2$	1.0×10^{-9}	18
$F_2^+ + CF \rightarrow CF_2^+ + F$	2.18×10^{-9}	18
$F_2^+ + C \rightarrow CF^+ + F$	1.04×10^{-9}	18

$F_2^+ + CF_2 \rightarrow CF_3^+ + F$	1.79×10^{-9}	18
$F_2^+ + CF_3 \rightarrow CF_3^+ + F + F$	1.60×10^{-9}	18
$F_2^+ + CF_4 \rightarrow CF_3^+ + F + F_2$	1.0×10^{-10}	18, i
$F_2^+ + C_2F_4 \rightarrow C_2F_4^+ + F_2$	1.0×10^{-10}	18, i
$F_2^+ + C_2F_5 \rightarrow C_2F_5^+ + F_2$	1.0×10^{-10}	18, i
$F_2^+ + F_2 \rightarrow F_2^+ + F_2$	1.0×10^{-9}	e,i
$C_4F_8^{-*} \rightarrow C_4F_8 + e$	$2.0 \times 10^{6}\ s^{-1}$	41,42
$C_4F_8^{-*} + M \rightarrow C_4F_8^- + M$	1.0×10^{-10}	i
$F^- + CF_3 \rightarrow CF_4 + e$	4.0×10^{-10}	43
$F^- + CF_2 \rightarrow CF_3 + e$	3.0×10^{-10}	43
$F^- + CF \rightarrow CF_2 + e$	2.0×10^{-10}	43
$F^- + C \rightarrow CF + e$	1.0×10^{-10}	43
$F^- + F \rightarrow F_2 + e$	1.0×10^{-10}	43

Notes:

a. Rate coefficients have units of $cm^3\ s^{-1}$ unless noted otherwise. Two body rate coefficients are shown for T = 330 K and are scaled by $(T/300)^{1/2}$.

b. Estimated by analogy to CF_4.

c. Calculated from cross sections using Maxwell distribution.

d. Estimated by analogy to CF.

e. Included for gas heating only.

f. Estimated by analogy to CF_3.

g. Estimated by analogy to C_3F_5.

h. Estimated by analogy to F_2.

i. Estimated.

B.4. Ion-ion and Ion-electron Reactions.

Reaction	Rate coefficient[a]	Reference
Ion-ion neutralization		
$CF_3^- + Ar^+ \rightarrow CF_3 + Ar$	2.0×10^{-7}	44
$CF_3^- + CF^+ \rightarrow CF_3 + CF$	2.0×10^{-7}	45,46b
$CF_3^- + C^+ \rightarrow CF_3 + C$	3.0×10^{-7}	45,46b
$CF_3^- + F^+ \rightarrow CF_3 + F$	2.5×10^{-7}	45,46b
$CF_3^- + F_2^+ \rightarrow CF_3 + F_2$	2.0×10^{-7}	45,46b
$CF_3^- + CF_3^+ \rightarrow CF_3 + CF_3$	1.5×10^{-7}	44
$CF_3^- + C_2F_4^+ \rightarrow CF_3 + C_2F_4$	1.0×10^{-7}	45,46b
$CF_3^- + C_2F_3^+ \rightarrow CF_3 + C_2F_3$	1.0×10^{-7}	45,46b
$CF_3^- + C_2F_5^+ \rightarrow CF_3 + C_2F_5$	1.0×10^{-7}	45,46b
$CF_3^- + C_3F_5^+ \rightarrow CF_3 + C_3F_5$	1.0×10^{-7}	45,46b
$CF_3^- + C_3F_7^+ \rightarrow CF_3 + C_3F_7$	1.0×10^{-7}	45,46b
$CF_3^- + C_4F_7^+ \rightarrow CF_3 + C_4F_7$	1.0×10^{-7}	45,46b
$CF_3^- + CF_2^+ \rightarrow CF_3 + CF_2$	2.0×10^{-7}	45,46b
$C_4F_8- + Ar^+ \rightarrow C_4F_8 + Ar$	9.0×10^{-8}	45,46b
$C_4F_8-* + Ar^+ \rightarrow C_4F_8 + Ar$	9.0×10^{-8}	45,46b

$C_4F_8^- + CF^+ \rightarrow C_4F_8 + CF$	1.5×10^{-7}	45,46b
$C_4F_8^- + C^+ \rightarrow C_4F_8 + C$	3.0×10^{-7}	45,46b
$C_4F_8^- + F^+ \rightarrow C_4F_8 + F$	2.0×10^{-7}	45,46b
$C_4F_8^- + F_2^+ \rightarrow C_4F_8 + F_2$	1.5×10^{-7}	45,46b
$C_4F_8^- + CF_3^+ \rightarrow C_4F_8 + CF_3$	1.0×10^{-7}	45,46b
$C_4F_8^- + C_2F_4^+ \rightarrow C_4F_8 + C_2F_4$	9.0×10^{-8}	45,46b
$C_4F_8^- + C_2F_3^+ \rightarrow C_4F_8 + C_2F_3$	9.0×10^{-8}	45,46b
$C_4F_8^- + C_2F_5^+ \rightarrow C_4F_8 + C_2F_5$	9.0×10^{-8}	45,46b
$C_4F_8^- + C_3F_5^+ \rightarrow C_4F_8 + C_3F_5$	9.0×10^{-8}	45,46b
$C_4F_8^- + C_3F_6^+ \rightarrow C_4F_8 + C_3F_6$	9.0×10^{-8}	45,46b
$C_4F_8^- + C_3F_7^+ \rightarrow C_4F_8 + C_3F_7$	9.0×10^{-8}	45,46b
$C_4F_8^- + C_4F_7^+ \rightarrow C_4F_8 + C_4F_7$	9.0×10^{-8}	45,46b
$C_4F_8^- + CF_2^+ \rightarrow C_4F_8 + CF_2$	1.0×10^{-7}	45,46b
$C_4F_8^{-*} + CF^+ \rightarrow C_4F_8 + CF$	2.0×10^{-7}	45,46b
$C_4F_8^{-*} + C^+ \rightarrow C_4F_8 + C$	3.0×10^{-7}	45,46b
$C_4F_8^{-*} + F^+ \rightarrow C_4F_8 + F$	2.0×10^{-7}	45,46b
$C_4F_8^{-*} + F_2^+ \rightarrow C_4F_8 + F_2$	1.5×10^{-7}	45,46b
$C_4F_8^{-*} + CF_3^+ \rightarrow C_4F_8 + CF_3$	1.0×10^{-7}	45,46b
$C_4F_8^{-*} + C_2F_4^+ \rightarrow C_4F_8 + C_2F_4$	9.0×10^{-8}	45,46b
$C_4F_8^{-*} + C_2F_3^+ \rightarrow C_4F_8 + C_2F_3$	9.0×10^{-8}	45,46b
$C_4F_8^{-*} + C_2F_5^+ \rightarrow C_4F_8 + C_2F_5$	9.0×10^{-8}	45,46b
$C_4F_8^{-*} + C_3F_5^+ \rightarrow C_4F_8 + C_3F_5$	9.0×10^{-8}	45,46b

$C_4F_8^{-*} + C_3F_6^+ \rightarrow C_4F_8 + C_3F_6$	9.0×10^{-8}	45,46b
$C_4F_8^{-*} + C_3F_7^+ \rightarrow C_4F_8 + C_3F_7$	9.0×10^{-8}	45,46b
$C_4F_8^{-*} + C_4F_7^+ \rightarrow C_4F_8 + C_4F_7$	9.0×10^{-8}	45,46b
$C_4F_8^{-*} + CF_2^+ \rightarrow C_4F_8 + CF_2$	1.0×10^{-7}	45,46b
$F^- + Ar^+ \rightarrow F + Ar$	2.0×10^{-7}	44
$F^- + CF_3^+ \rightarrow F + CF_3$	8.7×10^{-8}	14
$F^- + CF_2^+ \rightarrow F + CF_2$	9.1×10^{-8}	14
$F^- + CF^+ \rightarrow CF + F$	9.8×10^{-8}	14
$F^- + F_2^+ \rightarrow F + F_2$	9.4×10^{-8}	14
$F^- + F^+ \rightarrow F + F$	3.1×10^{-7}	14
$F^- + C^+ \rightarrow F + C$	2.2×10^{-7}	14
$F^- + C_2F_5^+ \rightarrow F + C_2F_5$	9.0×10^{-8}	45,46b
$F^- + C_2F_3^+ \rightarrow F + C_2F_3$	9.0×10^{-8}	45,46b
$F^- + CF_3^+ \rightarrow CF_2 + F_2$	8.7×10^{-8}	14
$F^- + CF_3^+ \rightarrow CF_2 + F + F$	3.0×10^{-7}	43
$F^- + CF_2^+ \rightarrow CF + F_2$	9.1×10^{-8}	14
$F^- + CF^+ \rightarrow C + F + F$	4.0×10^{-7}	43
$F^- + C_2F_4^+ \rightarrow CF + CF_2 + F_2$	8.2×10^{-8}	14
$F^- + C_3F_5^+ \rightarrow C_2F_4 + CF_2$	8.0×10^{-8}	14
$F^- + C_3F_6^+ \rightarrow C_2F_4 + CF_3$	8.0×10^{-8}	14c
$F^- + C_3F_7^+ \rightarrow C_2F_6 + CF_2$	8.0×10^{-8}	14c
$F^- + C_4F_7^+ \rightarrow C_2F_5 + CF_2$	8.0×10^{-8}	14c

Electron-ion recombination reactions

$e + Ar \rightarrow Ar^{**}$	$8.15 \times 10^{-13}\ T_e^{-0.5}$	47
$e + F_2^+ \rightarrow F + F$	$8.0 \times 10^{-8}\ T_e^{-0.5}$	d
$e + CF^+ \rightarrow C + F$	$8.0 \times 10^{-8}\ T_e^{-0.5}$	d
$e + CF_3^+ \rightarrow CF_2 + F$	$8.0 \times 10^{-8}\ T_e^{-0.5}$	d
$e + CF_2^+ \rightarrow CF + F$	$8.5 \times 10^{-8}\ T_e^{-0.5}$	d
$e + C_2F_5^+ \rightarrow CF_3 + CF_2$	$8.0 \times 10^{-8}\ T_e^{-0.5}$	d
$e + C_2F_4^+ \rightarrow CF_2 + CF_2$	$8.0 \times 10^{-8}\ T_e^{-0.5}$	d
$e + C_2F_3^+ \rightarrow CF_2 + CF$	$8.0 \times 10^{-8}\ T_e^{-0.5}$	d
$e + C_3F_5^+ \rightarrow C_2F_3 + CF_2$	$8.0 \times 10^{-8}\ T_e^{-0.5}$	d
$e + C_3F_6^+ \rightarrow C_2F_4 + CF_2$	$8.0 \times 10^{-8}\ T_e^{-0.5}$	d
$e + C_3F_7^+ \rightarrow C_2F_4 + CF_3$	$8.0 \times 10^{-8}\ T_e^{-0.5}$	d
$e + C_4F_7^+ \rightarrow C_2F_4 + C_2F_3$	$8.0 \times 10^{-8}\ T_e^{-0.5}$	d

a. Rate coefficients have units of cm^3/s unless noted otherwise. Two body rate coefficients for heavy particle collisions are shown for T = 330 K and are scaled by $(T/300)^{1/2}$.

b. Estimated using scaling discussed in Refs. [45]and [46] and present ion saturation current measurements.

c. Estimated by analogy to $C_3F_5^+$.

d. Estimated.

B.5 References

1. M. Hayashi, Nagoya Institute of Technology Report, No. IPPJ-AM-19 (1991).
2. K. Tachibana, Physical Review A **34**, 1007 (1986).
3. D. Rapp and P. Englander-Golden, The Journal of Chemical Physics **43**, 1464 (1965).
4. R. H. McFarland and J. D. Kinney, Physical Review **137**, 1058 (1965).
5. I. P. Zapesochnyi, Y. N. Semenyuk, A. I. Dashchenko, A. E. Imre, and A. I. Zapesochny, JETP Lett. **39**, 141 (1984).
6. L. Vriens, Physics Letters **8**, 260 (1964).
7. W. L. Morgan, (private communication), Kinema Software, http://www.kinema.com.
8. M. Hayashi and T. Nimura, Journal of Applied Physics **54**, 4879 (1983).
9. E. Meeks, J. Electrochem. Soc. **144**, 357 (1998).
10. V. Tarnovsky and K. Becker, J. Chem. Phys. **98**, 7868 (1993).
11. R. A. Bonham, Japanese Journal of Applied Physics **33**, 4157 (1994).
12. V. Tarnovsky, P. Kurunczi, R. D., and K. Becker, **128**, 181 (1993).
13. M. Gryzinski, Physical Review **138**, A336 (1965).
14. K. Yoshida, S. Goto, H. Tagashira, C. Winstead, B. V. McKoy, and W. L. Morgan, Journal of Applied Physics **91**, 2637 (2002).
15. C. Winstead and V. McKoy, J. Chem. Phys. **116**, 1380 (2002).
16. M. Hayashi and A. Niwa, Proceedings of the Fifth International Symposium on Gaseous Dielectrics, 27 (1987).
17. V. Tarnovsky, H. Deutsch, and K. Becker, J. Phys. B **32**, L573 (1999).

18. G. I. Font, W. L. Morgan, and G. Mennenga, Journal of Applied Physics **91**, 3530 (2002).

19. C. Q. Jiao, A. Garscadden, and P. D. Haaland, Chem. Phys. Lett. **297**, 121 (1998).

20. J. E. Velazco, J. H. Kolts, and D. W. Setser, The Journal of Chemical Physics **65**, 3468 (1976).

21. A. N. Klucharev and V. Vujnovic, Physics Reports **185**, 55 (1990).

22. H. W. Ellis, R. Y. Pai, E. W. McDaniel, E. A. Mason, and L. A. Viehland, Atomic Data and Nuclear Data Tables **17**, 177 (1976).

23. N. Haider and D. Husain, Int. J. Chem. Kinet **25**, 423 (1993).

24. I. C. Plumb and K. R. Ryan, Plasma Chemistry and Plasma Processing **6**, 205 (1986).

25. P. K. Chowdhury, K. V. S. R. Rao, and J. P. Mittal, J. Phys. Chem. **92**, 102 (1988).

26. K. Okada, O. Kajimoto, and T. Fueno, Chem. Soc. Jpn. B **51**, 443 (1978).

27. I. C. Plumb and K. R. Ryan, Plasma Chemistry and Plasma Processing **9**, 409 (1989).

28. C. Tsai, S. M. Belanger, J. T. Kim, J. R. Lord, and D. L. McFadden, Journal of Physical Chemistry **93**, 1916 (1989).

29. D. R. Burgess, M. R. Zachariah, W. Tsang, and P. R. Westmoreland, Progressive Energy and Combustion Science **21**, 453 (1996).

30. N. I. Butkovskaya, M. N. Larichev, I. O. Leipunskii, I. I. Morozov, and V. L. Talroze, Kinet. Catal. **21**, 263 (1980).

31. K. R. Ryan and I. C. Plumb, Plasma Chemistry and Plasma Processing **6**, 231 (1986).

32. E. L. Keating and R. A. Matula, J. Chem. Phys. **66**, 1237 (1977).

33. V. L. Orkin and A. M. Chaikin, Kinet. Catal. **23**, 438 (1982).

34. E. R. Fisher, M. E. Weber, and P. B. Armentrout, The Journal of Chemical Physics **92**, 2296 (1990).

35. D. Smith and L. Kevan, The Journal of Chemical Physics **55**, 2290 (1971).

36. D. P. Almeida, A. C. Fontes, and C. F. L. Godinho, Journal of Physics B: Atomic and Molecular Optical Physics **28**, 3335 (1995).

37. R. A. Morris, A. A. Viggiano, and J. F. Paulson, Journal of Physical Chemistry **97**, 6208 (1993).

38. R. A. Morris, A. A. Viggiano, J. M. Van Doren, and J. F. Paulson, Journal of Physical Chemistry **96**, 2597 (1992).

39. G. K. Jarvis, C. A. Mayhew, and R. P. Tuckett, Journal of Physical Chemistry **100**, 17166 (1996).

40. G. K. Vinogradov, P. I. Verzorov, L. S. Polak, and K. I. Slovetsky, Vacuum **32**, 592 (1982).

41. I. Sauers, L. G. Christophorou, and J. G. Carter, J. Chem. Phys. **71**, 3016 (1979).

42. R. L. Woodin, M. S. Foster, and J. L. Beauchamp, J. Chem. Phys. **72**, 4223 (1980).

43. P. Ho, J. E. Johannes, R. J. Buss, and E. Meeks, Journal of Vacuum Science and Technology A **19**, 2344 (2001).

44. R. E. Olson, J. R. Peterson, and J. Moseley, The Journal of Chemical Physics **53**, 3391 (1970).

45. J. T. Moseley, R. E. Olson, and J. R. Peterson, Case Studies in Atomic Physics **5**, 1 (1975).

46. A. P. Hickman, The Journal of Chemical Physics **70**, 4872 (1979).

47. M. A. Biondi, in *Principles of Laser Plasmas*, edited by G. Bekefi (Wiley, New York, 1976).

48. A. V. Vasenkov, X. Li, G. Oehrlein, and M. J. Kushner, J. Vac. Sci. Technol. A **22**, 511 (2004).

APPENDIX C. LIST OF REACTIONS FOR C_2F_6 / Ar [a]

Reaction	Rate Coefficient[b]	Reference
$e + Ar \rightarrow Ar^* + e$	c	1
$e + Ar \rightarrow Ar^+ + e + e$	c	2
$e + Ar^* \rightarrow Ar^+ + e + e$	c	3
$e + Ar^* \rightarrow Ar + e$	c	3
$e + CF_4 \rightarrow CF_3 + F^-$	c	4
$e + CF_4 \rightarrow CF_3^- + F$	c	4
$e + CF_4 \rightarrow CF_3 + F + e$	c	4
$e + CF_4 \rightarrow CF_3^+ + F + e + e$	c	4
$e + CF_4 \rightarrow CF_2 + F + F + e$	c	4
$e + CF_3 \rightarrow CF_2 + F + e$	c	4,d
$e + CF_3 \rightarrow CF_2 + F^-$	c	4,d
$e + CF_3 \rightarrow CF_3^+ + e + e$	c	15
$e + CF_2 \rightarrow CF_2^+ + e + e$	c	16
$e + CF_2 \rightarrow CF + F + e$	c	5,d
$e + CF_2 \rightarrow CF + F^-$	c	5,d
$e + C_2F_6 \rightarrow CF_3^+ + CF_3 + e + e$	c	5
$e + C_2F_6 \rightarrow CF_3 + CF_3^-$	c	5
$e + C_2F_6 \rightarrow C_2F_5 + F^-$	c	5
$e + C_2F_6 \rightarrow CF_3 + CF_3 + e$	c	5
$e + C_2F_4 \rightarrow CF_2 + CF_2 + e$	c	5,e

$e + C_2F_4 \rightarrow C_2F_4^+ + e + e$	c	5,e
$e + C_2F_4 \rightarrow F^- + C_2F_3$	c	5
$e + F_2 \rightarrow F^- + F$	c	6,f
$e + F_2 \rightarrow F + F + e$	c	6,f
$e + CF_3^+ \rightarrow CF_2 + F$	2.0×10^{-8}	6,f
$e + C_2F_5^+ \rightarrow CF_3 + CF_2$	2.0×10^{-8}	6,f
$e + C_2F_4^+ \rightarrow CF_2 + CF_2$	2.0×10^{-8}	6,f
$Ar^+ + Ar \rightarrow Ar + Ar^+$	1.0×10^{-9}	7
$Ar^+ + CF_4 \rightarrow CF_3^+ + F + Ar$	7.0×10^{-10}	7
$Ar^+ + CF_3 \rightarrow CF_3^+ + Ar$	7.0×10^{-10}	7
$Ar^+ + C_2F_6 \rightarrow CF_3^+ + CF_3 + Ar$	9.58×10^{-10}	7
$Ar^+ + C_2F_5 \rightarrow C_2F_5^+ + Ar$	1.0×10^{-10}	8,f
$Ar^+ + C_2F_4 \rightarrow C_2F_4^+ + Ar$	1.0×10^{-10}	8,f
$Ar^* + Ar^* \rightarrow Ar^+ + Ar + e$	5.0×10^{-10}	9
$Ar^* + CF_4 \rightarrow CF_2 + F_2 + Ar$	4.0×10^{-11}	10
$Ar^* + CF_3 \rightarrow CF_2 + F + Ar$	4.0×10^{-11}	10
$Ar^* + CF_2 \rightarrow CF + F + Ar$	4.0×10^{-11}	10
$Ar^* + C_2F_5 \rightarrow CF_2 + CF_3 + Ar$	4.0×10^{-11}	10
$Ar^* + C_2F_3 \rightarrow CF_2 + CF + Ar$	4.0×10^{-11}	10
$Ar^* + C_2F_6 \rightarrow CF_3 + CF_3 + Ar$	4.0×10^{-11}	10
$Ar^* + C_2F_4 \rightarrow CF_2 + CF_2 + Ar$	4.0×10^{-11}	10
$CF_3^+ + CF_3 \rightarrow CF_3^+ + CF_3$	1.0×10^{-9}	7

$CF_3^+ + C_2F_6 \rightarrow C_2F_5^+ + CF_4$	3.50×10^{-11}	7
$C_2F_5^+ + C_2F_5 \rightarrow C_2F_5^+ + C_2F_5$	1.0×10^{-9}	7
$C_2F_4^+ + C_2F_4 \rightarrow C_2F_4^+ + C_2F_4$	1.0×10^{-9}	7
$F^- + Ar^+ \rightarrow F + Ar$	1.0×10^{-7}	11
$F^- + CF_3^+ \rightarrow F + CF_3$	1.0×10^{-7}	11
$F^- + C_2F_4^+ \rightarrow F + C_2F_4$	1.0×10^{-7}	11
$F^- + C_2F_5^+ \rightarrow F + C_2F_5$	1.0×10^{-7}	11
$F^- + CF_2^+ \rightarrow F + CF_2$	1.0×10^{-7}	11
$CF_3^- + Ar^+ \rightarrow CF_3 + Ar$	1.0×10^{-7}	11
$CF_3^- + CF_3^+ \rightarrow CF_3 + CF_3$	1.0×10^{-7}	11
$CF_3^- + C_2F_4^+ \rightarrow CF_3 + C_2F_4$	1.0×10^{-7}	11
$CF_3^- + C_2F_5^+ \rightarrow CF_3 + C_2F_5$	1.0×10^{-7}	11
$CF_3^- + CF_2^+ \rightarrow CF_3 + CF_2$	1.0×10^{-7}	11
$CF_3^- + F \rightarrow CF_3 + F^-$	5.0×10^{-8}	11
$F + F + M \rightarrow F_2 + M$	$2.4 \times10^{-33}(T/298)^{0.033}$ cm^6 s^{-1}	12
$F + C_2F_4 \rightarrow CF_3 + CF_2$	4.0×10^{-11}	13
$F + C_2F_5 \rightarrow CF_3 + CF_3$	1.0×10^{-11}	13
$F + C_2F_3 \rightarrow C_2F_4$	1.0×10^{-12}	14
$F + CF_3 \rightarrow CF_4$	$1.99 \times10^{-10}(T/300)^{-7.71}\exp(-1183.4/T)$	14
$F + CF_2 \rightarrow CF_3$	8.40×10^{-15}	13
$F + CF \rightarrow CF_2$	3.90×10^{-14}	13
$F_2 + CF_2 \rightarrow CF_3 + F$	4.56×10^{-13}	14

$F_2 + CF_3 \rightarrow CF_4 + F$	1.88×10^{-14}	14
$CF_3 + CF_3 \rightarrow C_2F_6$	7.67×10^{-12}	14
$CF_2 + CF_2 \rightarrow C_2F_4$	5.0×10^{-14}	14
$CF_2 + CF_3 \rightarrow C_2F_5$	8.26×10^{-13}	14

Notes:

a. Only reactions directly affecting species densities are shown here. Additional electron impact collisions (e.g., momentum transfer, vibrational excitation) are included in the EETM.

b. Rate coefficients have units $cm^3 s^{-1}$ unless noted otherwise.

c. Computed using the electron energy distribution and electron impact cross section from cited reference.

d. Estimated by analogy to CF_4.

e. Estimated by analogy to C_2F_6.

f. Estimated. See cited reference for similar reaction.

C.1. References

1. K. Tachibana, Phys. Rev. A **34**, 1007 (1986).
2. D. Rapp and P. Englander-Golden, J. Chem. Phys. **43**, 1464 (1965).
3. R. H. McFarland and J. D. Kinney, Phys. Rev. **137**, A1058 (1965).
4. R. A. Bonham, Jpn. J. Appl. Phys., Part 1 **33**, 4157 (1994)
5. M. Hayashi, in *Gaseous Dielectrics V*, edited by L. G. Christophorou and D. W. Bouldin (Pergamon, New York, 1987).
6. M. Hayashi and T. Nimura, J. Appl. Phys. **54**, 4879 (1983).
7. E. Fisher, M. E. Weber, and P. B. Armentrout, J. Chem. Phys. **76**, 4932 (1982).
8. G. K. Jarvis, C. A. Mayhew, R. P. Tuckett, J. Phys. Chem. **100**, 17166 (1996).
9. P. K. Leichner and R. J. Ericson, Phys. Rev. A **9**, 251 (1974).
10. J. E. Velazco, J. H. Koltz, and D. W. Sester, J. Chem. Phys. **65**, 3468 (1976).
11. R. E Olson, J. R. Peterson, and J. Moseley, J. Chem. Phys. **53**, 3391 (1971).
12. E. L. Duman, N. P. Tishchenko, and I. P. Shmatov, Dokl. Phys. Chem. **295**, 5 (1987).
13. C. Plumb, K. R. Ryan, Plasma Chem. Plasma Proc., **6**, 205 (1986).
14. D. R. F. Burgess, Jr., M. R. Zachariah, W. Tsang, and P. R. Westmoreland, Prog. Energy Combust. Sci., **21**, 453,1996.
15. V. Tarnovsky, P. Kurunczi, D. Rogozhnikov, and K. Becker, Int. J. Mass. Spectrom. Ion Processes **128**, 181 (1993).
16. H. Deutsch, T. D. Bark, V. Tarnovsky, K. Becker, C. Cornelissen, L. Cespiva, and V. Bonacic-Koutecky, Int. J. Mass. Spectrom. Ion Processes **137**, 77 (1994).

AUTHOR'S BIOGRAPHY

Kapil Rajaraman was born in Kanpur, India, in 1976. He received his B.Tech. degree in Engineering Physics from the Indian Institute of Technology, Bombay, India in 1999, and his M.S. in Physics from the University of Illinois at Urbana-Champaign. Under the direction of Professor Mark J. Kushner, he has studied low-temperature, low-pressure plasma processes and their equipment and feature scale simulation since May 2000, with a focus on radiation transport. His work has resulted in one published and two submitted journal articles, and six conference presentations.